PROCESSES AND PREDICTION OF CLIMATE CHANGE IN NORTHERN AFRICA AND THE CENTRAL UNITED STATES

A Dissertation

Presented to the Faculty of the Graduate School

of Cornell University

In Partial Fulfillment of the Requirements for the Degree of

Doctor of Philosophy

by

Christina Marie Patricola

May 2010

© 2010 Christina Marie Patricola

PROCESSES AND PREDICTION OF CLIMATE CHANGE IN NORTHERN AFRICA AND THE CENTRAL UNITED STATES

Christina Marie Patricola, Ph. D.

Cornell University 2010

A method for simulating future climate that combines regional and global models is developed and applied to northern Africa and the central U.S. Simulation with the regional model allows for the optimization of parameterizations and land-surface model, and the horizontal resolution needed to resolve the strong meridional gradients of the Sahel and the West African and Great Plains (GPLLJ) low-level jets. The control and future simulations are not constrained with output directly from atmosphere-ocean general circulation models (AOGCMs). Instead, reanalysis products constrain the control simulations, and future boundary conditions are formed by adding anomalies in SSTs and lateral boundary conditions from AOGCMs forced with a business-as-usual emissions scenario to the reanalysis. This produces realistic control simulations by reducing model error in the boundary conditions.

A nine-member ensemble of late-twenty-first century climate projections for northern Africa is generated using output from nine AOGCMs. The consistency of precipitation projections is much greater for the regional model ensembles than among the AOGCMs. Simulations with projected and idealized SST forcing suggest overall SST warming in part supports the ensemble agreement. Over West Africa, wetter conditions are projected in spring, but midsummer drought – related partly to weakened monsoon flow – develops during June and July, and heat stoke risk increases across the Sahel. Wetter conditions associated with enhanced moisture

transport by the West African westerly jet, a strengthening of the jet itself, and moisture transport from the Mediterranean resume in late summer, and the likelihood of flooding increases.

Over the Great Plains and Midwest precipitation projections for the mid-twenty-first century are similar, with wetter conditions in the spring and drying in the summer. In April and May positive rainfall projections are supported by enhanced local daytime convection, while increased nocturnal rainfall during June in the northern Great Plains is associated with a stronger GPLLJ. Drying in the northern Great Plains is initiated in July by suppressed daytime convection and prolonged though September by positive land-atmosphere feedbacks. Near-surface air temperatures warm annually, with maximum warming over the Great Plains and Midwest of 4.4-5.1°F in August, and variability in summer daily maximum near-surface air temperatures increases.

BIOGRAPHICAL SKETCH

Christina Marie Patricola was born Christina Marie DiRosario on February 14, 1983, to parents Judy and Joseph DiRosario and was raised in Franklin Massachusetts. She developed an early interest in the atmosphere and pursued this interest as a volunteer weather watcher for WCVB TV – Boston during her teens. Christina also enjoys spending time with her friends, family, and her Shetland Sheepdog, Max, playing softball, photography, cartooning, and reciting scenes from comedies with Jennifer and Matthew, her sister and brother. After graduating Franklin High School in June 2001, she attended Cornell University where she received a BS in geological sciences with a concentration in atmospheric science in May 2005, and a MS in atmospheric science with a minor in geology in January 2007. She continued to work under Dr. Kerry H. Cook to complete her Ph. D. and has accepted a post-doctoral research position at Texas A&M University with Dr. Ping Chang.

To my parents, grandparents, and all of my wonderful relatives.

For all your love and encouragement.

To Jennifer and Matthew.

You always keep me laughing. :)

("Did you hear I finally graduated?"

"Yeah, and just a shade under a decade too. All right." [Tommy Boy])

To my dear friends, especially Caitlin, Ian, Michelle, Dan, Pam, and Anthony.

Thank you for always being there, no matter how far away.

ACKNOWLEDGMENTS

I would like to thank my advisor, Professor Kerry H. Cook, for her continued guidance and support throughout my graduate studies, and for all that I have learned from her. I am sincerely grateful for all of the time and energy she gives for her students and for her friendship over the years.

I would also like to express my great appreciation to Prof. Stephen Colucci for all of his feedback and support, and especially for serving as the co-chair of my Special Committee. I am very grateful to the rest of my Special Committee, Prof. Peter Hess and Dr. Michelle Goman, for their constructive comments which have helped improve this work greatly. I also owe a special thank you to Dr. Edward Vizy for many engaging discussions.

I thank my fellow students, Bing Pu, Emily Riddle, Steve Jessup, Marcus Walter, Mike Kelleher, and Naresh Neupane, for their friendship, encouragement, and discussions, and Mark Wysocki, Profs. Art DeGaetano, Dan Wilks, Natalie Mahowald, and Gang Chen, and all of the faculty and students of the Department of Earth and Atmospheric Sciences for their support and encouragement. I am grateful for the antics of my Snee and Bradfield lunch crews, especially Art Bloom, Tiffany Tchakirides, Holly and Jacob Moore, Dan Zarrow, Brian Crandall, and Eowyn Connolly-Brown. I very much appreciate the computer support of Steve Gallow and Brian Belcher and the administrative support of Pam Vitale and Linda Hall.

Finally, I want to express my deepest appreciation for my family and friends and for all my teachers throughout the years – thank you for helping me reach where I am today.

Financial support was provided by National Science Foundation Award ATM-0415481 and the Jackson School of Geosciences at the University of Texas at Austin.

Simulations for Chapters 1 and 2 were run on the National Center for Atmospheric Research supercomputer facility, and simulations for Chapter 3 were run at the Texas Advanced Computing Center (TACC). The Program for Climate Model Diagnosis and Intercomparison has formed and maintains the archive of the IPCC AR4 AOGCM output.

TABLE OF CONTENTS

LIST OF FIGURES

LIST OF TABLES

LIST OF ABBREVIATIONS

AEJ……African easterly jet

AGCM…..……atmospheric general circulation model

AOGCM…..…… coupled atmosphere-ocean general circulation model

AR4…….... Fourth Assessment Report

CMIP…….…….. Coupled Model Intercomparison Project

CRU.…….Climate Research Unit

ECMWF……..……. European Center for Medium Range Weather Forecasting

GCM…….general circulation model

GPCP……. Global Precipitation Climatology Project

GPLLJ…….….Great Plains low-level jet

hPa……...…….……hectopascals

IPCC……..… Intergovernmental Panel on Climate Change

LBCs……. lateral boundary conditions

LBCA…….……...…anomalies in lateral boundary conditions

mm…….…….millimeters

MJJASO……..May – October average

m/s……...…….…meters per second

NARR……...…….North American Regional Reanalysis

NCAR……...National Center for Atmospheric Research

NCEP..…….…National Center for Environmental Prediction

PME……precipitation minus evaporation

ppm…….parts per million

RCM…….regional climate model

SST……..sea surface temperature

SSTA……sea surface temperature anomaly

WAWJ……..……..…..…… low-level West African westerly jet

WRF……..…. Weather Research and Forecasting Model

CHAPTER 1

NORTHERN AFRICAN CLIMATE AT THE END OF THE TWENTY-FIRST CENTURY: AN INTEGRATED APPLICATION OF REGIONAL AND GLOBAL CLIMATE MODELS

1.1 Introduction

As greenhouse warming continues, there is growing concern about the future climate of northern Africa. The Fourth Assessment Report of the Intergovernmental Panel on Climate Change (IPCC AR4; IPCC 2007) highlights this region as exceptionally vulnerable to climate change, especially since the population depends highly on agriculture and climate change may alter the availability of water resources.

The atmosphere–ocean general circulation model (AOGCM) simulations prepared by modeling groups around the world for the IPCC AR4 are state-of-the-art tools for studying future climate, but they do not produce projections of future climate for northern Africa with confidence. This lack of confidence derives in part from the models' difficulties in accurately capturing today's climate processes, although it has become clear that an accurate simulation of past climate variability in this region does not guarantee successful prediction (Cook and Vizy 2006a; Biasutti et al. 2008). It also arises from a concern that the AOGCMs may not simulate future global SST distributions with sufficient accuracy, since we know from studies of present day climate variability that northern Africa is sensitive to SST anomalies—and their gradients—in the Indian, Atlantic, and Pacific Oceans. Indeed, the AR4 AOGCM simulations do not produce a consensus about how rainfall will change due to greenhouse gas increases over northern Africa during the summer, further undermining confidence in the results.

In this paper we design and carry out simulations aimed at providing the most

confident projections of future climate over northern Africa possible given our current state of understanding of the climate of this region and our ability to model that climate. The climates of West Africa and the continent-spanning Sahel are particularly complex, with pronounced thermal and moisture gradients, an intricate series of atmospheric jets, various hydrodynamic instabilities, and a demonstrated sensitivity to both global SSTAs and regional land surface processes. The region has a known propensity for abrupt climate change and decadal-scale drought. The global connectivity of the region's climate combined with the influence of regional-scale structures and processes suggests an approach that combines global climate models (AOGCMs) with a regional climate model (RCM).

Here we provide a projection of climate change for the end of the twenty-first century in northern Africa that is as reliable as possible given the current state of climate system modeling (and the accuracy with which greenhouse gas emissions can be projected). We develop and apply a method for simulating future climate that addresses issues that are particular to our region of interest, but will certainly be useful applied elsewhere, using a high-resolution RCM in conjunction with output from nine AOGCMs. A detailed description of the methodology in the context of the confidence that can be placed in these model predictions is included, and the results are presented with attention to the kinds of information needed to assess impacts.

1.2 Background

The IPCC AR4 assembled and compared output from more than 20 AOGCMs run in standardized simulations of twentieth and twenty-first century climate. The precipitation projections from the AOGCMs were averaged and presented only over areas where the models satisfied a certain level of agreement. In this process, northern Africa did not emerge as a region with confident predictions of the future. For

example, when forced with a modest-growth future emissions scenario, <66% of the AR4 AOGCMs agreed whether most of northern Africa will experience wetter or drier conditions at the end of the twenty-first century. While most of these models produced modest rainfall anomalies, two were outliers that simulated extreme changes in rainfall, one wet and one dry.

In an attempt to complement the ensemble approach to building confidence in AOGCM climate prediction, Cook and Vizy (2006a) examined twentieth century integrations of the AR4 AOGCMs to select models that more accurately represent northern African rainfall and the West African monsoon system, including its interannual variability, reasoning that these models may produce more reliable projections of future climate. They chose three models that capture the region's climate relatively well, but then found that the twenty-first century rainfall projections from these three models are radically different from one another. Of the three models selected, two are the extreme outliers. This suggests that a well-validated twentieth century climate simulation, while certainly being necessary for confident prediction, may not always be sufficient.

Cook and Vizy (2006a) continued their analysis by examining the physical processes of climate change in the selected models, and found that the outlier models exhibit behaviors that are not seen in present day climate observations. While it is not impossible that one of the extreme twenty-first century scenarios will occur, it raises concern when a model diverges so far from the climate dynamics that we see operating in today's climate, especially since the climate models have been developed and tuned over decades with heavy reference to and guidance from the observed climate. With different forcing factors becoming more prominent in the future, it is not clear how strongly we can rely on analogy with the twentieth century climate to validate climate prediction.

Observational studies show that SST forcing is related to Sahel rainfall variability on interannual to decadal time scales (e.g., Lamb 1978; Folland et al. 1991), and there is evidence that climate models with prescribed SSTs are able to capture these relationships, at least in part (Vizy and Cook 2002; Giannini et al. 2003; Hoerling et al. 2006; Hagos and Cook 2008). A number of investigations have tried to understand the potential for climate change in northern Africa in terms of changes in SSTs. Cook and Vizy (2006a) examined projected warming in the Gulf of Guinea in the AR4 AOGCMs and related this warming to Sahel rainfall through a mechanism that is a prominent source of interannual variability in today's climate (e.g., Ward 1998; Vizy and Cook 2002). Biasutti et al. (2008) used 19 pre-industrial integrations of the AR4 AOGCMs to construct a bivariate linear regression model that computes Sahel rainfall as a function of Indo-Pacific SSTs and the meridional Atlantic SST gradient. Unlike, Joly et al. (2007) who find that only one of twelve of these AOGCMs captures the observed relationship between tropical Atlantic SSTs and Sahel rainfall, Biasutti et al. (2008) conclude that their statistical model has skill in simulating rainfall on all timescales in the twentieth century and for twenty-first century interannual and decadal rainfall variability over the Sahel. However, changes in the Indo-Pacific SSTs and the meridional Atlantic SST gradients produced by the AOGCMs fail to explain the trend in Sahelian rainfall in the twenty-first century for the majority of the AOGCMs.

In addition to an often-confusing dependence on SST forcing from three ocean basins (Atlantic, Pacific, and Indian), the climate of northern Africa is also distinguished by an especially strong coupling between the atmosphere and the land surface (e.g., Xue and Shukla 1993; Xue and Shukla 1996; Koster et al. 2004; Patricola and Cook 2007). This coupling is thought to be instrumental in determining the region's variability (e.g., Zeng et al. 1999) and its susceptibility to abrupt change

(e.g., Patricola and Cook 2008). Several modeling studies suggest that positive feedbacks resulting from interactions between the land-surface and the atmosphere can amplify the climate response to forcings such as SSTs or solar variations (e.g., Doherty et al. 2000). But the transient simulations of Liu et al. (2006) suggest that strong low-frequency climate variability, rather than atmosphere/vegetation feedbacks, may be responsible for abrupt change in the region. Paeth and Thamm (2007) propose that until 2025, the impacts of land degradation and vegetation loss over tropical Africa may even be more important than global radiative heating for understanding climate change, and this is supported by Paeth et al. (2009).

These studies indicate that relying on the AR4 AOGCM projections alone may be insufficient for creating reliable predictions of the future for northern Africa. It is clear that considering climate change in terms of variability of the present day climate system is alone not enough since additional climate forcing factors are coming into play. For example, Biasutti et al. (2008) suggest that SSTs may be less influential in forcing the climate in the future and, perhaps, that greenhouse gas forcing will dominate. It is also possible that projected rainfall may depend heavily on model resolution and parameterizations, especially for land-surface/atmosphere interactions, as noted by Cook (2008) and/or the representation of convection. But, since the modeled system is highly nonlinear, attempting to take apart the role of numerous parameterizations in 21 AOGCMs would yield little insight.

The inconsistencies in northern African rainfall projections that arise from using AOGCMs alone, and the limited understanding and confidence that we have so far gained in analyzing these projections, strongly motivate the development of a different approach. This method, which uses a regional model with an optimized set of parameterizations and SST and lateral boundary anomalies from nine AOGCMs, and the confidence that can be placed in it is described in the next section. Model

validation is presented in Section 1.4. In Section 1.5 we project northern African climate for the end of the twenty-first century with focus on variables most relevant for human impacts, including precipitation and heat index. Conclusions and implications are given in Section 1.6.

1.3 Methodology for generating confident future climate predictions

Decisions were made in the simulation design to enhance the reliability of the projections of future climate. There can be no guarantee that a model will produce trustworthy projections for the future, and the emissions scenarios that force the simulated climate change are uncertain, but we need to squarely address issues of uncertainty as best as we can to provide information to the impacts community that is of the highest quality possible. This section includes a detailed description of the methodology within the context of reducing uncertainty in predictions.

The regional model used for all simulations is the Weather Research and Forecasting Model (WRF; Skamarock et al. 2005) version 2.2. This model has been developed and maintained by the National Center for Atmospheric Research (NCAR). It is a non-hydrostatic model with 28 vertical levels, and the top of the atmosphere is set to 50 hPa.

The domain chosen for this study, shown in Figure 1.1 with topography as resolved in the simulations, includes continental Africa and the tropical and subtropical Atlantic and Indian Oceans, extending from 53.8°W–103.8°E to 32.1°S–47.4°N. The location of boundaries is carefully chosen so that large-scale circulation features over and adjacent to northern Africa fit within the domain. A large domain is chosen so that the region of interest is far from the lateral boundaries. Each simulation uses a 90 second time step and 90 km horizontal resolution. Previous work indicates that this resolution is sufficient for producing a sufficiently accurate representation of

the summer climate of the Sahel (e.g., Hsieh and Cook 2005, 2007, 2008; Hagos and Cook 2007) and for capturing land/atmosphere feedbacks (Patricola and Cook 2008). The horizontal resolution is finer than that of typical GCMs and provides information to aid impacts analysis on the regional scale. Integrations are run for 231 days from March 15 to October 31 with the first 47 days disregarded for spin-up. Model output is saved every 3 hours.

Land surface categories are prescribed according to the 10-minute resolution 24-category United States Geological Survey (USGS) data set. The WRF is modified to allow albedo to update daily, instead of the initial value remaining static. Since the resolution of the land surface characteristics is much finer than the resolution of the input surface temperature information, the small lakes covering eastern equatorial Africa are set to the closest vegetation category. This is done to prevent the prescription of unrealistic SSTs on these lakes, since information for both the twentieth and twenty-first century is not available on this space scale. Soil moisture and temperature are initialized from the European Center for Medium Range Weather Forecasting ERA-40 reanalysis (ECMWF 2002) averaged from 1981 to 2000, as previous work suggests that this produces a more accurate control simulation than when the NCEP reanalysis provides the initialization. For consistency, SSTs for the twentieth century simulation are prescribed from the monthly means of the ECMWF reanalysis averaged from 1981 to 2000 as well.

To support reliable projection of future climate, a realistic control simulation is necessary, even though recent results show that it is not sufficient for reliable prediction (Cook and Vizy 2006a; Biasutti et al. 2008). Utilizing the regional model offers the ability to optimize parameterizations and the land-surface model regionally. Several sets of parameterizations and configurations (summarized in Table 1.1) were tested to complement previous modeling experience and optimize for simulation of

African climate north of 10°S. The selection of regionally appropriate parameterizations and land surface model was of critical importance in producing an accurate control simulation of the twentieth century climate. This is demonstrated by the precipitation of two tests simulations for the twentieth century. The regional model is configured exactly the same for these tests, except in test_1, the NOAH land-surface model (Chen and Dudhia 2001), Monin-Obukhov surface scheme (Monin and Obukhov 1954), and Yonsei University (YSU) planetary boundary layer scheme (Hong et al. 2006) are utilized, while in test_2 the RUC land-surface model (Smirnova et al. 1997; Smirnova et al. 2000), Monin- Obukhov Janjic surface scheme (Monin and Obukhov 1954; Janjic 1994, 1996, 2002), and Mellor-Yamada-Janjic planetary boundary layer (Mellor and Yamada 1982; Janjic 1990, 1996, 2002) are used. The average precipitation during May is plotted for test_1 (Fig. 1.2a) and test_2 (Fig. 1.2b), and there are clearly huge differences in the simulations depending on the choice of parameterizations. This, of course, is not to claim that one scheme is superior to another, but to illustrate that the selection of certain parameterizations has a huge impact on a simulation regionally and that the ability to configure the regional model appropriately is one great advantage over the approach of using global models alone.

While the choice of surface parameterizations and land-surface model has a strong impact on the simulation, the use of different cumulus parameterization results in relatively small differences. Two simulations were conducted using exactly the same parameterizations, except the new Kain–Fritsch cumulus scheme (Kain and Fritsch 1990, 1993) is used in one (named test_3), and in the other (named test_4) the Betts-Miller-Janjic parameterization (Betts 1986; Betts and Miller 1986; Janjic 1990, 1994, 2000) is used. Comparison of the May rainfall for test_3 and test_4 (Fig. 1.2c, d, respectively) shows that, at least for these two cumulus schemes, the choice does

not have a large impact on the simulated precipitation.

Based on these tests and previous work, the physical options chosen in this study include the Mellor-Yamada-Janjic planetary boundary-layer scheme (Mellor and Yamada 1982; Janjic 1990, 1996, 2002), the Monin-Obukhov Janjic surface-layer scheme (Monin and Obukhov 1954; Janjic 1994, 1996, 2002), the new Kain–Fritsch cumulus scheme (Kain and Fritsch 1990, 1993), and the Purdue Lin microphysics scheme (Lin et al. 1983; Rutledge and Hobbs 1984; Tao et al. 1989; Chen and Sun 2002). Longwave radiation is calculated by the RRTM scheme (Mlawer et al. 1997), and shortwave is represented by the Dudhia (1989) scheme. The land-surface is represented by the RUC land-surface model (Smirnova et al. 1997, 2000), which solves heat and moisture transfer equations at six levels in the soil column and energy and moisture budget equations for the ground surface.

The National Center for Environmental Prediction (NCEP)/NCAR reanalysis (Kalnay et al. 1996) is used to specify the lateral boundary conditions for the twentieth century simulation. All boundary conditions are derived from the monthly means averaged over 1981–2000 and are linearly interpolated to input to WRF at 6-hourly intervals. These ‘‘climatological’’ lateral boundary conditions maintain variations on the seasonal time scale, but eliminate the diurnal and synoptic effects that are represented in ‘‘synoptic’’ lateral boundary conditions.

Using climatological surface and lateral boundary conditions produces a simulation of the climatology by integrating for 1 year instead of several decades. This method has been used successfully in previous regional climate studies (Vizy and Cook 2002, 2003, 2005; Cook and Vizy 2006b; Patricola and Cook 2007, 2008). Vizy and Cook (2002) compared regional climate simulations that used present day climatological versus synoptic lateral boundary conditions over a domain similar to the one used in this study, and found that including only the seasonal scale in the

lateral boundaries does not significantly impact the results within the domain. For this application, we tested the validity of this methodology by running a simulation with climatological lateral boundary conditions from 1981 to 2000 (test_3) and another with synoptic lateral boundaries from the year 1991 (test_5), with all other configurations the same. Comparison of the simulated May rainfall of test_3 (Fig. 1.2c) and test_5 (Fig. 1.2e) indicates that the use of synoptic versus climatological lateral boundary conditions results in relatively small differences in simulated rainfall, especially when compared to the influence of different surface parameterizations and land-surface models (test_1 and test_2 in Fig. 1.2a, b, respectively). Similar to the findings of Vizy and Cook (2002), this suggests that for this domain in the tropics, the influence of transients propagating across the lateral boundaries is relatively unimportant for the simulation of climate in the interior of the domain and justifies the use of climatological lateral boundary conditions in this study. Although transients are not included in the lateral boundary conditions, the regional model develops them (for example, African easterly waves) within the interior of the large domain. Were this method to be used for another region, it would be prudent to investigate the use of climatological versus synoptic lateral boundary conditions for that domain.

The method developed in this study to produce future climate projections with improved confidence combines the strengths of regional and global climate modeling. For simulating the future, integrations are performed by the regional model with SSTs and global connectivity supplied by the state-of-the-art AOGCMs through anomalies in surface and lateral boundary conditions.

Another feature of the simulation design that is aimed at improving the reliability of the projections is the ensemble approach. Typically when working with GCMs, ensembles are used to give a measure of robustness or a range for projections. GCM ensembles are generated by integrating multiple simulations with the same

physical parameterizations and forcings, but slightly different initial conditions. The spread of the ensemble members is interpreted as a measure of uncertainty. We draw on that approach to develop an ensemble simulation design for regional climate modeling. Here, nine RCM ensemble members are created by using anomalies in surface and lateral boundary conditions from nine AOGCM simulations. In this way, uncertainties associated with the details of the AOGCMs' projections of SSTs and lateral boundary conditions are taken into account to provide a range of behavior in the RCM. When the ensemble members agree, one builds confidence that the results are not depending on the unknowns, in our case, on the different lateral and surface boundary conditions. Boundary conditions are derived from the following AOGCMs which are included in the World Climate Research Programme's (WCRP's) Coupled Model Intercomparison Project phase 3 (CMIP3) multimodel dataset (Meehl et al. 2007) and are archived by the Program for Climate Model Diagnosis and Intercomparison: CCCMA_CGCM3.1, CNRM-CM3, ECHAM/ MPI-OM, GFDL-CM2.0, MIROC3.2(medres), MRICGCM2.3.2, NCAR_CCSM, NCAR_PCM, and UKMOHadCM3.

For the future climate simulations, which represent the end of this century, the 2081–2100 average CO_2 concentration based on the SRESA2 emissions scenario is prescribed. This scenario estimates a relatively high emission rate of CO_2 and high population growth. We choose this emissions scenario so that projections essentially represent inaction on the part of the world community and provide useful information for impacts planning. Another advantage to choosing a high emissions scenario is that the future signal is likely to be clearer than if a low emissions scenario were chosen. In the A2 scenario, the atmospheric CO_2 concentration increases from 330 ppm in the twentieth century integration to 757 ppm for the 2081–2100 mean. Effects of other greenhouse gasses and aerosols are not included. Justification for the selection of one

emissions scenario is provided by GCM simulations that suggest that over West Africa uncertainties in the prescription of SSTs dominate the uncertainty of emissions scenario chosen (Caminade et al. 2006).

SST and lateral boundary conditions taken from the AOGCM simulations are applied as anomalies to the ECMWF and NCEP/NCAR reanalysis present day climatologies, respectively, and are used to produce the future (end of the twenty-first century) climate. Our approach is different from the traditional dynamical downscaling method, which would produce nine control simulations using SST and lateral boundary conditions directly from the twentieth century simulations of the AOGCMs, and then nine twenty-first century simulations. We did not adopt that strategy because confidence in the simulations is promoted by having an accurate simulation of region's climate processes in the control (''present day'') simulation, and using lateral boundary conditions directly from AOGCMs seriously degrades the control simulation in other regional models including the Regional Climate Model (RegCM; Seth and Rojas 2003; Rojas and Seth 2003) as well as the Mesoscale Model 5 (MM5; Cook and Vizy 2008).

For each twenty-first century ensemble member, monthly SST distributions are calculated by adding the monthly SSTAs derived from the AOGCM to the observed monthly climatology as represented in the ECMWF reanalysis. The SSTAs from the AOGCMs are the 2081– 2100 average forced by the SRESA2 emissions scenario minus the 1981–2000 average from the twentieth century (called the 20C3M) simulations. Figure 1.3 shows the June–August averaged SSTAs from the selected nine AOGCMs. The SSTAs exhibit substantial variability in space, although generally the tropical Indian Ocean warms more than the tropical Atlantic Ocean, except in the CNRM-CM3 model (Fig. 1.3c). There is a considerable range of SSTAs, from about 1 to 4 K. While there are differences in the spatial distribution and

magnitude of the SSTAs among the AOGCMs, the models are consistent in that they all project warmer SSTs at the end of the twenty-first century.

Lateral boundary constraints for the twenty-first century simulations are derived similarly to the SST distributions, as monthly anomalies. Values for temperature, zonal and meridional wind, geopotential height, and relative humidity are taken from the AOGCM simulations for 1981–2000 and 2081–2100, differenced, interpolated to the reanalysis grid, and then applied as anomalies to the NCEP/NCAR reanalysis values along the lateral boundaries of the RCM. For the AOGCMs that include quantities interpolated below the local ground surface, the application of anomalies to the reanalysis is straightforward. For the AOGCMs that have missing information below the local ground surface, the anomaly from the lowest level provided by the AOGCM is applied to the reanalysis value.

One concern with this method of creating lateral boundary conditions is that information is taken from only one point in the AOGCM, making it possible to introduce small-scale circulation anomalies generated by the AOGCM. To insure against this possibility, regions located along the boundaries of the RCM domain (Fig. 1.1) were visually inspected in each AOGCM simulation for the twentieth and twenty-first century to be sure there are no local circulation features present.

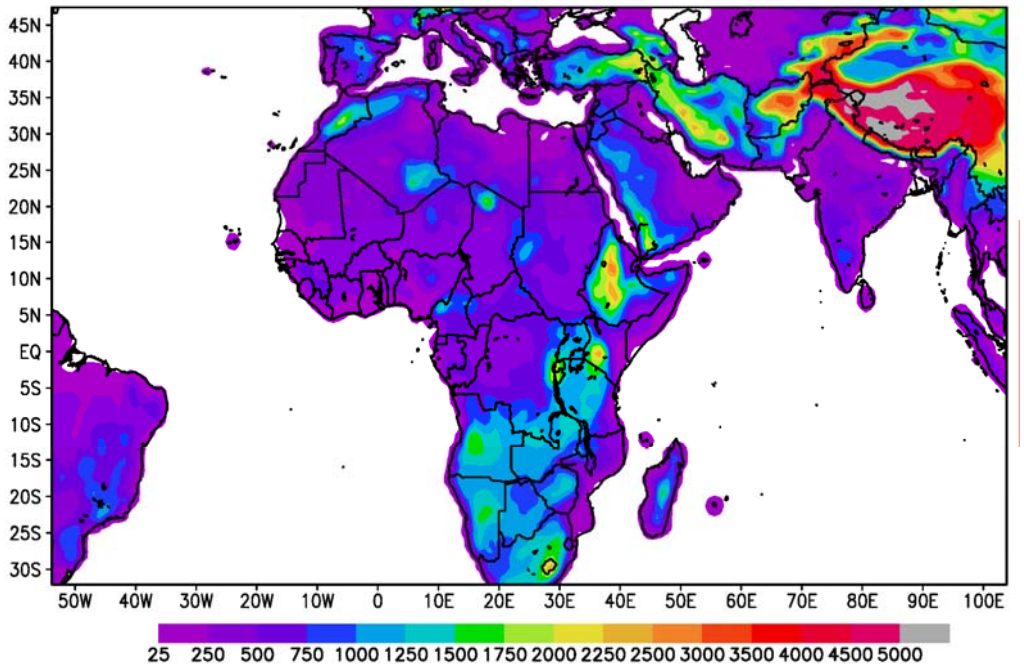

Figure 1.1: Topography (m) at 90 km resolution on the simulation domain.

Table 1.1: Summary of test simulations.

Test number	PBL scheme	Surface scheme	LSM	Convection scheme	Lateral Boundaries	Domain
1	YSU	Monin-Obukhov	NOAH	New KF	Climatological 1981-2000	Excludes South Africa
2	Mellor-Yamada-Janjic	Monin-Obukhov Janjic	RUC	New KF	Climatological 1981-2000	Excludes South Africa
3	YSU	Monin-Obukhov	NOAH	New KF	Climatological 1981-2000	Includes South Africa
4	YSU	Monin-Obukhov	NOAH	Betts and Miller	Climatological 1981-2000	Includes South Africa
5	YSU	Monin-Obukhov	NOAH	New KF	Synoptic 1991	Includes South Africa

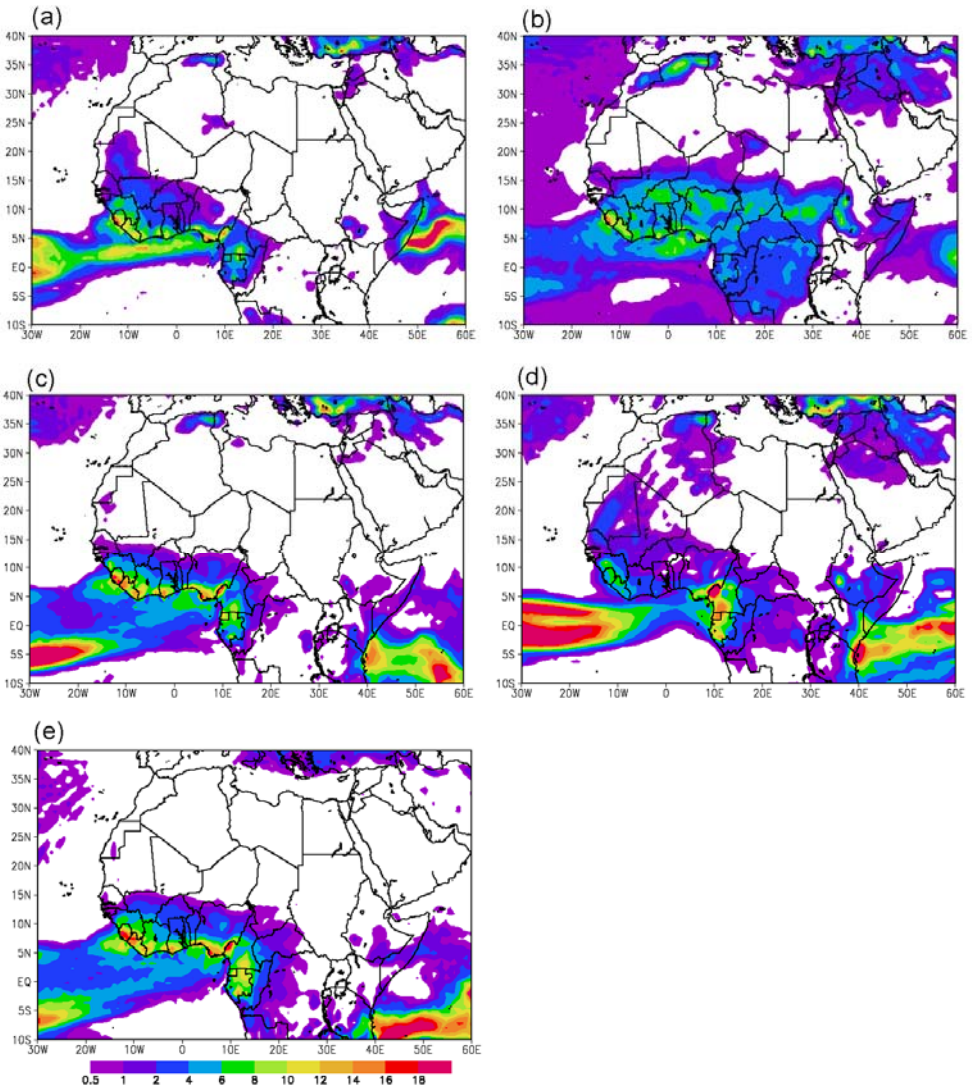

Figure 1.2: Precipitation rate (mm/day) averaged over May from (a) test_1, (b) test_2, (c) test_3, (d) test_4, and (e) test_5.

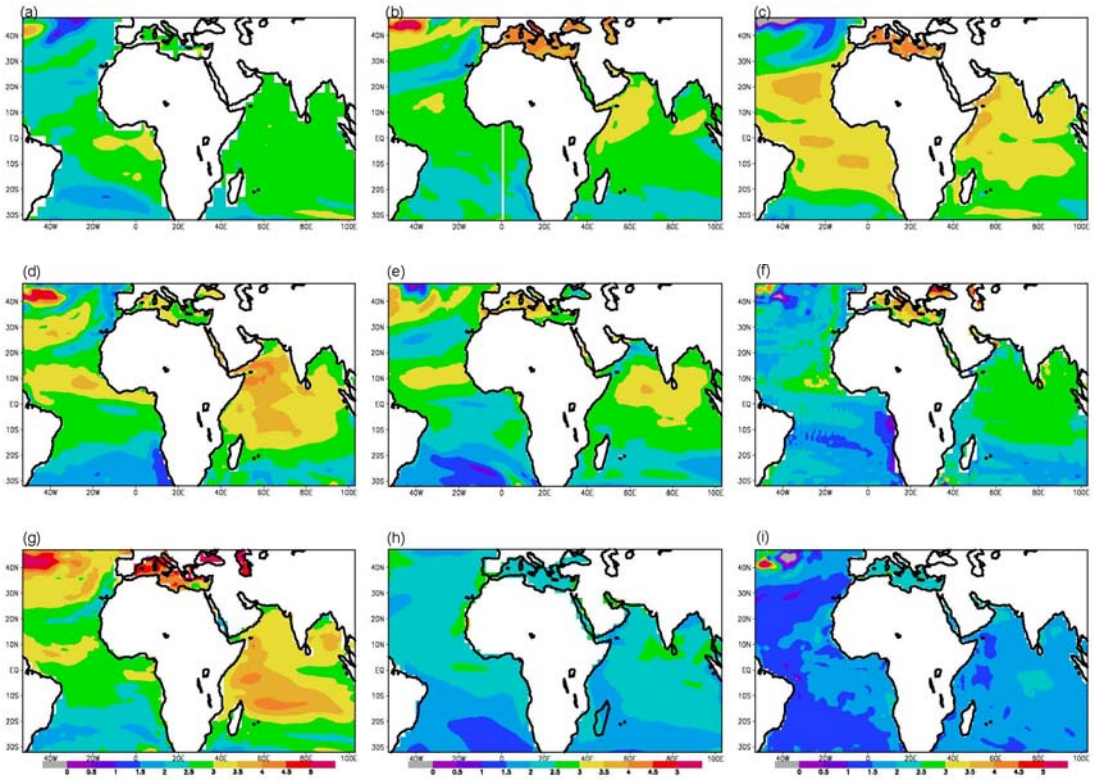

Figure 1.3: SST anomalies averaged June through August calculated as the difference between the 2081–2100 averaged SST forced by the SRES A2 scenario minus the 1981–2000 averaged SST derived from (a) CCCMA_CGCM3.1, (b) NCAR_CCSM, (c) CNRM-CM3, (d) ECHAM/MPI-OM, (e) GFDL-CM2.0, (f) UKMO-HadCM3, (g) MIROC3.2 (medres), (h) MRI-CGCM2.3.2, (i) NCAR_PCM.

1.4 Model validation

The ability of the regional model to represent the observed northern African climate is assessed to support confidence in the results. Particular attention is devoted to the validation of precipitation, since this is such an important variable for human impacts and is also one of the more difficult variables to simulate. Monthly average rainfall of the twentieth century regional model simulation is compared to observations, as well as to twentieth century AOGCM simulations. The ability of the regional model to simulate near-surface air temperature and circulation over northern Africa is also assessed.

Two rainfall data sets are used to include coverage over the ocean and high-resolution information over land (Fig. 1.4a–c). Precipitation from the monthly rain gauge-derived Climate Research Unit data set (CRU; New et al. 1999), averaged over the years 1971–1990, is available over land only on a grid of 0.5° x 0.5°. Rainfall rates over the ocean are given by the monthly Global Precipitation Climatology Project (GPCP; Adler et al. 2003) Version 2 Combined Precipitation data set, averaged from 1981 to 2000. The GPCP data set covers a grid of 2.5° x 2.5° and combines rainfall estimates from satellites and rain gauges. To maintain the resolution of the RCM rainfall, the precipitation from the RCM is presented on its 90 km grid.

Observed rainfall maxima along the Guinean Coast (10°W, 10°E) with additional maxima over Ethiopia and the Central African Republic during May and June (Fig. 1.4a), are represented well in the RCM (Fig. 1.4d). The strong meridional precipitation gradient observed over the African continent between 10°N and 15°N (Fig. 1.4a) is also captured (Fig. 1.4d). In July and August, the observed precipitation maxima (Fig. 1.4b) are more intense than in May and June, and the 0.5 mm/day isohyet is located near 18°N–20°N. The African rainfall maxima are also stronger in the regional model, but the position of the 0.5 mm/day isohyet is farther south than in

the observations (Fig. 1.4e). The rainfall maximum remains over the Guinean Coast region and Sahelian precipitation is underestimated, with the implication that potential future drying over the Sahel during mid-summer may be underestimated. In September and October rainfall rates decrease and the 0.5 mm/day isohyet recedes southward in both the observations and model (Fig. 1.4c, f, respectively).

We also compare the RCM rainfall with a subset of the AOGCM simulations (Fig. 1.5). Based on the analysis of (Cook and Vizy 2006a), examples are shown from two models that do not validate well over northern Africa, the UKMO-HadCM3 and GISS_AOM in Figures 1.5a and b, respectively, and two models that do validate well, the flux-adjusted MRI-CGCM2.3.2 and MIROC3.2(medres) in Figures 1.5c and d, respectively. The RCM clearly produces a more realistic representation of rainfall in July and August compared with some AOGCMs, which erroneously simulate rainfall maxima over the Gulf of Guinea instead of over land (Fig. 1.5a) or do not simulate a West African rainfall maximum at all (Fig. 1.5b). The quality of the simulated rainfall is comparable among the RCM, MRI-CGCM2.3.2, and MIROC3.2(medres). While the land-based rainfall maxima of MRI-CGCM2.3.2, the regional model, and MIROC3.2(medres) are weaker, slightly stronger, and much stronger than observed, respectively, these differences may be within the error of the observations, which are based on a relatively sparse network of rain gauges.

Validation of near-surface air temperature is presented since it is a critical variable for evaluating future impacts. The twentieth century RCM simulation is compared to the ECMWF ERA-40 reanalysis (ECMWF 2002), since that reanalysis provided the SSTs for the twentieth century simulation. Figures 1.6a and d show near-surface air temperature averaged over May and June from the reanalysis and the twentieth century RCM simulation, respectively. The reanalysis places the warmest regions over Mauritania and Mali in West Africa, Sudan and Egypt in North Africa,

and the Arabian Peninsula, and the RCM simulates the location and magnitude of these maxima well. The regional model also accurately places the coolest temperatures over the east African highlands, but produces warmer temperatures than in the reanalysis over equatorial Africa. Modeled temperatures are warmer than the reanalysis over the Sahel in July and August when simulated rainfall is weaker than observed. The seasonality in near-surface air temperature is fairly well represented in the RCM, although in northwestern Africa the reanalyzed temperature is warmer in July–August (Fig. 1.6b) than during May–June (Fig. 1.6a), while this is reversed in the regional model (Fig. 1.6d and e). Despite these discrepancies, the RCM performs reasonably well.

The NCEP/NCAR reanalysis is used to validate circulation and geopotential height fields in the RCM since lateral boundary conditions were derived from that reanalysis. Since observations are relatively sparse over northern Africa we expect that the magnitudes of wind and geopotential height maxima and minima may be slightly different between the RCM simulation and the reanalysis. Differences may also be related to the finer resolution of the RCM (90 km) compared to the reanalysis (2.5° x 2.5°).

The regional model reproduces the features of the West African summer monsoon and northern African circulation realistically. Figure 1.7a - d show the reanalyzed and simulated geopotential height and wind field at 925 hPa averaged from June through September, respectively. The shallow thermal low at about 15°N is slightly weaker in the RCM, and the subtropical high (near 35°N and 30°W) is somewhat stronger than in the reanalysis. Over West Africa, the reanalyzed southerly monsoon winds from the Gulf of Guinea converge with the northerly winds from the Mediterranean region near 15°N, and this is captured in the twentieth century simulation, but with stronger northerlies and a convergence zone located about two

degrees farther south which is consistent with the precipitation issues previously discussed. Another important feature of the low-level flow which provides an important moisture source for the Sahel (Patricola and Cook 2007) is the low-level westerly jet off the west coast of Africa near 12.5°N (Grodsky et al. 2003). It is barely discernable in the reanalysis, perhaps because of the coarser resolution, and more apparent in the RCM simulation. The subtle westerly flow over Central Africa is similar between the reanalysis and the RCM. Over East Africa, the Somali jet is also well represented in the twentieth century simulation.

The divergent Saharan high overlays the low-level thermal low near 600 hPa, as seen in Figure 1.7b. The African easterly jet, which forms over the strongest surface temperature gradients when Coriolis accelerations act on the northerly outflow from the Saharan High (Cook 1999), is located at about 15°N. Both the Saharan high and the African easterly jet are represented more strongly, but reasonably, in the RCM (Fig. 1.7e). At 200 hPa, both the reanalysis and the model (Fig. 1.7c, f, respectively) produce high pressure over the Arabian Peninsula extending over northern Africa, and the associated tropical easterly jet located near 15°N.

In summary, the RCM produces a satisfactory simulation of the twentieth century summer climate of northern Africa, comparable to or better than that of the current generation of AOGCMs and suitable for applications to study the future climate of northern Africa on regional space scales.

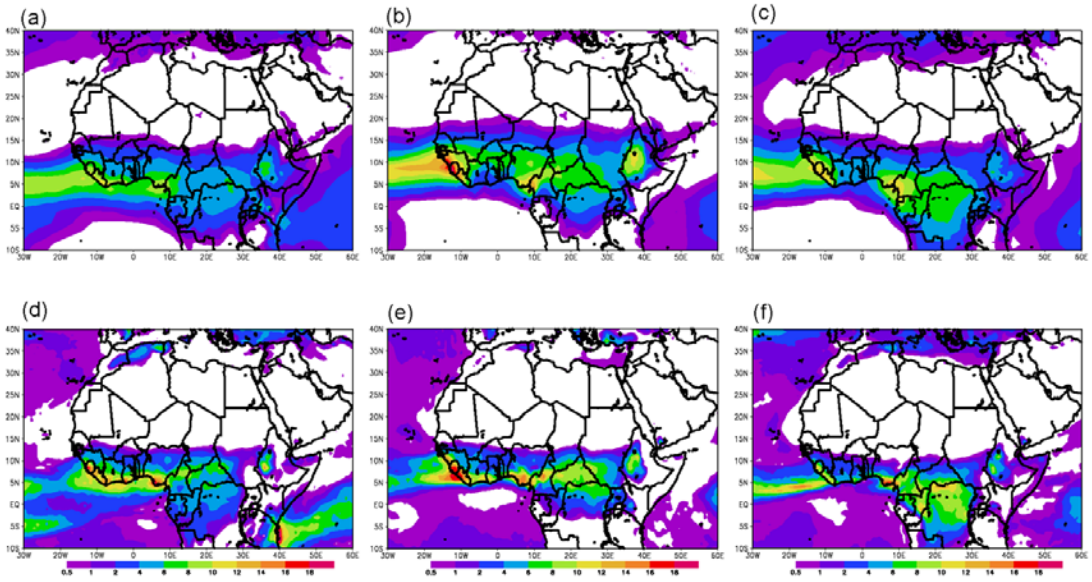

Figure 1.4: Precipitation rate (mm/day) from the CRU data set over land, averaged over 1971–1990 on a 0.5 x 0.5° grid and from the GPCP Version 2 data set over ocean, averaged over 1981–2000 on a 2.5° x 2.5° grid during (a) May and June, (b) July and August, and (c) September and October. Precipitation rate (mm/day) from the twentieth century RCM simulation on a 90 km grid during (d) May and June, (e) July and August, and (f) September and October.

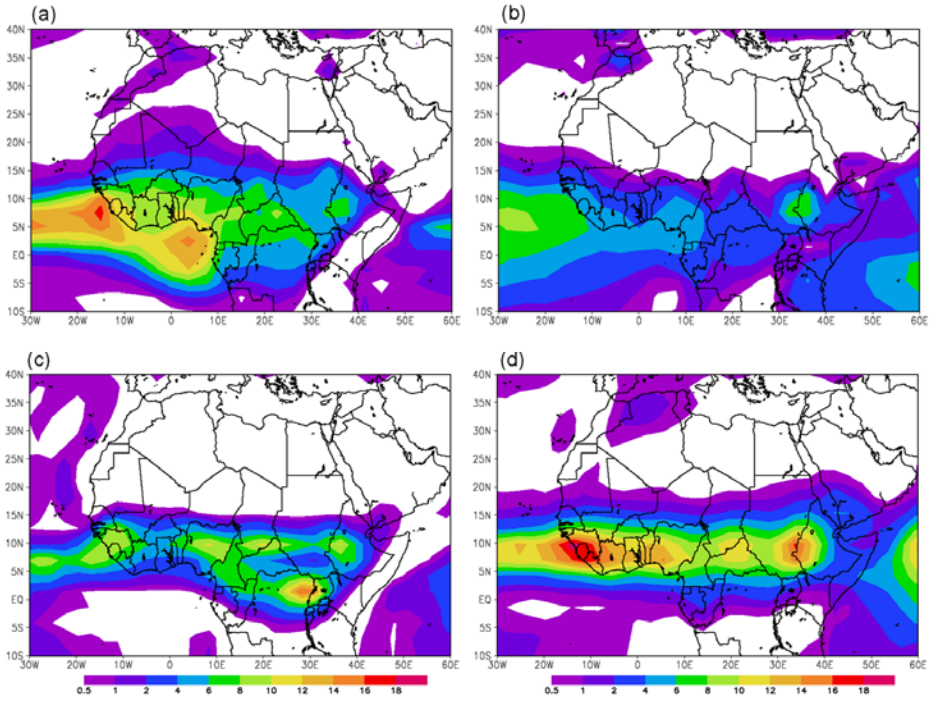

Figure 1.5: Simulated precipitation rate (mm/day) from (a) UKMO-HadCM3, (b) GISS_AOM, (c) MRI-CGCM2.3.2, and (d) MIROC3.2(medres) models averaged over July and August of 1981–2000.

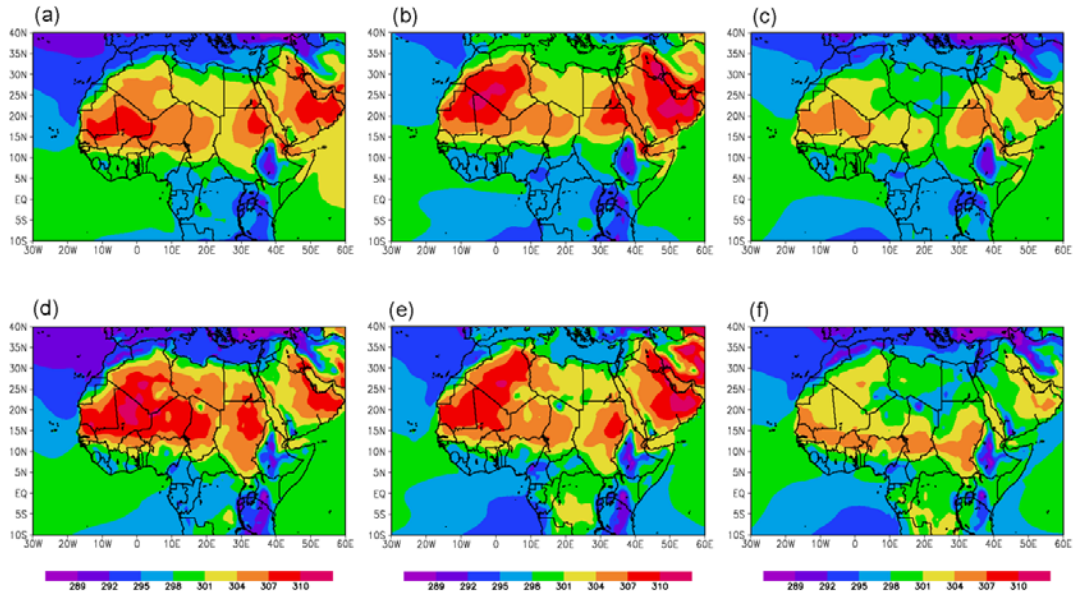

Figure 1.6: Near-surface air temperature (K) averaged over (a) May–June, (b) July–August, and (c) September–October of 1981–2000 from the ECMWF reanalysis and over (d) May–June, (e) July–August, and (f) September–October from the twentieth century RCM simulation.

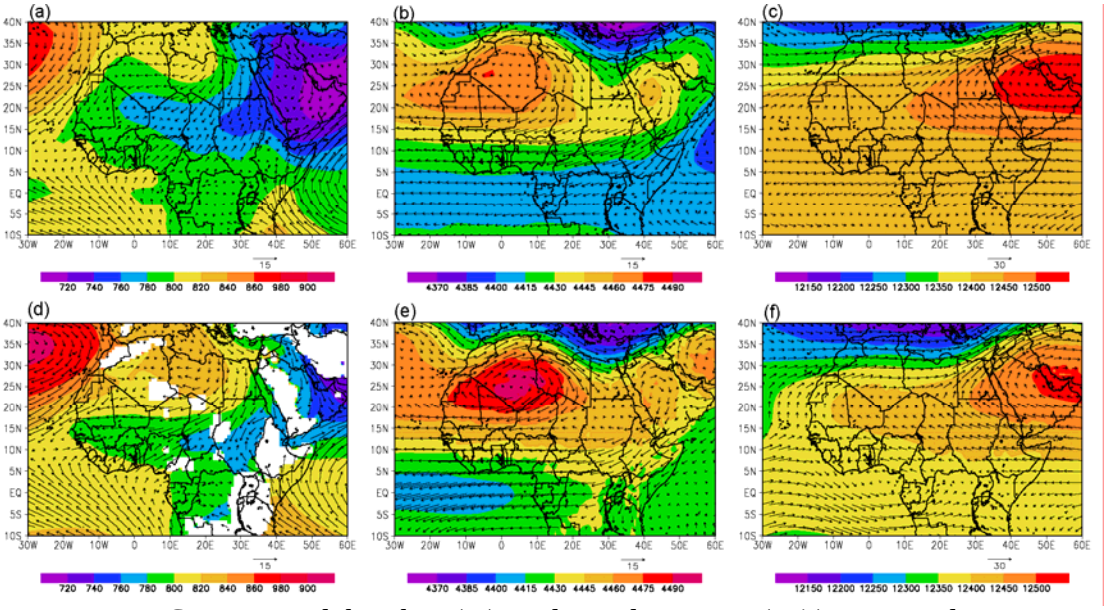

Figure 1.7: Geopotential heights (m) and wind vectors (m/s) averaged over June through September of 1981–2000 at (a) 925 hPa, (b) 600 hPa, and (c) 200 hPa from the NCEP/NCAR reanalysis and at (d) 925 hPa, (e) 600 hPa, and (f) 200 hPa from the twentieth century RCM simulation. White regions are underground in the model simulations, while variables are interpolated through topography in the reanalysis.

1.5 Results

Results from the regional model twentieth century and twenty-first century climate simulations described in Section 1.3 are presented, including comparisons with some results from the IPCC AR4 reports. Focus is on quantities that have the most impact on humans and agriculture, including monthly rainfall, extreme rainfall events, near-surface air temperature, and heat index.

1.5a Precipitation

Monthly ensemble mean twenty-first century minus twentieth century precipitation anomalies derived from the regional model are plotted in Figure 1.8. Only precipitation anomalies for which seven or more (77% or greater) of the nine ensemble members produce the same sign are shown. Areas where <77% of the ensemble members agree on the sign of the anomaly are shaded gray. Figure 1.8 is similar to Figure 3.3 of the IPCC AR4 Synthesis Report, but not directly comparable because the emissions scenario selected and months included in the averaging are different. Also the 77% criterion used here is stricter than the 66% criterion used in the IPCC report.

To allow for direct comparison between the results from the regional and global models, the monthly ensemble average precipitation anomalies derived from the nine AOGCM simulations used to produce the RCM ensemble are plotted in Figure 1.9 in the same format as Figure 1.8. Precipitation from each AOGCM is interpolated to the grid of the regional model. The precipitation anomalies plotted in Figure 1.9 are quite similar to those from Figure 3.3 of the IPCC AR4, with inconsistent projections (gray shading) over nearly all of northern Africa. However, positive rainfall anomalies emerge over the Guinean Coast during July–September in Figure 1.9, while the signal over that region is inconsistent in Figure 3.3 of the IPCC

AR4. This may be due to the different emissions scenarios used.

It is evident by comparison of Figs. 1.8 and 1.9 that the ensemble members of the regional model show more consensus than the global models that provide surface and lateral boundary constraints for them. Wetter conditions simulated over central equatorial Africa during May and June in the AOGCMs (Fig. 1.9a) are not reproduced in the RCM simulations (Fig. 1.8a). During July the regional model produces drying along the Guinean Coast, while the AOGCMs project wetter conditions. In August and September the regional and global models both simulate wetter conditions at the end of the twenty-first century over parts of the Guinean Coast.

The RCM ensemble simulates a strong seasonality in the rainfall signal over northern Africa and the signal varies significantly by region (Fig. 1.8). To provide a measure of how extreme the twenty-first century anomalies are in comparison to twentieth century rainfall rates, the ensemble average twenty-first century precipitation is plotted in Figure 1.10 as a percent of the simulated twentieth century rainfall rate. A value of 100 indicates that the twenty-first century and twentieth century rainfall rates are equal, whereas a value of 10 means that in the twenty-first century the rainfall rate is only 10% of its twentieth century value. Regions where <0.25 mm/day of rainfall is received in the twentieth century simulation are shaded white to prevent misleading high percentages resulting from a very low value in the denominator.

In West Africa, including Senegal, Gambia, Guinea Bissau, Guinea, Sierra Leone, Liberia, Mali, Ivory Coast, Ghana, Burkina Faso, Togo, Benin, and Nigeria rainfall rates at the end of the twenty-first century are generally projected to increase during May by up to 6 mm/day along the coast and 2 mm/day inland (Fig. 1.8a) corresponding to about a 50% increase from the twentieth century rate (Fig. 1.10a). During June and July negative rainfall anomalies of up to 7 mm/day (Fig. 1.8b, c), or

50–75% (Fig. 1.10b, c) are simulated. In August, September, and October (Fig. 1.8d–f), wetter conditions, in some regions more than a doubling of rainfall, are simulated at the end of the twenty-first century with the exception of drying over the Guinean Coast in August. No changes in rainfall are simulated over Niger and Mauritania where the twentieth century simulation produces conditions that are too dry. Since the regional model tends to simulate West African rainfall in a contracted band compared to the observations, it is possible that the twenty-first century rainfall anomalies simulated over the southern Sahel may apply to the northern Sahel as well.

Over the western part of North Africa, including Morocco, Algeria, and Tunisia, wetter (drier) conditions are projected over localized areas during May (June) (Fig. 1.8a, b). There is little change in July and August (Fig. 1.8c, d) and some drying in September and October (Fig. 1.8e, f). Over Western Sahara and the northeastern countries of Libya and Egypt both the twentieth and twenty-first century simulations produce no rainfall from May through October.

The precipitation projections vary regionally over Central Africa, including Chad, Sudan, Cameroon, Central African Republic, Democratic Republic of Congo, Congo, Gabon, and Equatorial Guinea. During May and June projections are generally wetter by about 1–2 mm/day representing about a 25% increase from the twentieth century (Figs. 1.8a, b, 1.10a, b, respectively), except for a dry band over Chad in May and June and Sudan in May. During July conditions are projected to be drier by 2–4 mm/day (Fig. 1.8c) over many parts of Central Africa. In August and September (Fig. 1.8d, e) there is an east–west dipole, with wetter (drier) conditions in the western (eastern) part of Central Africa. Drying over southern Sudan is severe, with essentially no rainfall occurring in the twenty-first century simulation (Fig. 1.10d, e). Generally wetter conditions or an inconsistent signal are simulated in October (Fig. 1.8f).

Over East Africa, including Eritrea, Ethiopia, Djibouti, Somalia, Uganda, Kenya, Rwanda, Burundi, and Tanzania, precipitation projections also vary regionally. Drier (wetter) conditions are projected over Tanzania and southern Kenya (southern Somalia) during May and June (Fig. 1.8a, b). Drying in Tanzania and Kenya is extreme (Fig. 1.10a, b). In July, August, and September (Fig. 1.10c–e) there is nearly complete drying in parts of Ethiopia, Kenya, Uganda, and Rwanda, with the greatest severity in August. Djibouti, the northern tip of Somalia, and parts of Ethiopia are projected to be wetter (drier) in September (October) (Fig. 1.10e, f).

Since changes in evaporation impact changes in water availability, precipitation minus evaporation anomalies are also evaluated. Monthly ensemble average twenty-first century minus twentieth century precipitation minus evaporation anomalies derived from the RCM (not shown) are similar to the precipitation anomalies (Fig. 1.8). Differences in evaporation (not shown) are opposite in sign, but smaller in magnitude than the precipitation anomalies. They are largest over West Africa during June through September where rates increase by up to 2 mm/day, and over eastern equatorial Africa in August and September where rates decrease by up to 5 mm/day. Comparison of the precipitation and precipitation minus evaporation anomalies demonstrates that the structure and sign of the precipitation minus evaporation projections are dominated by changes in precipitation, not evaporation.

Of great importance for impacts analysis are changes in extreme rainfall events. Based on the monthly precipitation anomalies (Fig. 1.8), West Africa emerges as a region that warrants further investigation of how the precipitation rates are distributed at the end of the twenty-first century to assess flooding risk. Box plots are a useful way to display the distribution of a data set and show the minimum, first quartile, median, third quartile, maximum values, and outliers, which are defined here as values that exceed the third quartile value plus 1.5 times the innerquartile range or

are less than the first quartile minus 1.5 times the innerquartile range. Box plots of 3-hourly land-based rainfall rates for the twentieth century and nine twenty-first century regional model simulations are shown for West Africa averaged over 18°W–18°E and 8–15°N (Fig. 1.11). The time period of analysis includes August 1 through September 30 and is chosen to isolate only the months during which rainfall is projected to increase in the twenty-first century.

In all of the twenty-first century simulations, the third quartile values exceed that of the twentieth century by at least 0.8 mm/day. In addition, simulated twenty-first century maximum rainfall rates are more intense than that of the twentieth century simulation, increasing to 12.3–21.5 mm/day from 9.5 mm/day. The wetter conditions during August–September over West Africa are related to a higher frequency of more intense rainfall events, indicating the increased possibility for flooding during the twenty-first century over this region in the late summer.

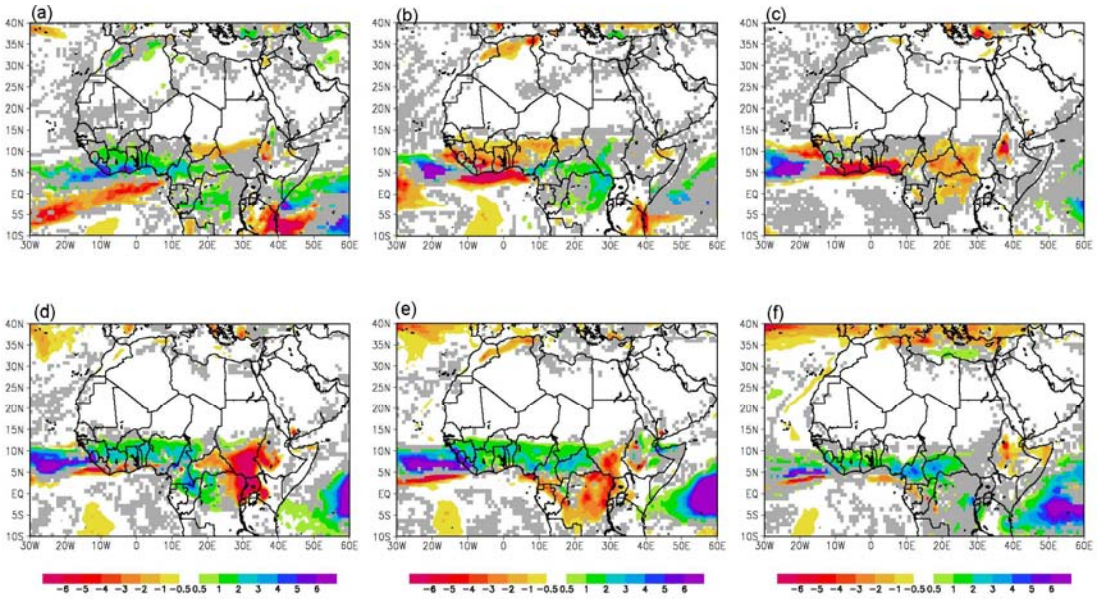

Figure 1.8: Ensemble averaged monthly precipitation anomalies (twenty-first century–twentieth century) from the RCM simulations for (a) May, (b) June, (c) July, (d) August, (e) September, and (f) October. Units are mm/day. Areas where <77% of the ensemble members agree are shaded gray.

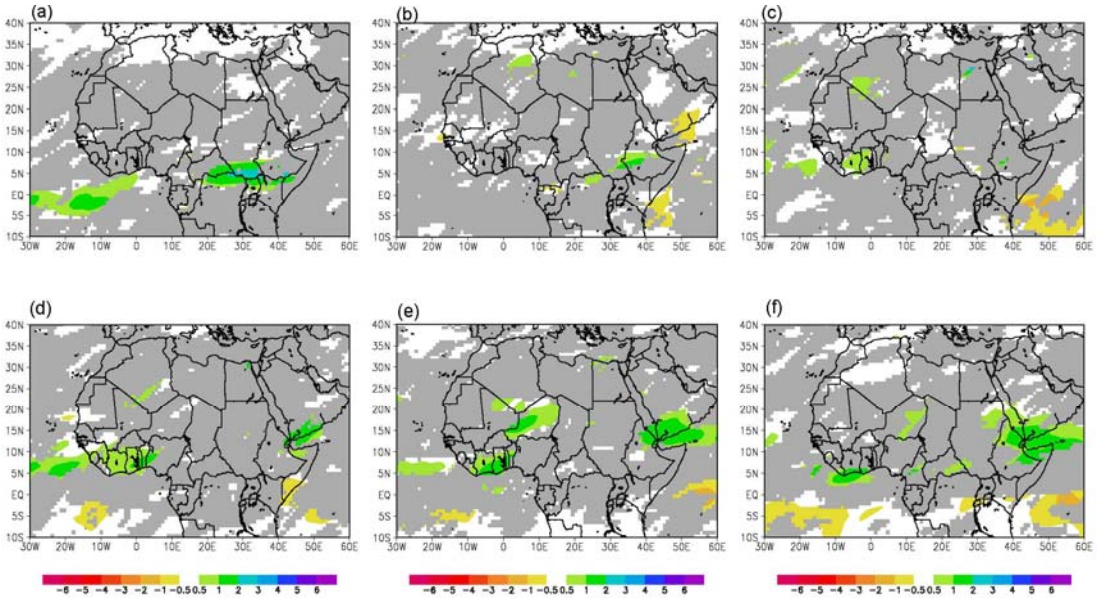

Figure 1.9: Ensemble averaged monthly precipitation (mm/day) anomalies (twenty-first century minus twentieth century) from the nine IPCC AOGCM simulations used in this study (see text) for (a) May, (b) June, (c) July, (d) August, (e) September, and (f) October. Values are the difference between the 2081–2100 averaged monthly precipitation forced by the SRES A2 scenario minus the 1981–2000 averaged monthly means. Areas where <77% of the ensemble members agree are shaded gray.

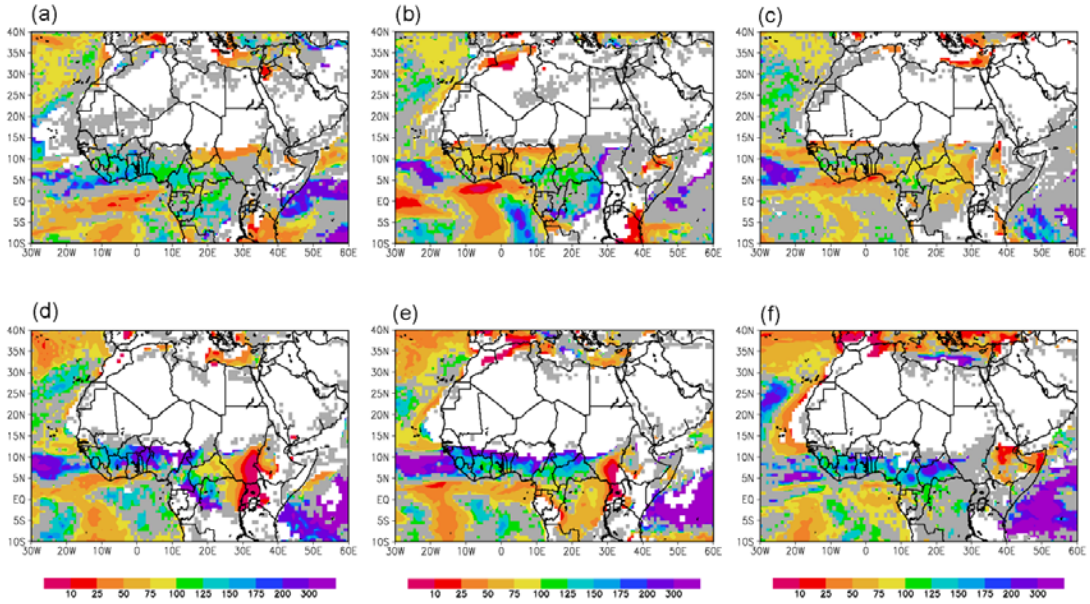

Figure 1.10: Ensemble averaged twenty-first century precipitation rate as a percent of the twentieth century precipitation rate from the regional model simulations. The value 100 indicates the twenty-first century and twentieth century precipitation rates are equal. Regions where the twentieth century monthly rainfall is <0.25 mm/day are shaded white.

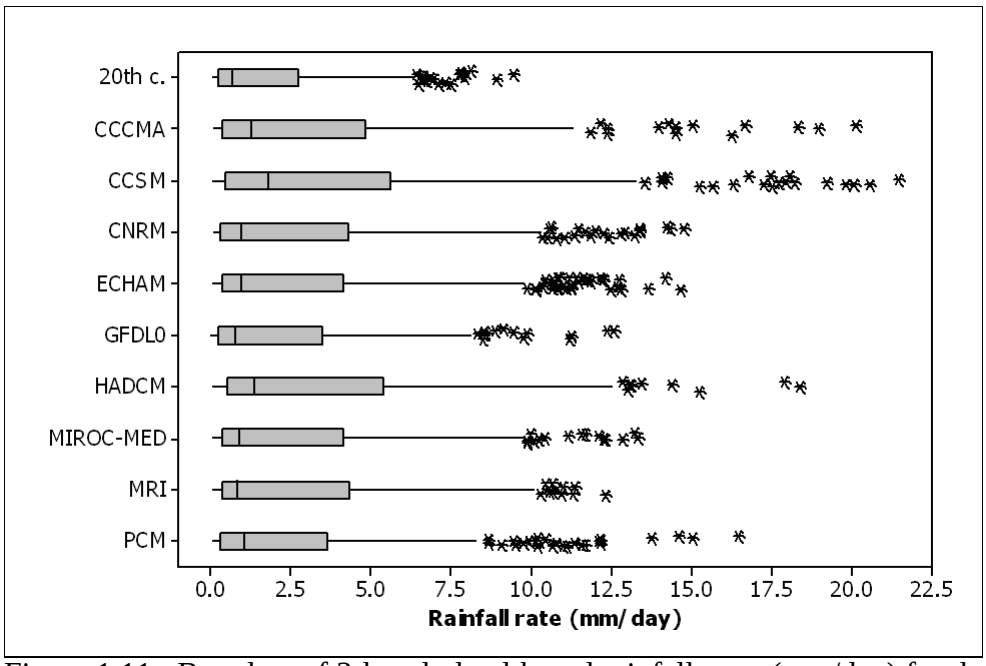

Figure 1.11: Boxplots of 3-hourly land-based rainfall rates (mm/day) for the twentieth century and nine twenty-first century regional model simulations over West Africa covering 18°W–18°E and 8–15°N including events between August 1 through September 30. Outliers are denoted with stars offset to clarify overlapping marks.

1.5b Near-surface air temperature and heat index

The ensemble near-surface air temperature anomalies averaged from May through October simulated by the RCM and AOGCMs are shown in Figures 1.12a, b, respectively, with Figure 1.12b comparable to Figure 3.2 of the IPCC AR4. In contrast to the precipitation projections, there is a high level of agreement between the RCM and AOGCMs about the positive sign of projected near-surface air temperatures at the end of the twenty-first century. The RCM ensemble mean produces maximum warming of about 6 K over northwestern Africa (Fig. 1.12a), similar to that of the AOGCM mean (Fig. 1.12b). There is additional strong warming related to the July–August twenty-first century drought over the East African highlands in the RCM ensemble mean and a warming minimum over the central Sahara which are not produced by the AOGCM ensemble mean. A minimum in warming is simulated over the Guinean Coast and the coastal regions of the Horn of Africa by both the regional and global models. Despite the differences in the distribution, both modeling approaches produce an average warming between 3 and 6 K over of northern Africa.

A more detailed understanding of the warming is necessary to address the likelihood of additional heat waves in the future. Figure 1.13a and b display box plots of 3-hourly near-surface air temperatures over land during May 21–August 21 from the twentieth century and twenty-first century simulations for the Sahel (18°W–18°E and 8–15°N) and the Guinean Coast (9°W–9°E and 4–7.5°N), respectively. As expected, all ensemble members simulate warming in the twenty-first century over both regions. Over the Sahel region the median surface air temperature warms by 3.2–5.4 K (with a median of 4.0 K), from 301.6 K in the twentieth century to 304.8–307.1 K in the future. Since the distribution of temperature is shifted to the right, values which were extreme in the twentieth century occur more often in the twenty-first century. Eight of the nine RCM ensemble members simulate a median air temperature

that exceeds the third quartile of the twentieth century simulation, and the maximum temperature rises from 310.2 K in the twentieth century to 312.9–314.6 K in the twenty-first century. It is clear from these changes in the temperature distribution that extreme high temperatures will occur more commonly in the twenty-first century, increasing the likelihood for longer and more intense heat waves over the Sahel region.

Over the Guinean Coast region (Fig. 1.13b), warming is more moderate, with a median near-surface air temperature of 296.8 K in the twentieth century and a range of 298.8– 300.7 K in the twenty-first century, representing an increase of 2.0–3.8 K with a median of 3.4 K. Again higher temperatures occur more frequently, with the median of all nine twenty-first century RCM ensemble members exceeding the third quartile of the twentieth century simulation. Maximum temperatures rise by 1.8–7.1 K, from 301.2 K in the twentieth century to 303.0–308.3 K in the twenty-first century.

These temperature changes are accompanied by changes in relative humidity, and both are significant for understanding impacts on human health due to heat exposure (Steadman 1979). The heat index is a convenient way to represent the combination of changes in these two factors for human comfort and health. Although perceived temperature is also affected by wind speed, atmospheric pressure, and solar radiation, it is a good assumption that changes in temperature and humidity are the most important. The heat index defined by Steadman (1979) follows the equation:

$$\mathrm{HI} = -42.4 + 2.05(\mathrm{T}) + 10.1(\mathrm{R}) - 0.225(\mathrm{TR}) - 6.84(10^{-3})(\mathrm{T}^2)$$
$$-5.48(10^{-2})(\mathrm{R}^2) + 1.23(10^{-3})(\mathrm{T}^2\mathrm{R}) + 8.53(10^{-4})(\mathrm{TR}^2) - 1.99(10^{-6})(\mathrm{T}^2\mathrm{R}^2), \quad (1.1)$$

where HI is the heat index (°F), T the air temperature (°F), and R is the relative humidity in percent. Steadman (1979) developed this heat index for temperatures above 80°F (300 K), which is generally the case over northern Africa in summer. He

included a condition for relative humidities above 40%, and this is also generally satisfied in summer except over the Sahara, where the low humidity results in a perceived temperature that is cooler than the actual air temperature. A heat index between 80 and 90°F (300–305 K) indicates a possibility of fatigue related to prolonged exposure to the sun and physical activity. Sunstroke, a serious life threatening condition, and heat cramps are possible for a heat index of 90–105°F (305–314 K) and likely for a heat index of 105–130°F (314–326 K). Sunstroke is very likely for a heat index that exceeds 130°F (326 K). For conciseness, the heat index categories 300– 305, 305–314, 314–326, and over 326 K will be referred to as low, medium, high, and severe risks, respectively.

We calculate the maximum heat index for each day between May 1 and October 31 occurring between 09Z and 15Z, the period when maximum air temperatures are probable over northern Africa. Figure 1.14a–c show the number of times the worst daily heat index reaches the low, medium, and high risk categories during the May–October period in the twentieth century RCM simulation, respectively, and Figures 1.14d–f are the same for the twenty-first century heat indices. (The number of days in the severe heat index category is not plotted because this threshold is not exceeded in any simulation.)

In the twentieth century simulation, the Guinean Coast region experiences around 120 low-risk days, 0–40 medium- risk days, and no high-risk days (Fig. 1.14a–c, respectively). In the twenty-first century simulations, the medium- and high-risk heat indices (Fig. 1.14e, f) occur more frequently at the expense of low-risk events (Fig. 1.14d). Similarly, over the Sahel higher risk heat indices occur more frequently, with up to 180 days of medium risk (Fig. 1.14b) and no high-risk days (Fig. 1.14c) in the twentieth century, and up to 160 high-risk days in the twenty-first century (Fig. 1.14f). At the end of the twenty-first century people in the Sahel region are projected

to experience the most severe increases in sun stroke and heat cramps.

In East Africa over Somalia, the number of medium-risk days increases from around 40 in the twentieth century (Fig. 1.14b) to over 160 in the twenty-first century (Fig. 1.14e). Ethiopia becomes more susceptible to low-risk heat indices in the twenty-first century (Fig. 1.14a, d). Over Central Africa, medium-risk days become more prevalent (Fig. 1.14b, e) and high-risk days increase from zero in the twentieth century (Fig. 1.14c) to up to 100 in the twenty-first century (Fig. 1.14f).

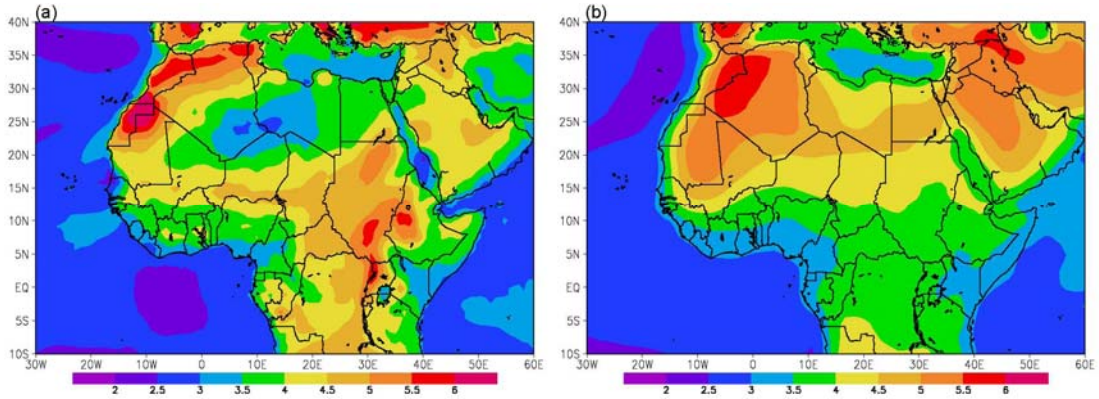

Figure 1.12: Ensemble averaged May–October near-surface air temperature (K) twenty-first century–twentieth century anomalies from (a) RCM and (b) AOGCM simulations.

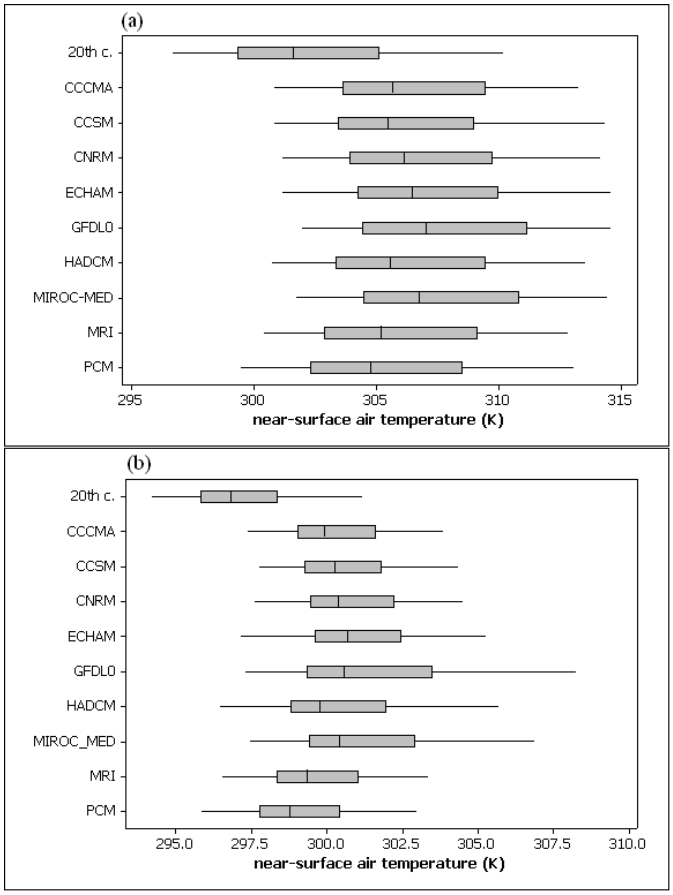

Figure 1.13: Boxplots of 3-hourly land-based near-surface air temperature (K) from May 21 to August 21 for the twentieth century and nine twenty-first century RCM simulations for (a) the Sahel region averaged over 18°W–18°E and 8–15°N and (b) the Guinean Coast region averaged over 9°W–9°E and 4–7.5°N.

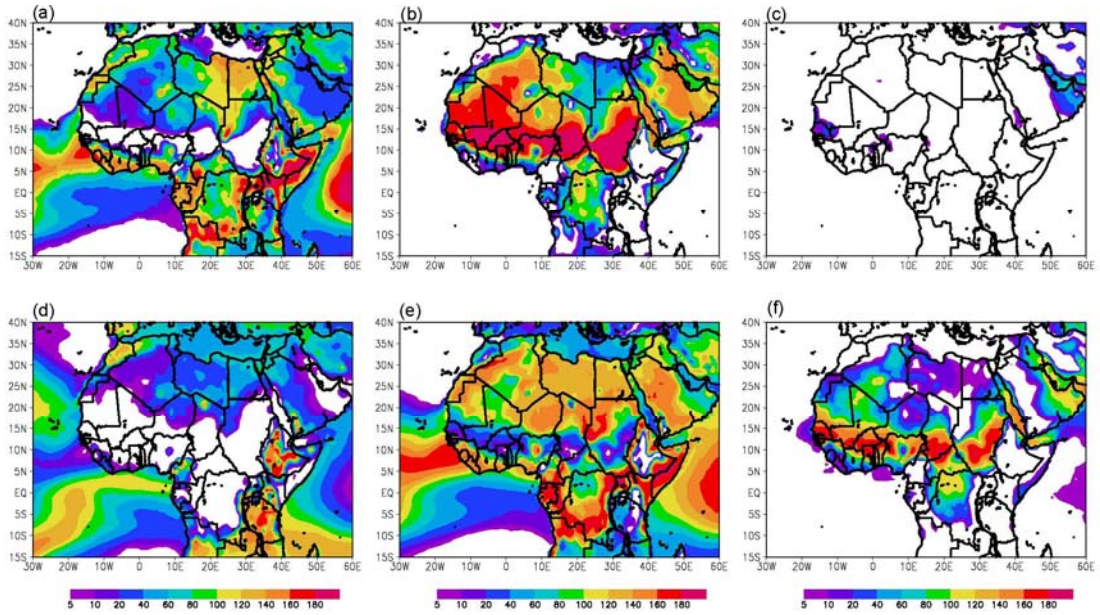

Figure 1.14: The number of days between May 1 and October 31 during which the maximum heat index occurring between 09Z and 15Z is in (a) low, (b) medium, and (c) high risk category in the twentieth century simulation, and the twenty-first century ensemble average number of days between May 1 and October 31 during which the maximum heat index occurring between 09Z and 15Z is in (d) low, (e) medium, and (f) high risk category.

1.6 Conclusions

A method for predicting future climate that utilizes both regional and global models is developed and applied to project climate change during this century over northern Africa. The regional model offers the fine horizontal resolution appropriate for capturing climate processes accurately and providing information on space scales appropriate for impacts analysis. Selecting a set of parameterizations and a land-surface model that are optimal for simulation of northern African climate improves the simulation. Output from present day and future simulations from AOGCMs, which were produced for the IPCC AR4, provides anomalies in future SST and global connectivity. This method is not to be confused with traditional dynamical downscaling, which applies boundary conditions to a regional model directly. Boundary conditions for the regional model are derived from monthly mean AOGCM output to maintain information about the seasonal cycle, but to remove synoptic and diurnal effects. Similar to other studies, testing shows that the influence of prescribing transients in the lateral boundary conditions is small on the tropical domain, validating this choice for climate simulation.

An ensemble approach is taken to provide different realizations of future climate in the regional model. The atmospheric CO_2 concentration is increased to 757 ppmv, which is the mean value for 2081–2100 according to the IPCC's SRESA2 emissions scenario. A nine-member ensemble representing northern African climate for 2081–2100 is created by adding SST and lateral boundary condition anomalies from nine different AOGCM simulations to the present day boundary conditions. A benefit of this method is that there is only one control simulation, and nine twenty-first century simulations. If we were to use nine twentieth century simulations with nine twenty-first century simulations with lateral boundary conditions provided directly from the AOGCMs, it would be unclear how much the quality of the control

simulations impacts a climate change response. In addition, this method produces a relatively accurate control simulation of the northern Africa climate.

Agreement among the nine ensembles leads to a robust results. Over vast regions of northern Africa in summer, the regional model ensemble members produce agreement among at least seven of the nine realizations (77% or more). This level of agreement is much stronger than that of the AOGCMs used for the anomalous lateral boundary and SST constraints. Although the AOGCMs show little consensus in their predictions of West African rainfall at the end of the twenty-first century, it is worthwhile to note that with the exception of two outliers (one very wet and the other very dry), the models generally predict West African annual rainfall changes that are within ±0.5 mm/day. The regional model produces rainfall anomalies within this range between May and October. It may be that in the future annual rainfall changes over West Africa are near zero while, as simulated by the regional model, changes in the seasonal cycle are considerable.

Projections from the regional model are presented with focus on the climate change parameters most relevant for human impacts, and include the following:

- Over West Africa, including Senegal, Gambia, Guinea Bissau, Guinea, Sierra Leone, Liberia, Mali, Ivory Coast, Ghana, Burkina Faso, Togo, Benin, and Nigeria wetter conditions are projected during the month of May, with some regions receiving up to 50% more rainfall in the twenty-first century compared with the twentieth century. A mid-summer drought during June and July develops in this region late in the twenty-first century, with only half of the twentieth century rainfall delivered. Wetter conditions resume during August through October, with the exception of the Guinean Coast during August. During these months in the twenty-first century simulations there is an increase in intense rainfall events and the likelihood of flooding

in the late-summer.

- Over Central Africa, the regional model projects increases in rainfall during May and June over Cameroon, Central African Republic, Congo, and Democratic Republic of Congo with drying over Chad and Sudan and drier conditions in July. In August severe drying with <10% of the twentieth century rainfall covers southern Sudan, northern Democratic Republic of Congo, and in East Africa, Uganda, Rwanda, Kenya and western Ethiopia. Drying continues into September except over Central Africa Republic, where conditions are wetter in October.
- Generally in the twenty-first century there is an increase in the heat index over all of northern Africa throughout May–October. It is expected that the people in the Sahel region will be the most vulnerable, experiencing up to 160 days per year in the twenty-first century with a likely chance of heat stroke. At the next highest risk are the people of central equatorial Africa, Somalia, Kenya, Uganda, Gabon, and the Guinean Coast.

The RCM ensemble method produces precipitation projections for the end of the twenty-first century over northern Africa that are very consistent across the ensemble members. This is despite the fact that the AOGCMs which provide the lateral and surface boundary condition anomalies produce different projections themselves and inspires the question, why are the regional model ensemble members consistent when the global models are not? In the context of the current understanding of West African climate, we may expect SST warming in the twenty-first century to play a large, even dominant, role in determining the rainfall projections. However, the nine regional model simulations which are constrained with nine different twenty-first century SST distributions produce similar precipitation anomalies. This may be indicating that some other factors are more important in forcing centennial-scale climate change than SSTs in the future, or that the details of the SST increases are not

as important as the fact that they are all warming.

A better physical understanding of physical processes of change and the role of the various twenty-first century forcings, including SSTs, greenhouse gasses, and remote forcings, as well as the sensitivity to soil moisture initialization, on northern African rainfall also will support confidence in the results. Regional model simulations with twenty-first century CO_2 forcing alone, twenty-first century SSTA constraints alone, and idealized SSTAs will be analyzed in another paper to address these issues and understand the physical processes that support the changes reported here as well as the high level of consistency of the regional model ensembles. A dynamical analysis of the twenty-first century northern African circulation will also be presented.

The potential for continued improvement in this methodology is recognized. Including reliable interactive vegetation and dust models may reduce uncertainty, as well as broadening the ensemble to include additional members. Creating ensembles by including other regional models would be a valuable contribution to this method. Additionally, it may be advantageous to utilize simulations with other sets of land-surface models and parameterizations if the quality of the control simulation can be preserved. Forcing the regional model with greenhouse gas concentrations from other emissions scenarios would also be useful. Finally, long simulations instead of climate snapshots would be useful to better understand changes in interannual variability.

REFERENCES

Adler RF et al (2003) The version 2 Global Precipitation Climatology Project (GPCP) monthly precipitation analysis (1979-present). J Hydrometeorol 4:1147–1167.

Betts AK (1986) A new convective adjustment scheme. Part I: observational and theoretical basis. Q J R Meteorol Soc 112:677–691

Betts AK, Miller MJ (1986) A new convective adjustment scheme. Part II: single column tests using GATE wave, BOMEX, and Arctic air-mass data sets. Q J R Meteorol Soc 112:693–709

Biasutti M, Held IM, Sobel AH, Giannini A (2008) SST forcings and Sahel rainfall variability in simulations of the twentieth and twenty-first centuries. J Clim 21(14):3471–3486.

Caminade C, Terray L, Maisonnave E (2006) West African monsoon response to greenhouse gas and sulphate aerosol forcing under two emission scenarios. Clim Dyn 26:531–547

Chen F, Dudhia J (2001) Coupling an advanced land-surface/ hydrology model with the Penn State/NCAR MM5 modeling system. Part I: model description and implementation. Mon Weather Rev 129:569–585

Chen SH, Sun WY (2002) A one-dimensional time dependent cloud model. J Meteorol Soc Jpn 80:99–118

Cook KH (1999) Generation of the African easterly Jet and its role in determining West African precipitation. J Clim 12(5):1165–1184

Cook KH (2008) Climate science: the mysteries of Sahel droughts. Nat Geosci 1(10):647–648

Cook KH, Vizy EK (2006a) Coupled model simulations of the West African monsoon system: 20th century simulations and 21st century predictions. J Clim 19:3681–

3703

Cook KH, Vizy EK (2006b) South American climate during the Last Glacial Maximum: delayed onset of the South American monsoon. J Geophys Res 111. doi:10.1029/2005JD005980

Cook KH, Vizy EK (2008) Effects of twenty-first-century climate change on the Amazon rain forest. J Clim 21:542–560

Doherty R, Kutzbach J, Foley J, Pollard D (2000) Fully coupled climate/dynamical vegetation model simulations over Northern Africa during the mid-Holocene. Clim Dyn 16(8):561–573

Dudhia J (1989) Numerical study of convection observed during the winter monsoon experiment using a mesoscale two-dimensional model. J Atmos Sci 46:3077–3107

European Centre for Medium-Range Weather Forecasts (2002) The ERA-40 archive. ECMWF, Reading, p 40

Folland C, Owen J, Ward MN, Colman A (1991) Prediction of seasonal rainfall in the Sahel region using empirical and dynamic methods. J Forecast 10(1–2):21–56

Giannini A, Saravanan R, Chang P (2003) Oceanic forcing of Sahel rainfall on interannual to interdecadal time scales. Science 302(5647):1027–1030

Grodsky SA, Carton JA, Nigam S (2003) Near surface westerly wind jet in the Atlantic ITCZ. Geophys Res Lett 30(19)

Hagos SM, Cook KH (2007) Dynamics of the West African monsoon jump. J Clim 20(21):5264–5284

Hagos SM, Cook KH (2008) Ocean warming and late-twentieth-century Sahel drought and recovery. J Clim 21(15):3797–3814

Hoerling M, Hurrell J, Eischeid J, Phillips A (2006) Detection and attribution of twentieth-century northern and southern African rainfall change. J Clim

19(16):3989–4008

Hong S, Noh Y, Dudhia J (2006) A new vertical diffusion package with an explicit treatment of entrainment processes. Mon Weather Rev (134):2318–2341

Hsieh JS, Cook KH (2005) Generation of African easterly wave disturbances: Relationship to the African easterly jet. Mon Weather Rev 133(5):1311–1327

Hsieh JS, Cook KH (2007) A study of the energetics of African easterly waves using a regional climate model. J Atmos Sci 64(2):421–440

Hsieh JS, Cook KH (2008) On the instability of the African easterly jet and the generation of African waves: reversals of the potential vorticity gradient. J Atmos Sci 65(7):2130–2151

IPCC (2007) Climate change 2007: impacts, adaptation and vulnerability. In: Parry ML, Canziani OF, Palutikof JP, van der Linden PJ, Hanson CE (eds) Contribution of working group II to the fourth assessment report of the intergovernmental panel on climate change. Cambridge University Press, Cambridge, p 976

Janjic ZI (1990) The step-mountain coordinate: physical package. Mon Weather Rev 118:1429–1443

Janjic ZI (1994) The step-mountain Eta coordinate model: further developments of the convection, viscous sublayer and turbulence closure schemes. Mon Weather Rev 122:927–945

Janjic ZI (1996) The surface layer in the NCEP Eta Model. In: Eleventh conference on numerical weather prediction, Norfolk, VA, 19–23 August 1996. Amer Meteor Soc, Boston, MA, pp 354–355

Janjic ZI (2000) Comments on ‘‘development and evaluation of a convection scheme for use in climate models’’. J Atmos Sci 57:3686

Janjic ZI (2002) Nonsingular implementation of the Mellor-Yamada Level 2.5 Scheme

in the NCEP Meso model. NCEP Office Note No. 437, 61 pp

Joly M, Voldoire A, Douville H, Terray P, Royer JF (2007) African monsoon teleconnections with tropical SSTs: validation and evolution in a set of IPCC4 simulations. Clim Dyn 29(1):1–20

Kain JS, Fritsch JM (1990) A one-dimensional entraining detraining plume model and its application in convective parameterization. J Atmos Sci 47(23):2784–2802

Kain JS, Fritsch JM (1993) Convective parameterization for mesoscale models: the Kain–Fritcsh scheme. The representation of cumulus convection in numerical models. Meteor Monogr 24:165–170

Kalnay E et al (1996) The NCEP/NCAR 40-Year Reanalysis Project. Bull Am Meteorol Soc 77:437–471

Koster RD et al (2004) Regions of strong coupling between soil moisture and precipitation. Science 305(5687):1138–1140

Lamb PJ (1978) Case studies of Tropical Atlantic surface circulation patterns during recent sub-Saharan weather anomalies: 1967 and 1968. Mon Weather Rev 106:482–491

Lin YL, Farley RD, Orville HD (1983) Bulk parameterization of the snow field in a cloud model. J Appl Meteorol 22:1065–1092

Liu Z, Wang Y, Glallimore R, Notaro M, Prentice IC (2006) On the cause of abrupt vegetation collapse in North Africa during the Holocene: climate variability vs. vegetation feedback. Geophys Res Lett 33. doi:10.1029/2006GL028062

Meehl GA, Covey C, Delworth T, Latif M, McAvaney B, Mitchell JFB, Stouffer RJ, Taylor KE (2007) The WCRP CMIP3 multimodel dataset: a new era in climate change research. Bull Am Meteorol Soc 88:1383–1394

Mellor GL, Yamada T (1982) Development of a turbulence closure model for geophysical fluid problems. Rev Geophys 20:851– 875

Mlawer EJ, Taubman SJ, Brown PD, Iacono MJ, Clough SA (1997) Radiative transfer for inhomogeneous atmosphere: RRTM, a validated correlated-k model for the longwave. J Geophys Res 102(D14):16663–16682

Monin AS, Obukhov AM (1954) Basic laws of turbulent mixing in the surface layer of the atmosphere. Contrib Geophys Inst Acad Sci USSR 151:163–187 (in Russian)

New M, Hulme M, Jones P (1999) Representing twentieth century space–time climate variability. Part I: development of a 1961– 1990 mean monthly terrestrial climatology. J Clim 12:829–856

Paeth H, Thamm HP (2007) Regional modelling of future African climate north of 15 degrees S including greenhouse warming and land degradation. Clim Change 83(3):401–427

Paeth H, Born K, Girmes R, Podzun R, Jacob D (2009) Regional climate change in tropical and northern Africa due to greenhouse forcing and land use changes. J Cilm 22(1):114–132

Patricola CM, Cook KH (2007) Dynamics of the West African monsoon under mid-Holocene precessional forcing: regional climate model simulations. J Clim 20(4):694–716

Patricola CM, Cook KH (2008) Atmosphere/vegetation feedbacks: A mechanism for abrupt climate change over northern Africa. J Geophys Res 113. doi:10.1029/2007JD009608

Rojas M, Seth A (2003) Simulation and sensitivity in a nested modeling study for South America. Part II. GCM boundary forcing. J Clim 16:2454–2471

Rutledge SA, Hobbs PV (1984) The mesoscale and microscale structure and organization of clouds and precipitation in midlatitude cyclones. XII: a diagnostic modeling study of precipitation development in narrow cold-frontal

rainbands. J Atmos Sci 41(20):2949–2972

Seth A, Rojas M (2003) Simulation and sensitivity in a nested modeling study for South America. Part I. Reanalysis boundary forcing. J Clim 16:2437–2453

Skamarock WC, Klemp JB, Dudhia J, Gill DO, Barker DM, Wang W, Powers JG (2005) A description of the Advanced Research WRF Version 2. NCAR Tech. Note, ncar/TN-468+STR, 88 pp

Smirnova TG, Brown JM, Benjamin SG (1997) Performance of different soil model configurations in simulating ground surface temperature and surface fluxes. Mon Weather Rev 125:1870– 1884.

Smirnova TG, Brown JM, Benjamin SG, Kim D (2000) Parameterization of cold season processes in the MAPS land-surface scheme. J Geophys Res 105:4077–4086

Steadman RG (1979) The assessment of sultriness. Part I: a temperature-humidity index based on human physiology and clothing science. J Appl Metab 18(7):861–873

Tao WK, Simpson J, McCumber M (1989) An ice-water saturation adjustment. Mon Weather Rev 117:231–235

Vizy EK, Cook KH (2002) Development and application of a mesoscale climate model for the tropics: influence of sea surface temperature anomalies on the West African monsoon. J Geophys Res 107. doi:10.1029/2001JD000686

Vizy EK, Cook KH (2003) Connections between the summer east African and Indian rainfall regimes. J Geophys Res 108. doi: 10.1029/2003JD003452

Vizy EK, Cook KH (2005) Evaluation of Last Glacial Maximum sea surface temperature reconstructions through their influence on South American climate. J Geophys Res 110. doi:10.1029/ 2004JD005415

Ward MN (1998) Diagnosis and short-lead time prediction of summer rainfall in

Tropical North Africa at interannual and multidecadal timescales. J Clim 11:3167–3191

Xue YK, Shukla J (1993) The influence of land-surface properties on Sahel climate. 1. Desertification. J Clim 6(12):2232–2245

Xue YK, Shukla J (1996) The influence of land surface properties on Sahel climate. 2. Afforestation. J Clim 9(12):3260–3275

Zeng N, Neelin JD, Lau KM, Tucker CJ (1999) Enhancement of interdecadal climate variability in the Sahel by vegetation interaction. Science 286:1537–1540.

CHAPTER 2

NORTHERN AFRICAN CLIMATE AT THE END OF THE TWENTY-FIRST CENTURY: FORCING FACTORS AND CLIMATE CHANGE PROCESSES

2.1 Introduction

There is a vital need for trustworthy predictions of northern African climate since the region is highly agricultural and prone to devastating droughts. Simulations from the majority of the atmosphere-ocean general circulation models (AOGCMs) run for the Fourth Assessment Report of the Intergovernmental Panel on Climate change (IPCC AR4; IPCC 2007) produce weak annual-mean rainfall projections over northern Africa. One model produces extreme rainfall decreases (Held et al. 2005), and one produces extreme increases, but these outlier model simulations may not be accurate (Cook and Vizy 2006; Giannini et al. 2008; Cook 2008).

Many of the AOGCMs validate poorly over northern Africa, e.g., missing the movement of the precipitation maximum into the Sahel and misrepresenting basic circulation features of the West African monsoon (Cook and Vizy 2006). Patricola and Cook (2009) developed an approach for projecting future climate that combines the advantages of global and regional modeling. They produce a nine-member ensemble of climate simulations for the end of the twenty-first century over northern Africa by constraining a regional climate model with SST and lateral boundary condition anomalies derived from nine AOGCMs. The rainfall predictions produced by the regional model ensembles have a very good consensus, with at least 77% agreement over vast regions of northern Africa. This is a substantial improvement over the projections from the AOGCMs that provided the anomalous SST and lateral boundaries to constrain the regional model, even though those SST and lateral

boundary predictions vary among the nine global models.

Patricola and Cook (2009) describe the prediction method in detail, and report climate change predictions. Confidence in these predictions is founded on the agreement among the ensemble members, and on the ability of the regional model to capture an accurate portrayal of the present day climate dynamics of northern Africa. The purpose of this paper is to further enhance confidence in these predictions and to expand our basic understanding of the region's climate by developing a physical understanding of the simulated climate change through analysis of the dynamics of the West African monsoon and East African region in the future. We investigate the role of individual climate change forcing factors, and explain why the rainfall predictions are similar among the nine future regional model ensembles despite differences in the forcing, especially SSTAs, taken from the AOGCM projections.

2.2 Background

In this section, we summarize the climate predictions of Patricola and Cook (2009), hereafter PC09, so that we may build on those results in this paper. In addition, we review present day relationships between variability in precipitation and circulation features over northern Africa to guide the supporting dynamical analysis of the future climate. For a review of AOGCM predictions, the ability of models to simulate present day relationships between SSTs and West African rainfall, and land-atmosphere interactions, please see PC09.

2.2a Northern African climate predictions from PC09

The AOGCM simulations conducted for the IPCC AR4 (IPCC 2007) produced summer rainfall predictions for northern Africa at the end of the twenty-first century that, as Cook (2008) notes, are clustered around zero with the exception of one

extremely wet and one extremely dry outlier. It is unclear from this multi-model ensemble approach whether West African rainfall is expected to increase, decrease, or remain about the same in the future. A validation-based approach, in which the future projections are considered from only the models that reasonably represent the present day climate and one prominent mode of interannual variability over West Africa, suggests that while a realistic representation of the control climate supports confidence, it is not sufficient for reliable prediction. This result emphasizes the need for an approach that relies on our physical understanding of the region, as in Cook and Vizy (2006).

PC09 discuss the disadvantages that arise from depending solely on global models to simulate regional climate change, specifically difficulty in representing the present day climate and coarse model resolution that does not resolve the observed low-level jets (e.g., the West African westerly jet and Turkana jet) and meridional gradients in precipitation, moisture, and temperature. In order to address these issues, PC09 developed a method that combines the advantages of both the global and regional modeling approaches. Using a regional model offers the benefit of simulating at an appropriate resolution, chosen through testing to capture important surface and atmospheric features, as well as producing model output that is more suitable for impacts analysis. In addition, regional modeling offers the ability to select an optimal set of parameterizations and land surface model for a realistic simulation of northern African climate, which PC09 demonstrated is critically important. The coupled global models provide predictions of SST and lateral boundary condition anomalies that are necessary to constrain the regional model for future climate simulations.

The method used by PC09 devotes particular attention to uncertainties in future SST and lateral boundary conditions by forming an ensemble of nine future climate simulations with boundary conditions derived from nine different AOGCMs. The

formulation of boundary conditions in PC09 differs from the traditional downscaling method, in which SSTs and lateral boundary conditions are applied directly from an AOGCM to a regional model. Here, future boundary conditions are applied to the regional model as anomalies that are added to the present day climatology from reanalysis products in order to reduce the impact of GCM error on the regional projections, and to produce a well-validated control climate constrained by reanalysis products. The AOGCM anomalies are differences between the present day (1981-2000) and future (2081-2100) climatologies forced by the SRESA2 emissions scenario (IPCC 2000).

Figure 2.1 shows the ensemble-averaged monthly rainfall predictions for 2081-2100 from PC09's regional climate model simulations, with regions where less than 77% of the ensemble members (7 out of 9) agree on the sign of the precipitation anomaly shaded in grey. The nine ensemble members produce monthly rainfall predictions that are consistent in sign over much of northern Africa (Fig. 2.1). Wetter conditions are predicted over the Guinean Coast region in May, September, and October with drying from June through August. Over the Sahel region, drier conditions are predicted in June and wetter conditions that may result in an increased flood risk persist from August through October. In East Africa, severe drying is centered over southern Sudan and Uganda in August and September (Fig. 2.1d-e).

Figure 2.2 shows the monthly and MJJASO averaged, area-averaged precipitation anomalies from each individual ensemble member over West Africa to provide more detailed information about the level of agreement of the ensemble average rainfall predictions, and the averaging regions (Fig. 2.2a) used throughout the analysis which include the Guinean Coast (4°N – 7.5°N and 18°W – 10°E) and Sahel (8°N – 14°N and 18°W – 18°E) in West Africa, and East Africa (2°S-10°N and 28°E-36°E). Over the Guinean Coast region in May, when at least 77% of the ensemble

members predict wetter conditions (Fig. 2.1a), none of the ensemble members are drastic outliers in the rainfall predictions (Fig. 2.2b). This holds true for each month in which 77% of the ensemble members agree on the sign of the rainfall anomaly over both the Guinean Coast (Fig. 2.2b) and Sahel (Fig. 2.2c) regions. In addition, when the ensemble members do not agree on the sign of the rainfall prediction, for example, over the Sahel in May (Fig. 2.1a), the individual model predictions (Fig. 2.2c) cluster close to zero, and none of the members are outliers. In July, when predictions are also uncertain over the Sahel (Fig. 2.1c), four of the members produce drying of 1-2 mm/day, four of the models produce near-zero change, and one model produces wetter conditions of ~0.75 mm/day (Fig. 2.2c), suggesting the Sahel may be weakly dry during July in the future. Even when the ensembles disagree about the sign of the rainfall anomaly the range of the predicted anomalies is small, promoting confidence in the precipitation predictions.

The May – October average for each of the nine future regional climate ensemble predictions for the Guinean Coast and Sahel regions is in the last column of Figures 2.2b and c, respectively. For both regions, the six-month averages are clustered closely about zero change; over the Guinean Coast the anomalies are evenly distributed around zero, while over the Sahel the anomalies tend to be positive. This result is similar to the summer rainfall predictions for 2100 from the AOGCMs run for the IPCC AR4, which are clustered around +/- 0.5 mm/day with two outliers reaching about 2 mm/day and -2.75 mm/day, suggesting that on the seasonal timescale Sahelian rainfall anomalies in the future may indeed be weak. This is not the case for the monthly rainfall predictions, however, and this result highlights the importance of analyzing rainfall predictions on at least the monthly timescale. Information that is critical for impacts analysis can be missed by focusing on only the annual or seasonal averages.

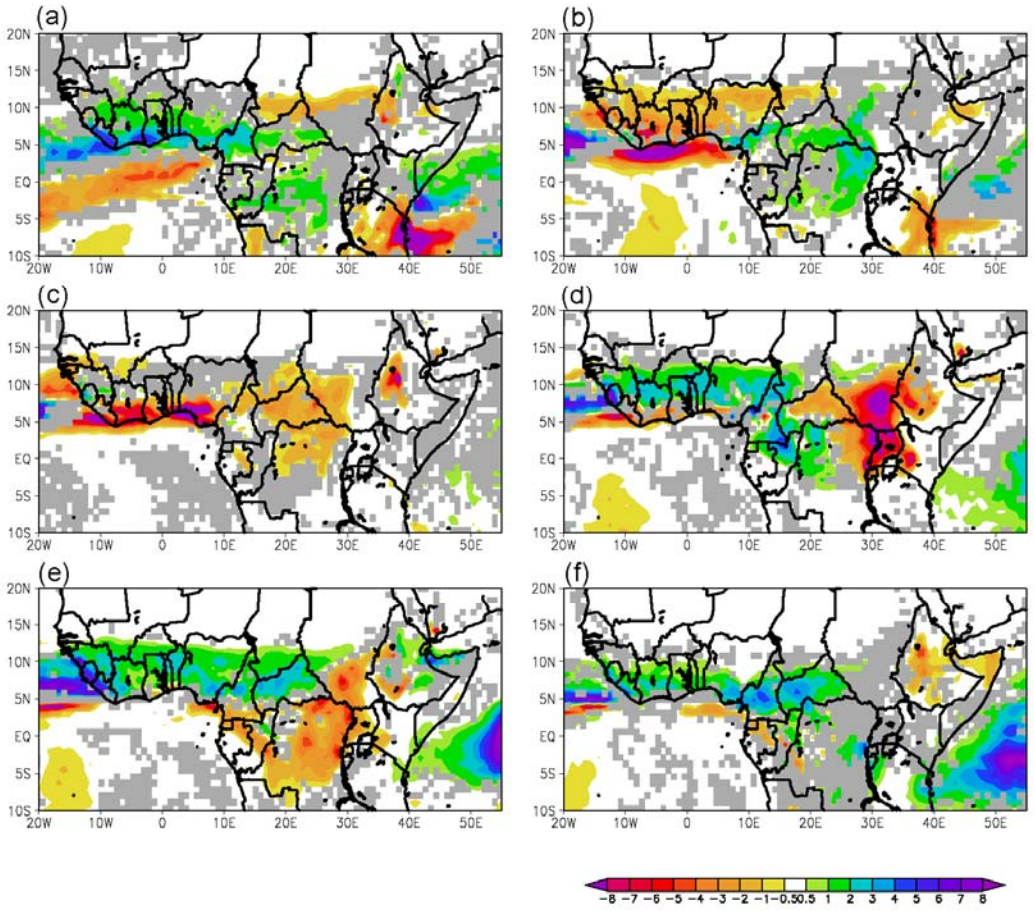

Figure 2.1: Ensemble averaged precipitation anomalies (mm/day) from the fully-forced future simulations for (a) May, (b) June, (c) July, (d) August, (e) September, and (f) October. Areas where less than 77% of the ensemble members agree are shaded grey.

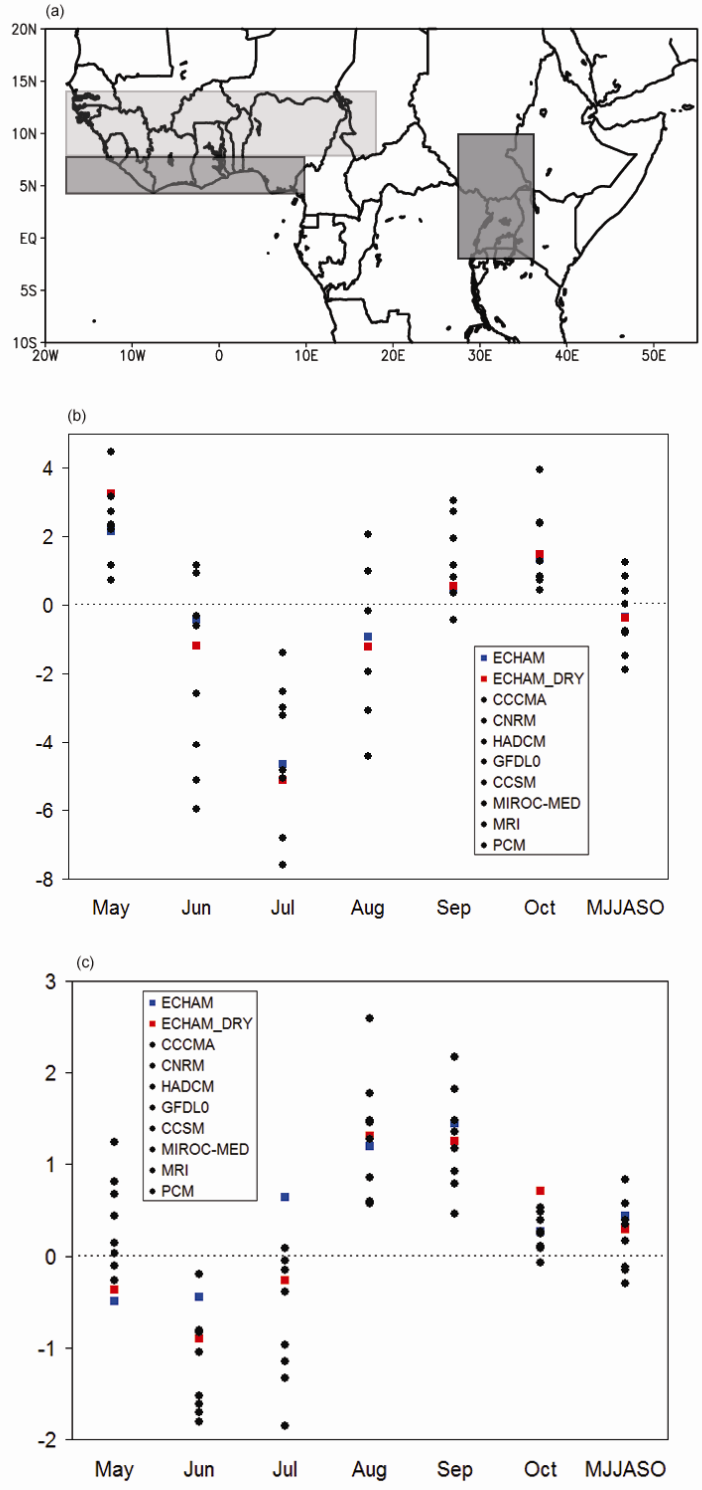

Figure 2.2: (a) Averaging regions including the Sahel (light grey), Guinean Coast (medium grey), and East Africa (dark grey). Monthly and MJJASO averaged precipitation anomalies from the nine individual fully-forced future simulations and the 21_DRY simulation over land only for the (b) Guinean Coast and (c) Sahel regions. Units are mm/day.

2.2b Climate variability: West Africa

One way to support confidence in projections of future climate change is to understand the physical processes responsible for the change, and evaluate the extent to which those processes are reasonable given our current understanding of the system. Here we briefly review the known relationships between circulation features and northern African rainfall to assist in the analysis below.

The West African monsoon is supported by moist southerly winds from the Gulf of Guinea that converge with the dry northeasterly Harmattan winds (e.g. Cook 1997; Sultan and Janicot 2003). Moisture transport associated with the more recently identified low-level West African westerly jet (WAWJ) on the west coast near 10°N – 12.5°N (Grodsky et al. 2003) provides an important additional moisture source, especially for the Sahel (Pu and Cook 2010a). Variability in the WAWJ is associated with Sahel rainfall on decadal timescales, with a stronger jet and wetter conditions tending to occur together (Pu and Cook 2010b). The WAWJ is also important on geological timescales, with a stronger jet supporting the "green Sahara" conditions in regional climate simulations of 6,000 years ago (Patricola and Cook 2007). This jet may also be an important feature in abrupt climate change processes, as abrupt changes in the strength of the jet are simulated under smooth idealized vegetation changes in a regional climate model (Patricola and Cook 2008). The African easterly jet (AEJ), located on the west coast of Africa at about 15°N and 625 hPa, is a moisture sink for the West African monsoon (Cook 1999). In today's climate, a stronger AEJ that is located anomalously south is associated with dry conditions in the Sahel on interannual time scales (Newell and Kidson 1984; Fontaine et al. 1995; Grist and Nicholson 2001).

Many studies have found relationships between present day variability in West African rainfall and Atlantic SSTs on interannual to decadal timescales. Wetter (drier)

conditions over the Sahel tend to be associated with warmer (cooler) northern and cooler (warmer) southern tropical and subtropical Atlantic SSTs (Lamb 1978a and 1978b; Folland et al. 1986; Druyan 1991; Folland et al. 1991; Lamb and Peppler 1992; Ward 1998). SSTs in the Gulf of Guinea exert a significant influence on West African rainfall as well. One frequently-observed mode of interannual variability is manifest as a dipole pattern with wet (dry) conditions over the Guinean Coast region and dry (wet) conditions over the Sahel in association with warm (cool) Gulf of Guinea SSTs (Nicholson 1980; Janicot 1992; Rowell et al. 1995). Regional climate model simulations capture this dipole pattern (Vizy and Cook 2002). The drying over the Sahel is associated with subsidence that results from shrinking of planetary vorticity and enhanced relative vorticity advection in the outflow from the Saharan high, while the wetter conditions over the Guinean Coast are linked to an increase in moisture transport across the Guinean coast through enhanced evaporation over the ocean, and not through a strengthening of the low-level southerly monsoon flow.

Both observations and model simulations reveal a relationship between Mediterranean SSTs and Sahel rainfall such that warmer (cooler) SSTs in the Mediterranean are associated with a wetter (drier) Sahel, most strongly on the decadal time scale (Rowell 2003). AGCM simulations indicate that a warm Mediterranean results in increased local evaporation, and that additional moisture is advected to the south at low levels and supports moisture convergence anomalies over the Sahel. The rainfall further is enhanced by several positive feedbacks, including a weakening of the African easterly jet.

Indian Ocean SSTs have been found to influence Sahelian rainfall on decadal timescales as well, with overall warming contributing to drier conditions (Giannini et al. 2003; Bader and Latif 2003; Lu and Delworth 2005) and dominating wetter conditions produced by a weakening of the meridional Indian Ocean SST gradient

(Chung and Ramanathan 2006). Climate simulations produce a Rossby wave response with convergence over the Indian Ocean and divergence over Africa due to Indian Ocean warming (Hagos and Cook 2008; Lu 2009). However, regional climate simulations demonstrate that the location of the subsidence depends on the scale and magnitude of the Indian Ocean forcing. Although the Indian Ocean was anomalously warm during both the 1980's and 1990's, the rainfall response over West Africa was different because the region of subsidence shifted to the west – off the coast – in the 1990's and allowed for the current observed recovery in Sahel rainfall (Hagos and Cook 2008).

2.2c Climate variability: East Africa

The Somali jet (Findlater 1966, 1977) is a cross-equatorial low-level jet that is northerly over the Horn of Africa and turns westerly into the Arabian Sea, transporting significant amounts of moisture over East Africa and into the Asian monsoon. A strong Somali jet is associated with above normal rainfall over the Horn of Africa (Segele et al. 2009) as well as wetter conditions along the west coast of India (Halpurn and Woiceshyn, 2001). Camberlin (1997) finds that, throughout the twentieth century, above normal sea-level pressure over Bombay and Indian drought in July through September are not only strongly correlated with dry conditions in the Ethiopian Highlands, Uganda, and western Kenya, but also precede them, suggesting that the Indian monsoon may be in part controlling rainfall in East Africa. Vizy and Cook (2003) also find that a strong (weak) Somali jet occurs with a wet (dry) Indian monsoon in regional model simulations but, unlike the observations, northern Ethiopian drying accompanied by decreased convergence and stronger flow in the Somali jet entrance region occurs with an enhanced Indian monsoon.

Another circulation feature over East Africa that is related to rainfall variations

is the Turkana Channel jet, which is a low-level southeasterly jet that funnels between the Ethiopian Highlands and the East African highlands. It persists throughout the year, and is formed by orographic channeling of the flow (Kinuthia and Asnani, 1982; Kinuthia 1992). A negative correlation between the strength of the Turkana jet and the Somali jet is found in regional model simulations (Vizy and Cook 2003), although the authors note that the Turkana jet should be investigated further with higher resolution simulations. Regional model simulations also produce a negative correlation between the strength of the Turkana jet and rainfall over that region, with a stronger (weaker) jet associated with stronger (weaker) low-level divergence (Sun et al. 1999).

2.3 Methodology

Regional climate model (RCM) simulations are conducted with the Weather Research and Forecasting Model (WRF; Skamarock et al. 2005) version 2.2 with a set of parameterizations chosen for an optimal simulation of northern African climate (see PC09). The horizontal resolution is 90 km, and the domain includes Africa, the Mediterranean Sea, and the tropical and subtropical Atlantic and Indian Oceans (Fig. 2.18).

This study is based on the present day and future simulations described in PC09 and listed in the first 2 rows of Table 2.1. These are climate mode simulations that include one control simulation representative of 1981-2000, with SSTs and lateral boundary conditions (LBCs) prescribed from climatological monthly means of the European Center for Medium Range Weather Forecasting ERA-40 reanalysis (ECMWF 2002) and the National Center for Environmental Prediction/National Center for Atmospheric Research (NCEP/NCAR; Kalnay et al. 1996) reanalysis, respectively. The atmospheric CO_2 concentration is set to 330 ppm. The integrations

are run from March 15 to October 31, with March 15 – April 30 disregarded for spin-up. PC09 provide a detailed description of this simulation along with validation that demonstrates that the control simulation is comparable to or better than those from the current generation of AOGCMs.

Table 2.1: List of simulations.

Name	CO_2 (ppm)	SST	LBC	AOGCM providing SSTA and LBCA	Soil conditions
control (1 run)	330	1980-2000	1980-2000	--	1980-2000
fully-forced future (9 runs)	757	2081-2100	2081-2100	9 AOGCMs	1980-2000
SSTA_only (9 runs)	330	2081-2100	1980-2000	9 AOGCMs	1980-2000
2K_SSTA (1 run)	330	uniform 2K	1980-2000	--	1980-2000
CO2_only (1 run)	757	1980-2000	1980-2000	--	1980-2000
LBCA_only_EC (1 run)	330	1980-2000	2081-2100	ECHAM	1980-2000
SSTA+LBCA_EC (1 run)	330	2081-2100	2081-2100	ECHAM	1980-2000
21_DRY (1 run)	757	2081-2100	2081-2100	ECHAM	4 dry years

The future simulations are an ensemble of nine simulations that represent the climate for 2081-2100. Each simulation is constrained by SST anomalies (SSTAs) and lateral boundary condition anomalies (LBCAs) from one of nine AOGCMs, and the CO_2 concentration is increased to 757 ppm based on the SRESA2 emissions scenario (IPCC 2000). Boundary conditions are derived from nine AOGCM simulations which are included in the World Climate Research Programme's (WCRP's) Coupled Model Intercomparison Project phase 3 (CMIP3) multimodel dataset (Meehl et al. 2007) and archived by the Program for Climate Model Diagnosis

and Intercomparison. Please refer to PC09 for a detailed description of these simulations.

The moisture budget, similar to that derived in Lenters and Cook (1995), is used to develop an understanding of the connections between simulated precipitation and circulation anomalies. The vertically-integrated atmospheric moisture budget is

$$P = E + C + A + R\,, \tag{2.1}$$

which calculates the contributions to precipitation (P) from evaporation (E), vertically-integrated moisture convergence (C) and advection (A), and the residual (R) which includes topographical effects as well as numerical and sampling error. The contribution from vertically-integrated moisture convergence is

$$C = -\frac{1}{g\rho_w}\sum_{p=p_s}^{100hPa}(q\nabla_h \cdot \vec{V})\Delta p\,, \tag{2.2}$$

where g is the acceleration due to gravity, ρ_w is the density of water, p is pressure, p_s is surface pressure, q is the water vapor mixing ratio, $\vec{V}$ is the horizontal wind vector, and ∇_h is the horizontal divergence operator.

The contribution from vertically-integrated moisture advection is

$$A = -\frac{1}{g\rho_w}\sum_{p=p_s}^{100hPa}(\vec{V} \cdot \nabla_h q)\Delta p\,, \tag{2.3}$$

The moisture convergence and advection terms are expressed in component form as

$$C_M = -\frac{1}{g\rho_w}\sum_{p=p_s}^{100hPa}(q\nabla_h \cdot v)\Delta p\,, \tag{2.4}$$

$$C_Z = -\frac{1}{g\rho_w}\sum_{p=p_s}^{100hPa}(q\nabla_h \cdot u)\Delta p\,, \tag{2.5}$$

$$A_M = -\frac{1}{g\rho_w}\sum_{p=p_s}^{100hPa}(v\cdot\nabla_h q)\Delta p\,, \tag{2.6}$$

$$A_Z = -\frac{1}{g\rho_w}\sum_{p=p_s}^{100hPa}(u\cdot\nabla_h q)\Delta p\,, \tag{2.7}$$

where C_M (A_M) and C_Z, (A_Z), are vertically-integrated meridional and zonal moisture convergence (advection), respectively.

Fourteen additional simulations, also listed in Table 2.1, are conducted to better understand the role of individual climate forcings, namely, atmospheric CO_2 concentration, SSTAs, and LBCAs. An ensemble of nine simulations designed to isolate the impact of SSTAs on climate is forced with SSTAs for 2081-2100 from each of the nine AOGCMs (as in the fully-forced future runs, see Fig. 3 in PC09), with LBCs and CO_2 representing 1981-2000. Together these nine simulations are called "SSTA_only."

An idealized simulation, named "2K_SSTA," in which a uniform warming of 2K is added to the control SSTs throughout the integration is also conducted. The warming of 2K is chosen because it approximates the average SSTA projected by the nine AOGCMs over the tropical and subtropical Atlantic and Indian Oceans. As in the SST_only simulations, the LBCs and CO_2 concentration for the 2K_SSTA simulation are also taken from 1981-2000 values.

A single simulation, named "CO2_only," is forced with the CO_2 concentration for 2081-2100 (757 ppm) and constrained with lateral boundary conditions and SSTs from 1981-2000. Therefore, this simulation isolates the radiative effects of CO_2 increases within the regional model domain, excluding the effects of global CO_2 increases and SST changes.

We conducted one simulation (LBCA_only_EC) in which only the LBCs are changed from the present day control simulation, using anomalous LBCs from the

ECHAM model. This produced a climate state that is physically unrealistic because of inconsistencies between the lateral and surface boundary conditions. For this reason, the role of anomalous LBCs and SSTs are assessed together using a simulation named "SSTA+LBCA_EC" in which the 2081-2100 SSTAs and LBCAs derived from the ECHAM AOGCM are applied to the RCM, with CO_2 prescribed at the 1981-2000 concentration.

Although soil moisture and temperature are not prescribed within the RCM, the relative importance of the initialization of these variables in the future simulations is of concern, especially since there is no consensus regarding the role of northern African land conditions in determining future climate in the region (Paeth and Thamm 2007; Maynard and Royer 2004). In addition, land/atmosphere interactions are particularly strong over the Sahel (Xue and Shukla 1993; Xue and Shukla 1996; Koster et al 2004), and our previous modeling experience suggests that soil moisture and temperature initialization can strongly impact the simulation of present day West African climate. We conduct a sensitivity simulation to evaluate the role of the initialization of soil variables in the fully-forced future simulations. This simulation is designed to address the uncertainty in the twenty-first century soil moisture and temperature that may originate from, for example, rainfall anomalies during the winter and spring months at the end of the twenty-first century that could impact soil conditions in March when the RCM simulations are initialized. For this simulation, named "21_DRY," the soil moisture and temperature at 4 levels are initialized from the March mean for 1983, 1990, 1998, and 2000 from the European Center for Medium Range Weather Forecasting ERA-40 reanalysis (ECMWF 2002). These years are selected because they are the four driest March distributions during the 1981-2000 period. (Recall that for all other simulations, soil moisture and temperature are initialized from the average of March over the years 1981-2000.) SSTAs and LBCAs

are derived from the ECHAM simulation, and the CO_2 concentration is 757 ppm.

Precipitation anomalies from the nine fully-forced future simulations and the 21_DRY simulation for the Guinean Coast and Sahel regions are shown in Figures 2.2a and b. For both regions and for all months, precipitation anomalies from the 21_DRY simulation (red dot) are within the range of the fully-forced future precipitation anomalies that were initialized with climatological soil conditions (black and blue dots). The results from this sensitivity test illustrate that the uncertainty in the initialization of soil moisture and temperature is insignificant compared to the SST, LBC, and CO_2 forcings.

2.4 Results

Regional moisture budget analyses for the Guinean coast, Sahel, and East African regions are examined below to relate precipitation and circulation anomalies, and improve our understanding of the processes of climate change in the projections. This analysis is followed by an examination of the role of the individual climate forcings, and an investigation of why the ensemble rainfall predictions are similar despite differences in the future climate forcings, specifically the SSTAs.

2.4a Analysis of Guinean Coast precipitation anomalies

The terms of the moisture budget, including precipitation, evaporation, and vertically-integrated meridional and zonal moisture convergence and advection, are plotted in Figures 2.3a and b, as anomalies for the end of the twenty-first century, and area-averaged over the Guinean Coast region (4°N – 7.5°N and 18°W – 10°E ; Fig. 2.2a). Monthly anomalies in the residual contribute relatively little to the anomalous moisture budget balance of the fully-forced future climate, so are not considered further. Anomalies in vertically-integrated zonal and meridional moisture

convergence emerge as the dominant terms of the moisture budget for the fully-forced future climate over the Guinean Coast region and relate strongly to the predicted precipitation increases in May and August to October and decreases in July to August (Fig. 2.3a). Contributions from evaporation and vertically-integrated moisture advection anomalies are relatively small from May through October (Fig. 2.3b).

Vertical profiles of the area-averaged zonal and meridional moisture convergence anomalies due to the full forcings (Fig. 2.3c and d, respectively) together with the vertically-integrated moisture budget (Fig. 2.3a and b) enable a better understanding of the connections between precipitation and circulation changes by revealing which levels contribute to the moisture convergence anomalies. The wet period in May, with anomalies reaching nearly 7 mm/day, is supported by anomalous zonal moisture convergence (Fig. 2.3a) that extends from the surface to 550 hPa (Fig. 2.3c) as well as anomalous meridional moisture convergence (Fig. 2.3a) at low-and mid-levels (Fig. 2.3d).

Cross sections of the zonal and meridional wind on the western and southern edge of the Guinean Coast averaging region allow us to relate the changes in regional-scale moisture convergence to the larger-scale circulation and moisture fields. Figures 2.4a – c show the zonal wind averaged from 4°N – 7.5°N along the western edge of the Guinean Coast averaging region at 18°W for the control simulation, ensemble averaged fully-forced future simulations, and the difference, respectively. The anomalous zonal moisture convergence that supports wetter conditions along the Guinean Coast region in late May is related to zonal wind anomalies along the west coast of Africa. Figures 2.4d – f show the meridional wind averaged from 18°W – 10°E along the southern edge of the Guinean Coast region at 4°N for the control simulation, ensemble averaged fully-forced future simulations, and the difference. Although the southerly monsoon flow from the surface to about 850 hPa (Fig. 2.4d) is

one of the primary sources of moisture for the West African monsoon, in early May the anomalous meridional moisture convergence in the future is not related to a strong change in this monsoon flow (Fig. 2.4f). These cross sections suggest that while the anomalies in meridional wind contribute weakly to the anomalous moisture convergence over the Guinean Coast region in May, increases in atmospheric moisture are very important.

The importance of atmospheric moisture anomalies in supporting the future precipitation anomalies is confirmed by comparison of Figure 2.5, which shows the monthly geopotential height anomalies (shaded) and wind (vectors) at 925 hPa for the future, and Figure 2.6, which shows the anomalous water vapor mixing ratio (shaded) and moisture transport vectors (i.e., the horizontal wind scaled by water vapor mixing ratio) at 925 hPa. In May, while anomalies in the southerly monsoon flow (Fig. 2.5a) are weak, positive atmospheric moisture anomalies over the Gulf of Guinea contribute to increased moisture transport onto the continent (Fig. 2.6a), supporting the low-level meridional convergence anomalies (Fig. 2.3d).

From June through mid-August, precipitation anomalies over the Guinean Coast region (Fig. 2.3a) peak close to -9 mm/day, and are supported by anomalous low- and mid-level zonal (Fig. 2.3c) and low-level meridional (Fig. 2.3d) moisture divergence. The anomalous zonal moisture divergence is related to both a weakening of the low-level westerlies and strengthening of the mid-level easterlies along the west coast of Africa (Fig. 2.4a-c), while the anomalous low-level meridional divergence (Fig. 2.3d) is related to a weaker and more shallow southerly monsoon flow (Fig. 2.4d-f). The drier summertime conditions over the Guinean Coast region are related primarily to circulation changes, not atmospheric moisture anomalies (Figs. 2.5b-c and 2.6b-c).

Projected conditions are wetter in the future over the Guinean Coast region

from mid-August through October. From mid-August through early September, these precipitation increases are supported by anomalous zonal moisture convergence (Fig. 2.3a and c) that is related to a slight strengthening of the low-level westerly flow (Fig. 2.4a-c) as well as increases in atmospheric moisture (Figs. 2.5d and 2.6d). Anomalous meridional moisture convergence between the surface and 950 hPa and 850 – 650 hPa that dominates anomalous meridional moisture divergence from 950 – 850 hPa contributes to wetter conditions from mid-September through October (Fig. 2.3a and d). These meridional convergence anomalies are related to a monsoon flow that is stronger near the surface, but shallower, with a weaker mid-level northerly return flow in the future (Fig. 2.4c-f).

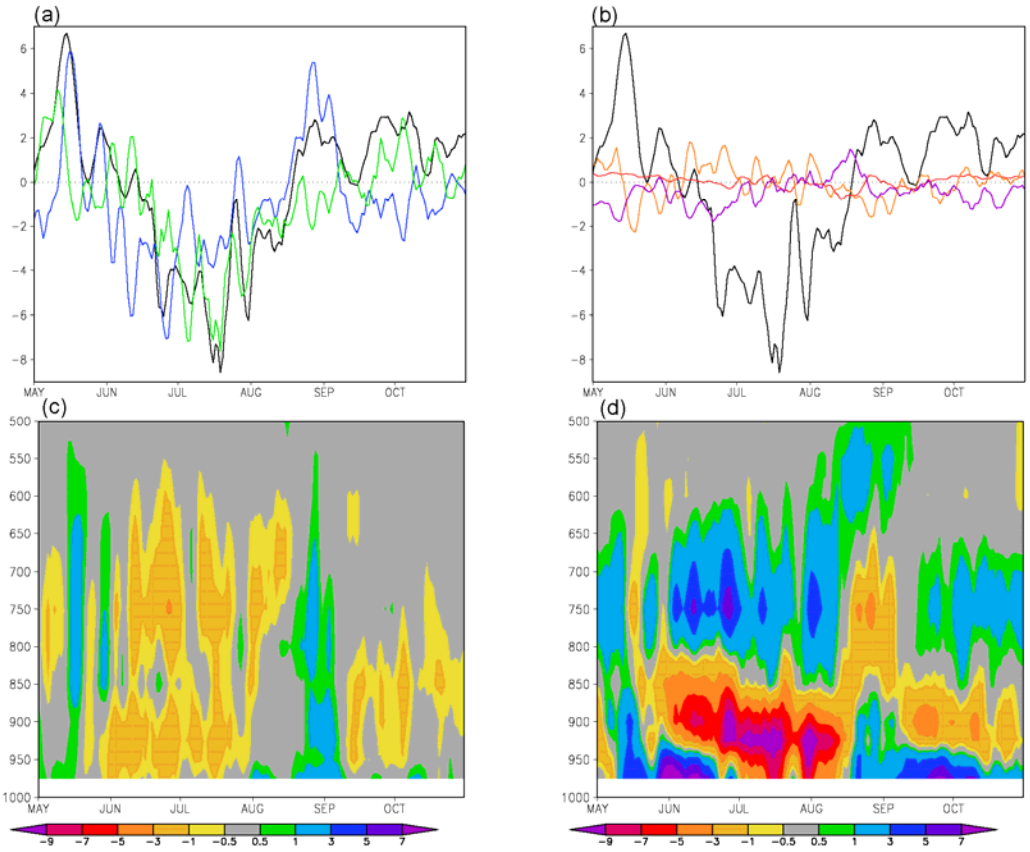

Figure 2.3: The 5-day running mean of the area-averaged, ensemble averaged anomalies in (a) precipitation (black), vertically-integrated zonal moisture convergence (blue) and meridional moisture convergence (green), (b) evaporation (red), and vertically-integrated meridional moisture advection (orange), and zonal moisture advection (purple) from the fully-forced RCM simulations for the Guinean Coast region. Units are mm/day. Vertical profiles of the 5-day running mean of the area-averaged, ensemble averaged anomalies in (c) zonal and (d) meridional moisture convergence from the fully-forced RCM simulations for the Guinean Coast region. Units are 10^{-3}-(m/s^2)(kg H_2O/kg air).

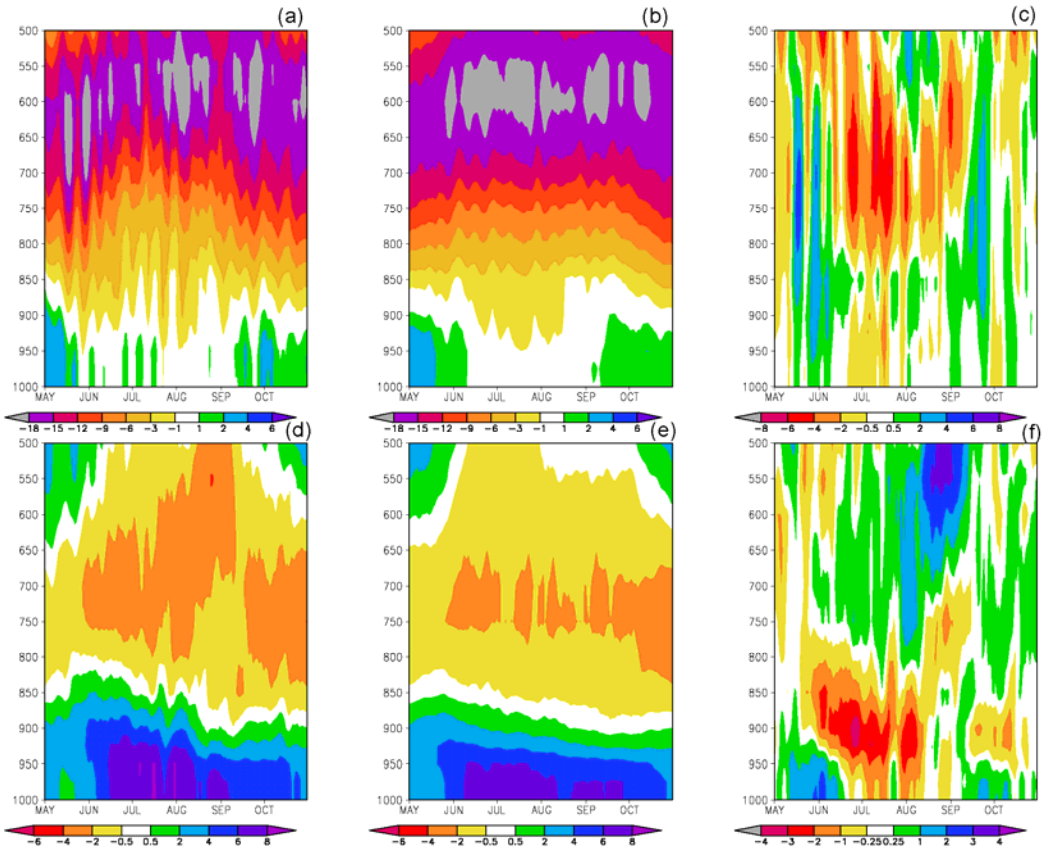

Figure 2.4: The 5-day running mean of the zonal wind profiles at 18°W, averaged over 4°N-7.5°N for the (a) control simulation, (b) ensemble average of the fully-forced future simulations, and (c) difference. The 5-day running mean of the meridional wind profiles at 4°N, averaged over 18°W-10°E for the (d) control simulation, (e) ensemble average of the fully-forced future simulations, and (f) difference. Units are m/s.

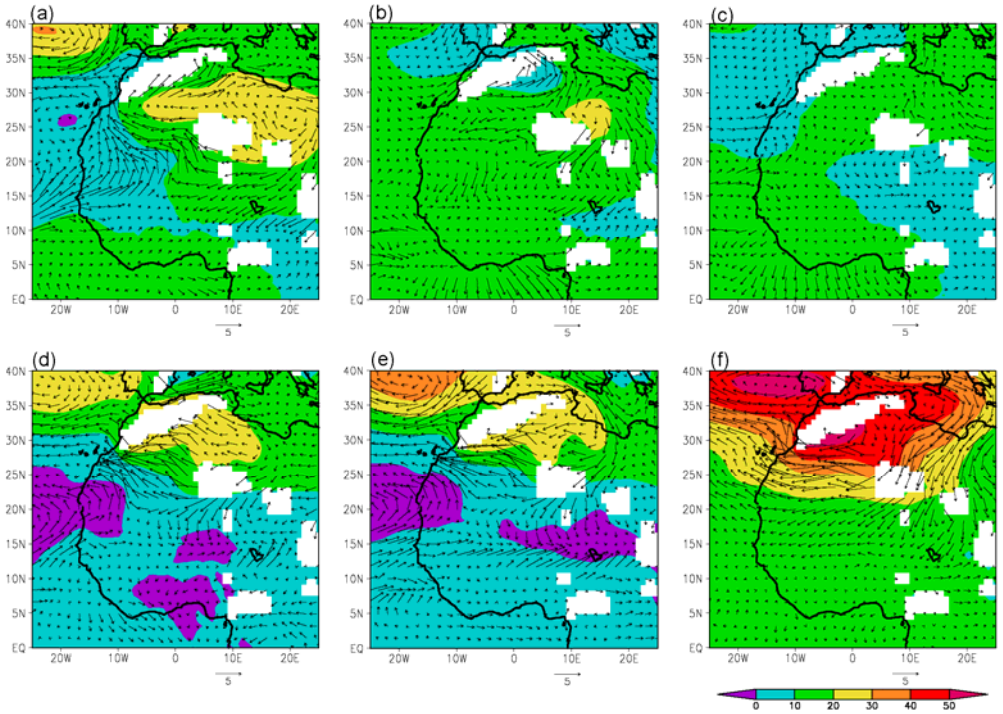

Figure 2.5: Ensemble averaged anomalies in geopotential heights (m, shaded) and wind (m/s, vectors) at 925hPa for (a) May, (b) June, (c) July, (d) August, (e) September, and (f) October from the fully-forced future simulations.

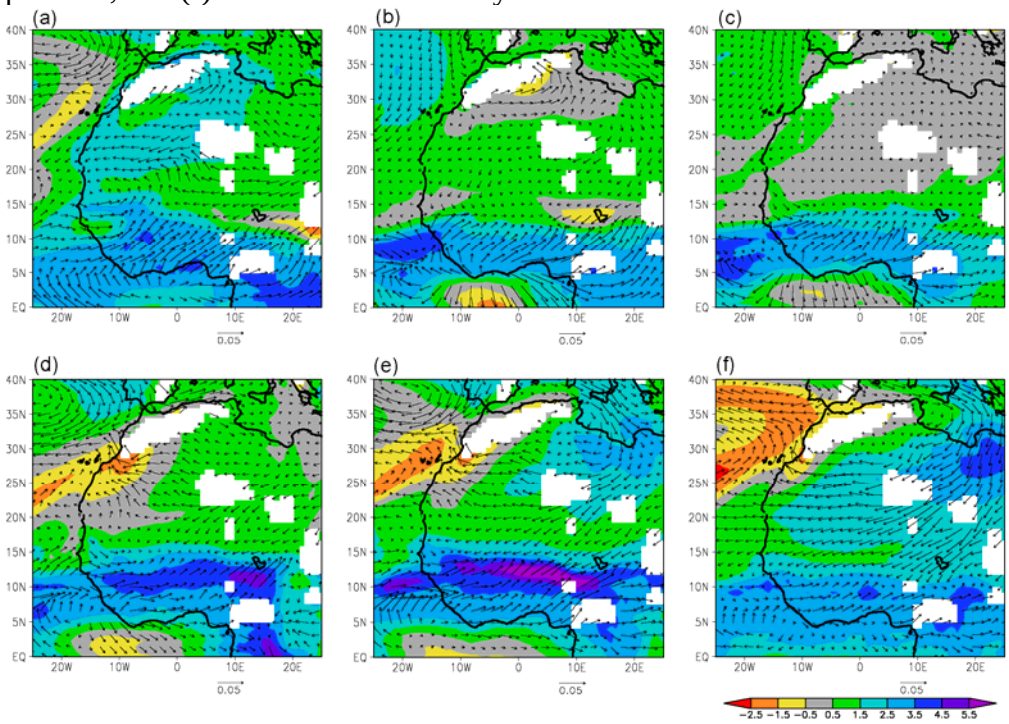

Figure 2.6: Ensemble averaged anomalies in water vapor mixing ratio (kg H_2O/kg air, shaded) and moisture transport ((kg H_2O/kg air)(m/s), vectors) at 925hPa for (a) May, (b) June, (c) July, (d) August, (e) September, and (f) October from the fully-forced future simulations.

2.4b Analysis of Sahel precipitation anomalies

Figure 2.7 is similar to Figure 2.3 and shows the terms of the atmospheric moisture budget as anomalies for the future over the Sahel region (8°N – 14°N and 18°W – 18°E; Fig. 2.2a). The model predicts an anomalous monthly precipitation cycle for the end of the twenty-first century for the Sahel (Fig. 2.7a) that is similar to, but weaker than, that of the Guinean Coast region (Fig. 2.3a). Unlike the response along the Guinean Coast region (Fig. 2.3b), there are times when contributions from evaporation and vertically-integrated moisture advection anomalies play a more considerable role for the Sahel (Fig. 2.7b).

The dry conditions of up to 2.5 mm/day during June and July are accompanied by decreases in evaporation (Fig. 2.7b) reaching from 25% to up to 50% of the rainfall deficit and supported by anomalous vertically-integrated meridional moisture advection (Fig. 2.7b) and near-surface and mid-level zonal moisture divergence (Figs. 2.7a and c). A profile of the zonal wind averaged from 8°N – 14°N along the western edge of the Sahel region at 18°W from the control simulation (Fig. 2.8a) shows the WAWJ from the surface to 875 hPa, as well as the AEJ centered near 650 hPa. The same for the future, and the difference, are shown in Figs. 2.8b and c. A weaker WAWJ and an AEJ that is stronger below the core (Fig. 2.8b-c) support anomalous zonal moisture divergence in the future simulation during June and July. This relationship among a strong AEJ, weak WAWJ, and drying is similar to observed present day variability. The drying in June and July is opposed by anomalous low-level meridional moisture convergence (Fig. 2.7a, d) as well as vertically-integrated zonal moisture advection (Fig. 2.7b).

During August through mid-October wetter conditions of up to 2.5 mm/day are predicted for the Sahel region (Fig. 2.7a), supported by increased evaporation reaching from 33% to 50% of the rainfall anomaly and, in late-August, meridional moisture

advection (Fig. 2.7b). Anomalous low-level zonal moisture convergence (Figs. 2.7a and c) contributes in August and weakly in September, and is related to a stronger WAWJ that is slightly deeper (Figs. 2.8a-c), especially north of 12°N (Figs. 2.5d-e and 2.6d-e). South of 12°N, changes in the jet are weaker (Figs. 2.5c-d) but higher atmospheric moisture is carried by the jet (Figs. 2.6c-d), contributing to the anomalous zonal moisture convergence. Anomalous meridional moisture convergence contributes up to 2mm/day (Fig. 2.7a), primarily at low-levels (Fig. 2.7d), and is supported by stronger low-level northerly flow near the northern edge of the Sahel region box as shown in Figs. 2.8d-f, which display the meridional wind at 16°N averaged from 18°W – 18°E for the control simulation, the ensemble average of the future simulations, and the difference, respectively. The strengthened low-level northerly flow in September and October originates from the Mediterranean region (Figs. 2.5e-f) and supports the connection between Mediterranean SSTAs and Sahel rainfall anomalies discussed in the Section 2.4d. The simulated wetter Sahel, stronger WAWJ, and enhanced moisture transport from the Mediterranean (Figs. 2.6e-f) are also consistent with patterns observed in present day climate variability (Rowell 2003).

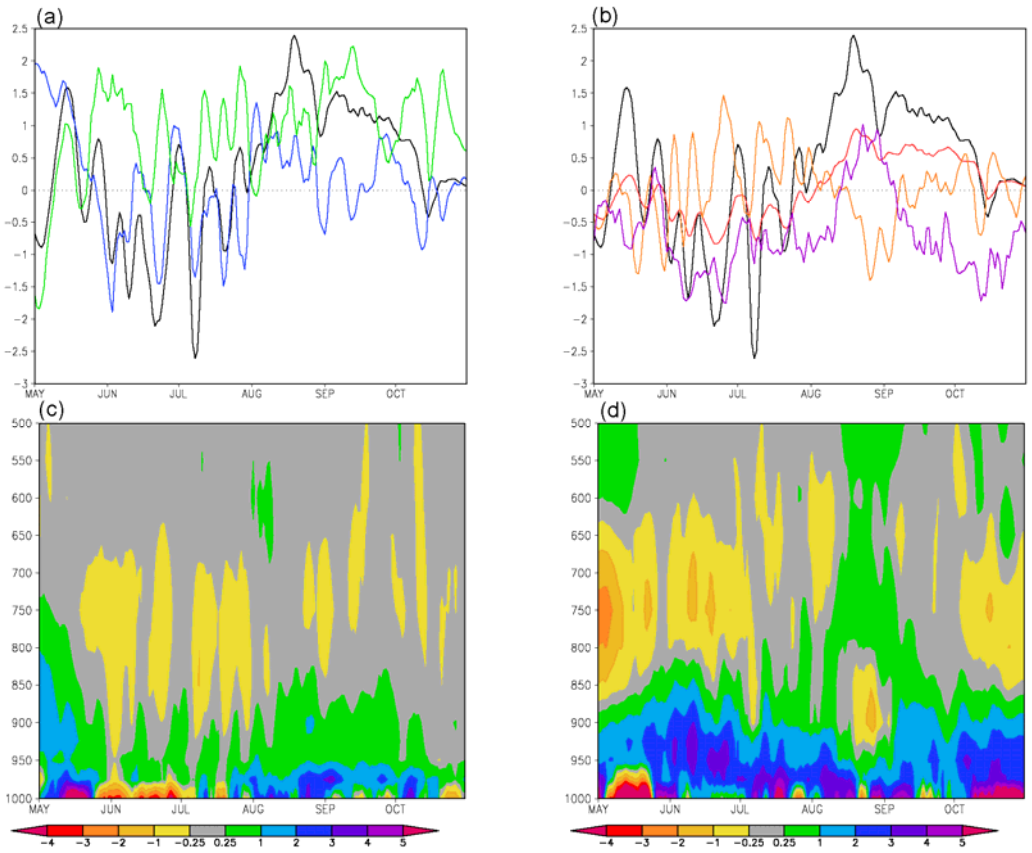

Figure 2.7: Same as Fig. 2.3, but for the Sahel region.

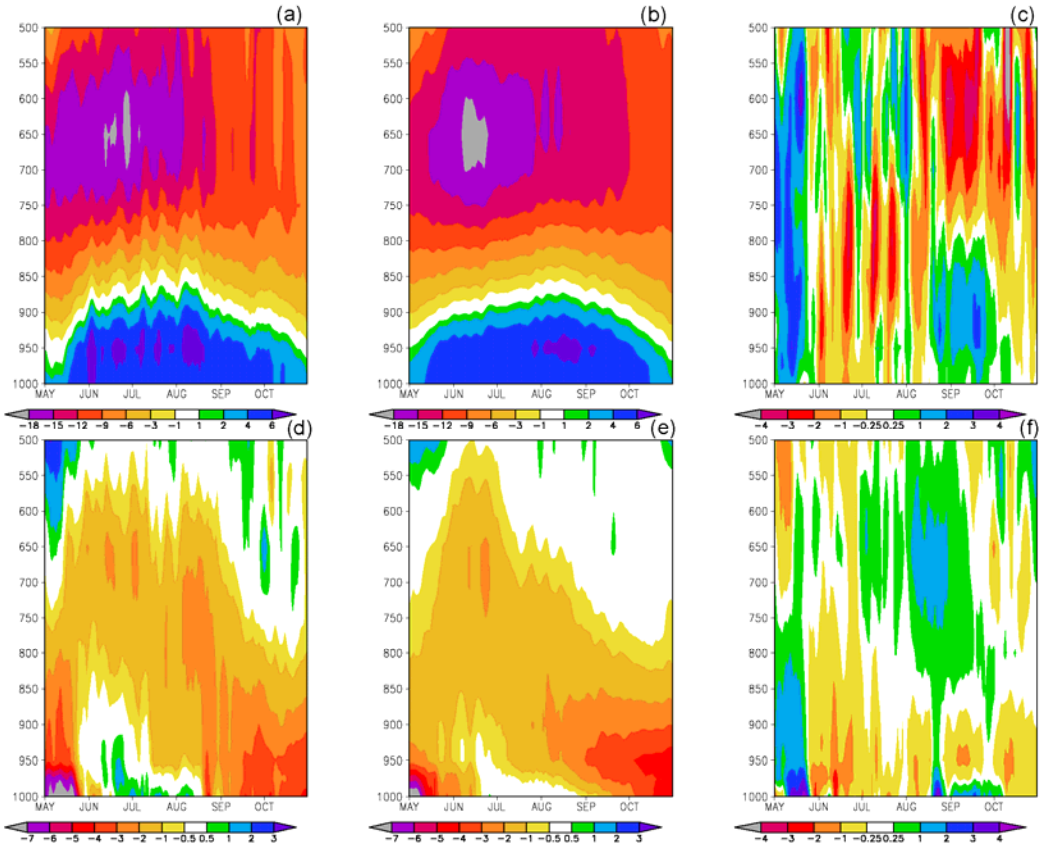

Figure 2.8: The 5-day running mean of the zonal wind profiles at 18°W, averaged over 8°N-14°N for the (a) control simulation, (b) ensemble average of the fully-forced future simulations, and (c) difference. The 5-day running mean of the meridional wind profiles at 16°N, averaged over 18°W-18°E for the (d) control simulation, (e) ensemble average of the fully-forced future simulations, and (f) difference. Units are m/s.

2.4c Analysis of East African precipitation anomalies

Precipitation predictions for the end of the twenty-first century over the region in East Africa (2°S-10°N and 28°E-36°E; Fig. 2.2a) covering parts of Uganda and Kenya are relatively weak except for a severe dry period peaking at a deficit of 10 mm/day in August and September (Fig. 2.9a). The decline in rainfall is triggered by anomalous meridional moisture divergence (Fig. 2.9a) and the drier conditions are sustained by anomalous zonal moisture divergence (Fig. 2.9a) and decreased evaporation of up to -3.75 mm/day (Fig. 2.9b). Changes in the advection terms are insignificant (Fig. 2.9b).

The development of the late summer drought is associated with changes in the Somali jet, Turkana jet, and Indian monsoon. Figure 2.10 shows geopotential height and wind vectors at 900 hPa averaged over August and September for the control simulation, the ensemble average of the fully-forced future simulations, and the difference. The Somali jet, which is characterized by low-level southerly flow over the Horn of Africa that turns westerly over the Arabian Sea, is represented well in the control simulation. During August and September in the future, the Somali jet is much weaker with stronger flow diverting into the Turkana jet, similar to the modeled relationship in Vizy and Cook (2003). The dry conditions and strengthened Turkana jet are also similar to the present day relationship simulated by Sun et al. (1999). The weakened Indian monsoon, which is simulated adequately by the regional model, and dry conditions in East Africa are also similar to observed present-day relationships (Camberlin 1997). The simulated climate changes that are consistent with present day climate variability and the reasonable regional model simulation of the control summer Indian rainfall both lend support to the confidence in the rainfall predictions over East Africa.

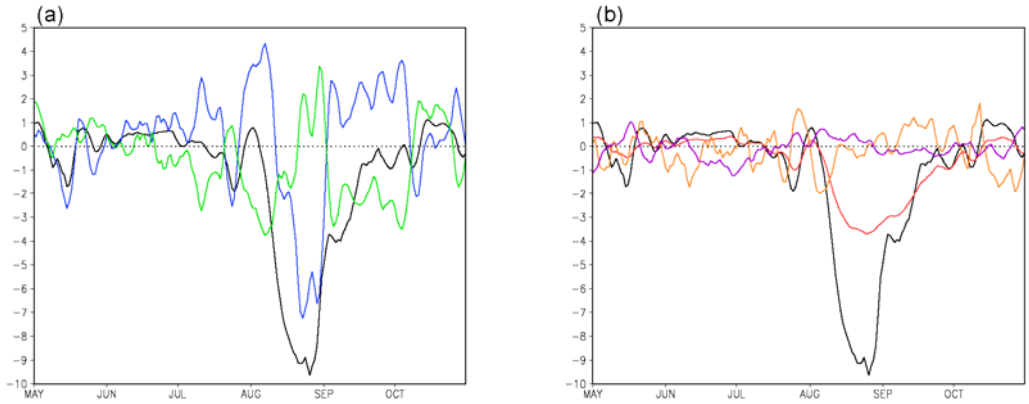

Figure 2.9: Same as Figure 2.3a-b, but for the East African region.

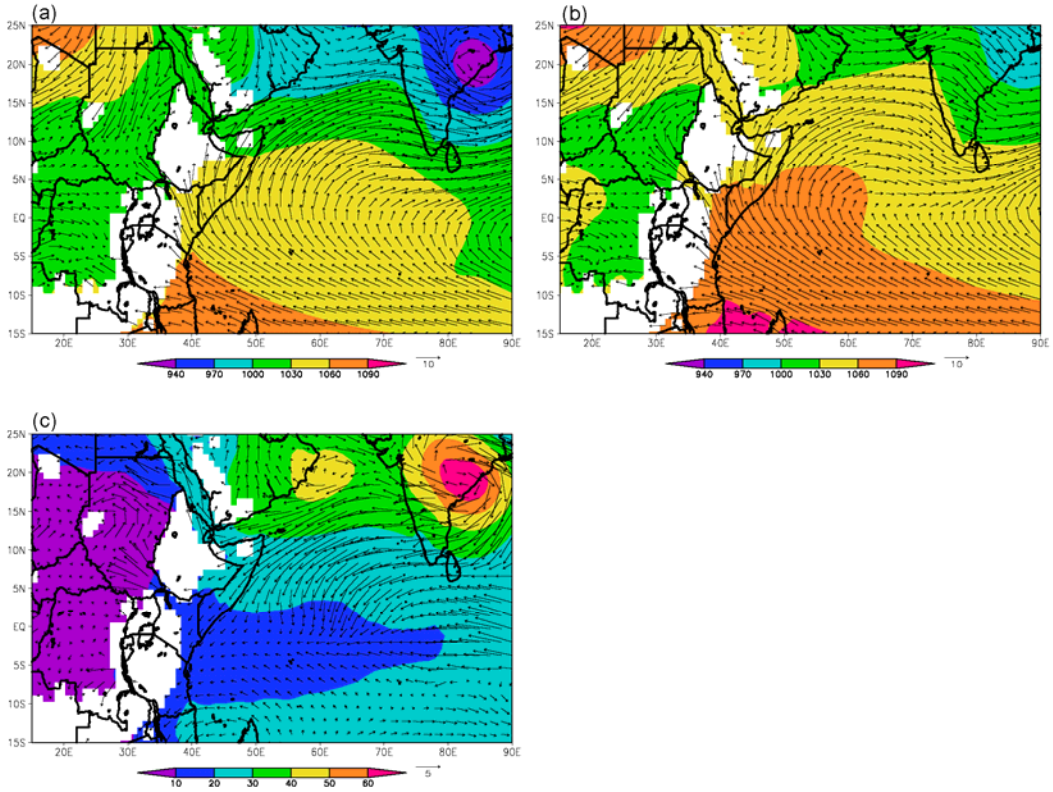

Figure 2.10: Geopotential heights (m, shaded) and wind (m/s, vectors) at 900hPa during August and September from the (a) control simulation, (b) ensemble average of the fully-forced future simulations, and (c) difference.

2.4d Individual climate forcings

The role of individual climate forcings, including atmospheric CO_2 concentration and SST and LBC anomalies, is investigated. The purpose is to add confidence to the projections presented in PC09 by improving our understanding of the important climate change processes.

In order to isolate the role of SSTAs and LBCAs, we compare the monthly precipitation anomalies due to SSTA, LBCA and CO_2 forcing (Figs. 2.11a-c) with those due to only SSTA and LBCA forcing (Figs. 2.11d-f). For both simulations, SSTA and LBCA forcings are provided by the ECHAM AOGCM. The distributions of the precipitation anomalies forced by SSTAs and LBCAs are very similar with and without regional CO_2 forcing from May through October (May, September, and October not shown). For example, drying is produced in the Gulf of Guinea and central Africa is wetter in June, central Africa and the Guinean Coast are drier in July, and the Sahel (East Africa) is wetter (drier) in August both with (Figs. 2.11a-c, respectively) and without (Figs. 2.11d-f, respectively) the regional CO_2 forcing. This agreement indicates that the fully-forced twenty-first century rainfall anomalies (Fig. 2.1 and PC09) are primarily caused by SST and lateral boundary forcing that are consequences of the global CO_2 forcing, and not the regional CO_2 forcing applied within the RCM domain.

However, regional CO_2 forcing does play an important role in some regions. The full forcing produces precipitation anomalies that are near zero or weakly negative over the Sahel region in June (Fig. 2.11a), while the SSTA and LBCA forcing results in strong drying over the Sahel (Fig. 2.11d). In July and August, Sahelian precipitation anomalies are strongly positive (weakly positive) due to SSTA and LBCA forcing with (Figs. 2.11b and c) (without; Figs. 2.11e and f) regional CO_2 forcing. While the spatial distribution of the fully-forced future precipitation

anomalies is dominated by the SSTAs and LBCAs, regional CO_2 forcing significantly impacts the magnitude of the rainfall anomalies, especially in the Sahel region, and generally produces more positive rainfall anomalies.

Figure 2.12 shows monthly precipitation anomalies due to increasing the CO_2 concentration over the regional model domain from 330 ppm to 757 ppm. Wetter conditions over the Sahel from May through September, with little change in October, are produced by these regional CO_2 increases. The wet conditions are concentrated over the western Sahel in May and June (Figs. 2.12a-b), but extend across the continent in July, August, and September (Figs. 2.12c-e). Over the Guinean Coast region, regional CO_2 forcing produces wetter conditions throughout the summer except for a dry period in July and August. In East Africa, regional CO_2 forcing produces wetter conditions over western Ethiopia from May through September except for a small region of drying in June. In October conditions are wet (dry) over southern (northern) Ethiopia. The rainfall signal is weak over central Africa except in August when anomalies are positive (negative) over the Congo region (Uganda and southern Sudan) and in October when conditions are wetter.

The evolution of the land-surface warming over northern Africa from May through October due to regional CO_2 forcing provides further insight to the Sahelian and Guinean Coast precipitation anomalies. Figure 2.13 shows monthly anomalies in skin temperature and moisture transport at 950 hPa due to regional CO_2 forcing. Warming is centered over the Sahara and peaks in July (Fig. 2.13c), while cooling related to increased rainfall occurs south of 15°N and peaks in August. In association with the Saharan warming, the low-level thermal low over northern Africa is intensified (not shown), and the anomalous cyclonic circulation carries moisture deeper into the continent. In May and June (Figs. 2.13a-b) this intensification is relatively weak, and so the additional moisture reaches only the Guinean Coast region

and supports wetter conditions there. By July and August (Figs. 2.13c-d) the intensification of the thermal low peaks in association with the maximum Sahelian surface temperature anomalies, and the anomalous circulation transports moisture much deeper into the continent, supporting the wetter conditions over the Sahel instead of the Guinean Coast region where higher pressure has developed. Although the Sahel is wetter in August due to both regional CO_2 forcing alone and the full future forcings, distinctly different physical processes are working in each case, both of which have analogies in present day observed variability.

During July and August, the peak of the wetter conditions over western Ethiopia in East Africa, the anomalous southwesterly winds on the southeastern side of the thermal low flow into the topography of the Ethiopian Highlands supporting increased orographic rainfall. At the same time the Somali jet is stronger and the Turkana jet is weaker, similar to the modeled relationship in Vizy and Cook (2003).

The nine fully-forced regional model ensemble members produce precipitation predictions (Fig. 2.1) that are consistent over much of northern Africa. This ensemble agreement is despite the differences among the anomalous SST and LBC forcings prescribed from the nine AOGCMs. The similarities among the ensemble members suggest that the simulated future climate is not sensitive to the details of the SSTA and LBCA constraints, rather that the similarities in predicted rainfall may be related to the overall warming of the atmosphere and ocean. To test this hypothesis, we compare the monthly precipitation anomalies forced by the nine SSTA distributions taken from the AOGCMs (Fig. 2.14) to those due to a uniform 2K warming of the ocean (Fig. 2.15).

During May and June, rainfall anomalies forced by the AOGCM SSTAs (Figs. 2.14a-b) and uniform 2K SSTAs (Figs. 2.15a-b) are similar east of 10°E, with drying over the Sahel and central Africa and wetter conditions over East Africa, suggesting

that the overall ocean warming dominates the changes in SST gradients for this region. In contrast, AOGCM SSTA forcing produces drier conditions over West Africa, while anomalies are near zero or weakly positive due to the 2K SSTA, indicating that changes in SST gradients play an important role in May and June.

The impact of SST warming dominates changes in SST gradients everywhere, even over West Africa, in July through September when the simulated rainfall anomalies under uniform 2K SST warming (Figs. 2.15c-e) are very similar to those from the AOGCM SSTAs (Figs. 2.14c-e). In July the east-west dipole, with dry (wet) conditions in western (eastern) Africa, is strikingly similar between the SSTA_only and 2K_SSTA simulations. During August and September both the predicted SSTAs and uniform 2K SST warming generate wetter conditions, with similarly-placed maxima over Ethiopia and Kenya, central Sudan, and Nigeria, Togo, and Benin.

Rainfall anomalies are similar during October east of 10°E, but they are different in West Africa where the AOGCM SSTAs produce an inconsistent or weakly positive signal and the 2K SST warming produces weakly dry conditions. With the exception of West Africa during May, June, and October, the precipitation anomalies due to SSTAs from the 9 AOGCMs (Figs. 2.14a, b, f) are similar to those due to uniform 2K SST warming (Figs. 2.15a, b, f), supporting the idea that for some regions of northern Africa the overall warming of the oceans dominates the response. This may partly explain the high level of consistency among the ensemble members in the fully-forced regional simulations.

To better understand the SSTA-forcing of precipitation anomalies for the end of the twenty-first century, correlations between area-averaged SSTAs over specific ocean regions and daily rainfall anomalies are calculated for each of the nine fully-forced future ensemble members. Figure 2.16a shows the ocean averaging regions, including the Mediterranean (5°W-30°E and 30°N-42°N), northern Atlantic (53°W-

5°W and 10°N-47°N), equatorial Atlantic (53°W-20°E and 10°S-10°N), southern Atlantic (53°W-20°E and 32°S-10°S), northern Indian (45°E-103°E and 10°N-20°N), equatorial Indian (45°E-103°E and 10°S-10°N), and southern Indian (45°E-103°E and 32°S-10°S) basins. The ensemble-averaged correlations are shown in Figs. 2.16b-d and 2.17. Regions where the correlation is not significant at the 95% confidence level (two-sided test) are shaded white, and regions where less than 7 of the 9 ensemble members agree on the sign of the correlation are shaded grey. Correlations are also calculated between SSTAs over the entire domain and rainfall anomalies over the land regions defined in Fig. 2.2a (Figure 2.18).

Ensemble members do not agree about the sign of the correlation of northern Africa rainfall with SSTAs over the northern Indian basin (Fig. 2.16b), but correlations over both the equatorial (Fig. 2.16c) and southern (Fig. 2.16d) Indian basins are significant. Sahelian precipitation is negatively correlated with SSTAs in both the equatorial and southern Indian Ocean regions, while precipitation over East Africa is positively correlated with SSTAs from only the southern Indian basin, most strongly around Madagascar (Fig. 2.18c). The negative correlation between Indian Ocean SSTAs and precipitation anomalies over the Sahel is consistent with our understanding of present day decadal-scale climate variability (Giannini et al. 2003; Bader and Latif 2003; Lu and Delworth 2005; Chung and Ramanathan 2006; Hagos and Cook 2008).

The RCM simulates significant positive correlations between northern Atlantic Ocean SSTAs and precipitation over the Sahel region, while northern Atlantic SSTAs are negatively correlated with rainfall anomalies over a small region along the Guinean Coast (Fig. 2.17a). Sahel rainfall anomalies are related to SSTAs over all of the northern tropical and subtropical Atlantic (Fig. 2.18b), while Guinean Coast rainfall anomalies are related to SSTAs over only the subtropical Atlantic (Fig. 2.18a).

The regional model also produces a significant negative correlation between northern tropical and subtropical Atlantic SSTAs and precipitation over Eastern Africa (Figs. 2.17a and 2.18c).

There is little agreement among the ensemble members in the correlation of precipitation and SSTAs in the equatorial Atlantic (Fig. 2.17b) except for a positive correlation between Guinean Coast rainfall anomalies and Atlantic SSTAs between the equator and 5°N (Fig. 2.18a). Correlations with SSTAs in the southern Atlantic, specifically in the subtropics (Fig. 2.18a), are confined to the Guinean Coast region where the relationship is positive (Fig. 2.17c). The simulated relationship between northern and southern Atlantic SSTs and West African rainfall is consistent with our understanding of present day climate variability (Lamb 1978a and 1978b; Folland et al. 1986; Druyan 1991; Folland et al. 1991; Lamb and Peppler 1992; Ward 1998; Vizy and Cook 2002) and emphasizes the importance of changes in SST gradients in simulating future West African rainfall in May, June, and October (Figs. 2.14a,b,f and 2.15a,b,f).

The relationship between SSTAs in the Mediterranean region and precipitation anomalies produced by the full future forcings (Fig. 2.17d) is similar to that of the northern Atlantic. The association between wetter conditions in the Sahel and drier conditions in the Guinean Coast region with warmer SSTAs in the Mediterranean simulated in the regional model is similar to the relationship found by Rowell (2003) and, as discussed in Section 2.4b, the associated moisture transport anomalies that are observed with Mediterranean warming in the present day are relevant for future climate. The RCM also simulates a negative correlation between Mediterranean SSTs and rainfall over Uganda and southern Sudan.

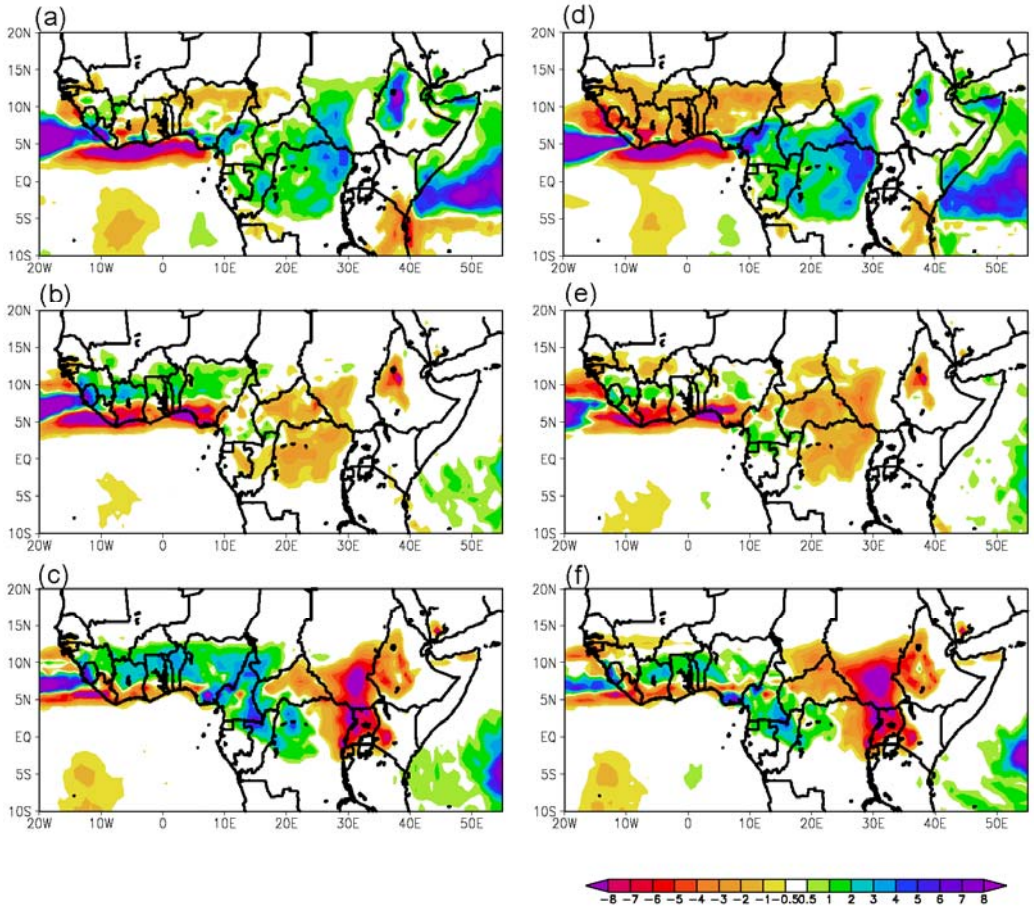

Figure 2.11: Precipitation anomalies from the fully-forced future simulation constrained with the ECHAM AOGCM for (a) June, (b) July, and (c) August, and from SSTA+LBCA_EC simulation the for (d) June, (e) July, and (f) August. Units are mm/day.

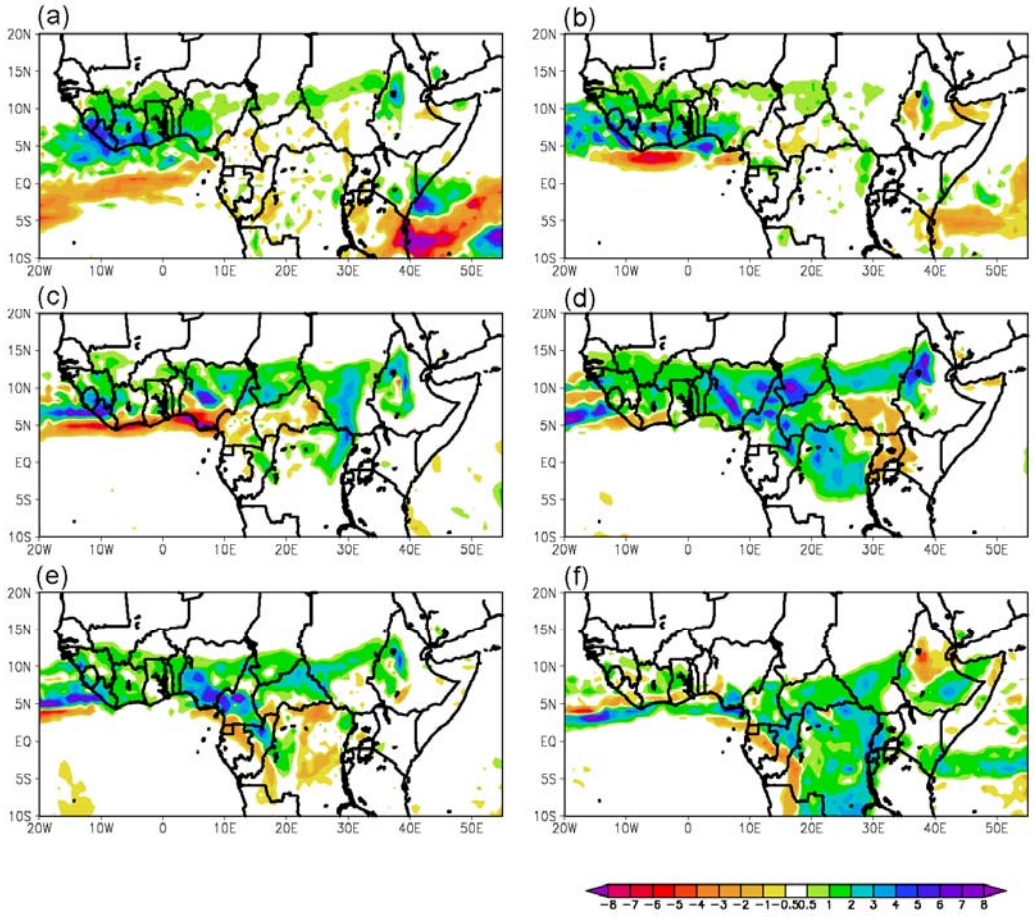

Figure 2.12: Precipitation anomalies from the CO_2_only simulation for (a) May, (b) June, (c) July, (d) August, (e) September, and (f) October. Units are mm/day.

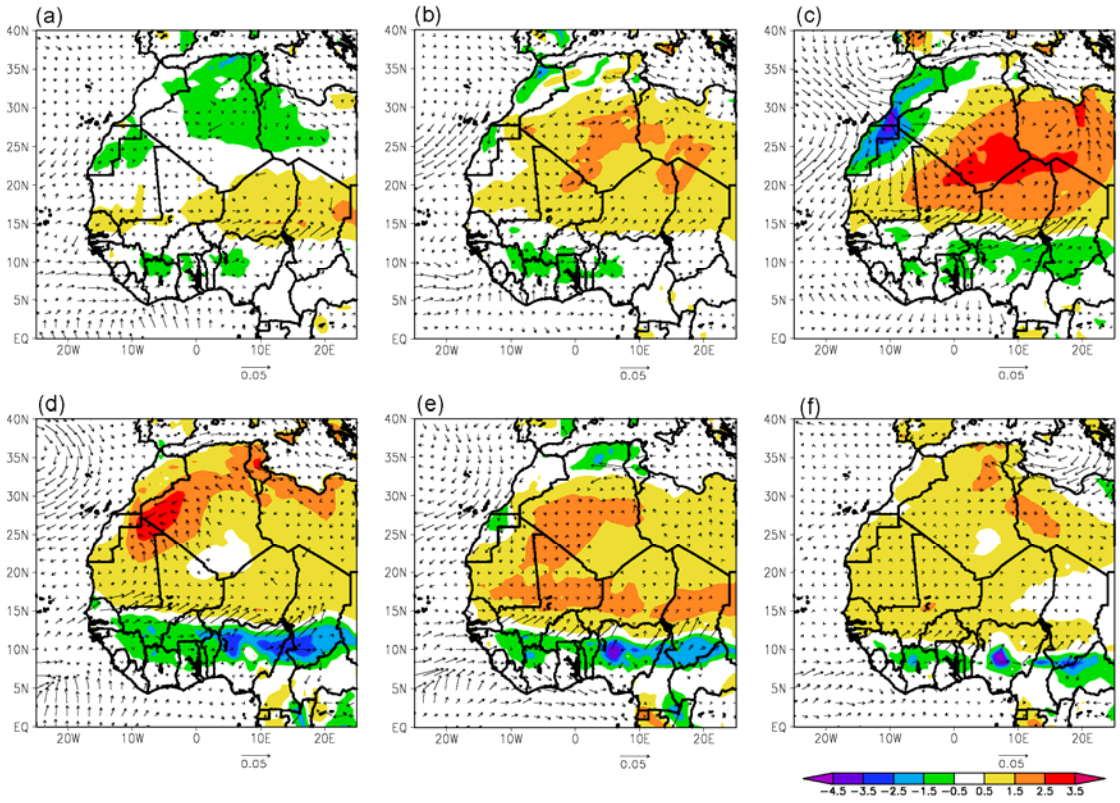

Figure 2.13: Anomalies in skin temperature (shaded, K) and moisture transport at 950hPa ((kg H_2O/kg air)(m/s), vectors) for (a) May, (b) June, (c) July, (d) August, (e) September, and (f) October from the CO_2_only simulation.

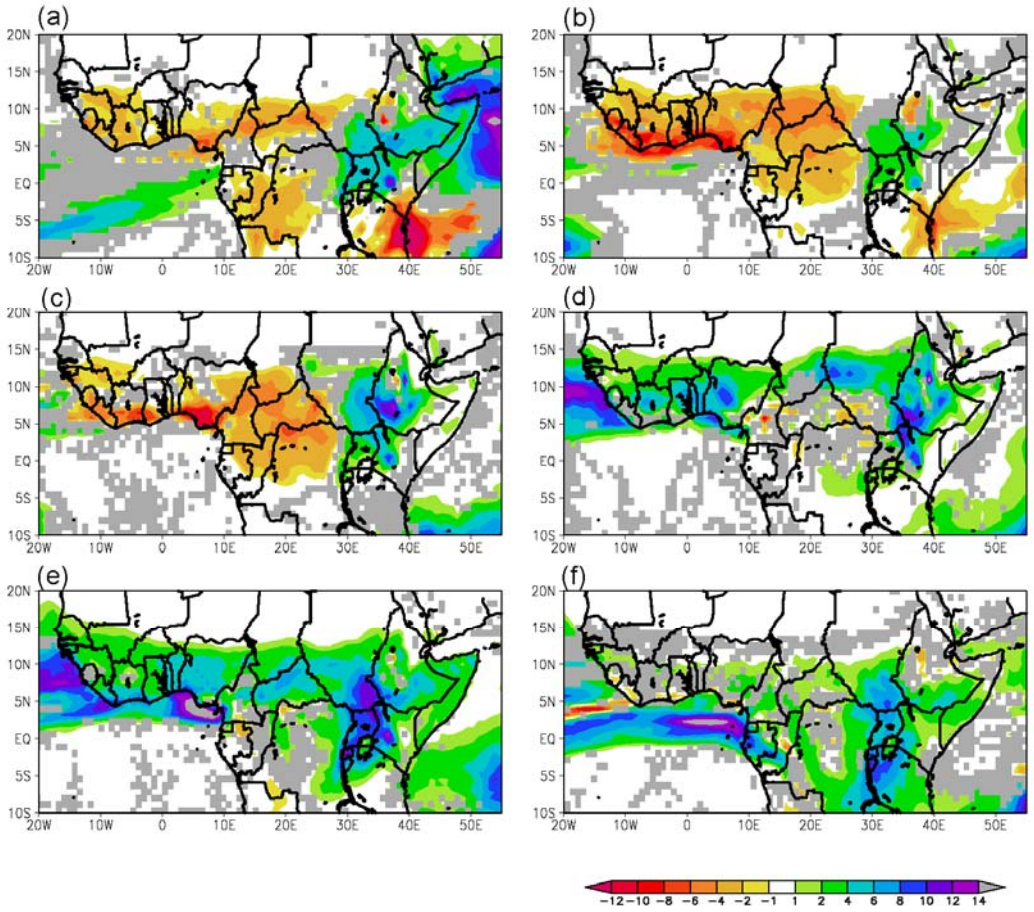

Figure 2.14: Ensemble averaged precipitation anomalies from the SSTA_only simulations for (a) May, (b) June, (c) July, (d) August, (e) September, and (f) October. Units are mm/day. Areas where less than 77% of the ensemble members agree are shaded grey.

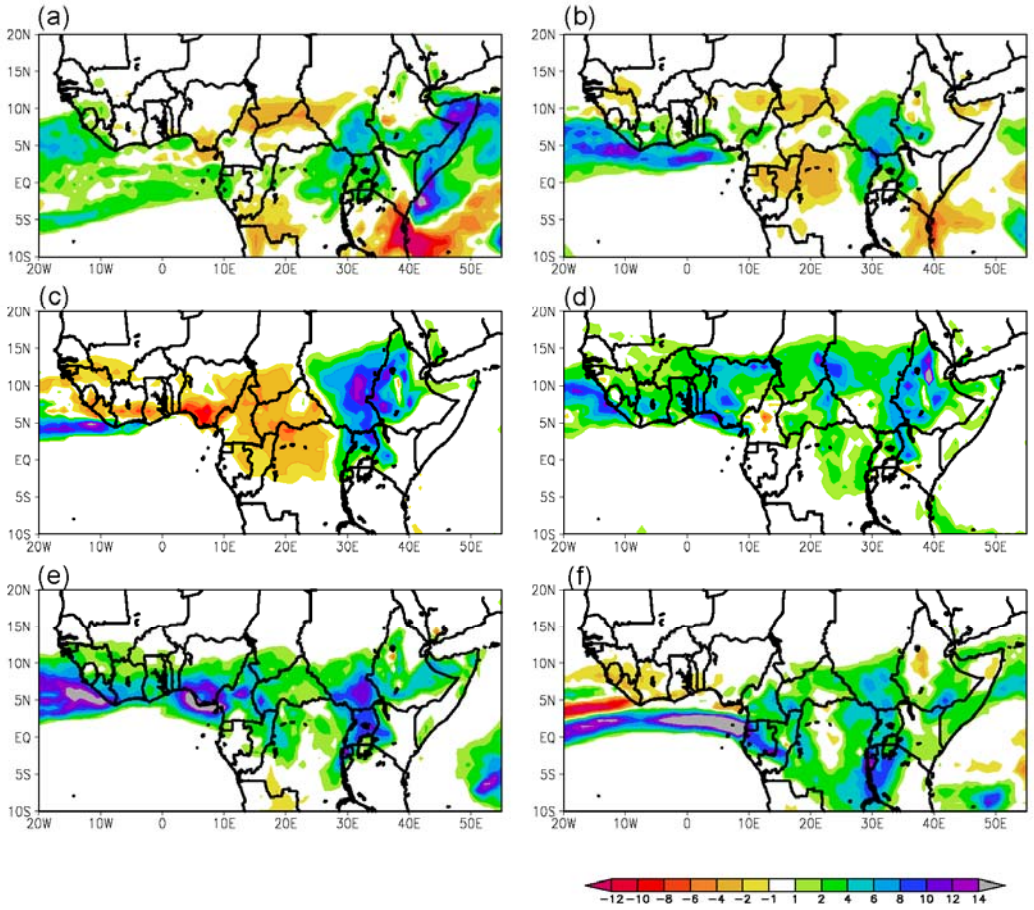

Figure 2.15: Precipitation anomalies from the 2K_SSTA simulation for (a) May, (b) June, (c) July, (d) August, (e) September, and (f) October. Units are mm/day. Areas where less than 77% of the ensemble members agree are shaded grey.

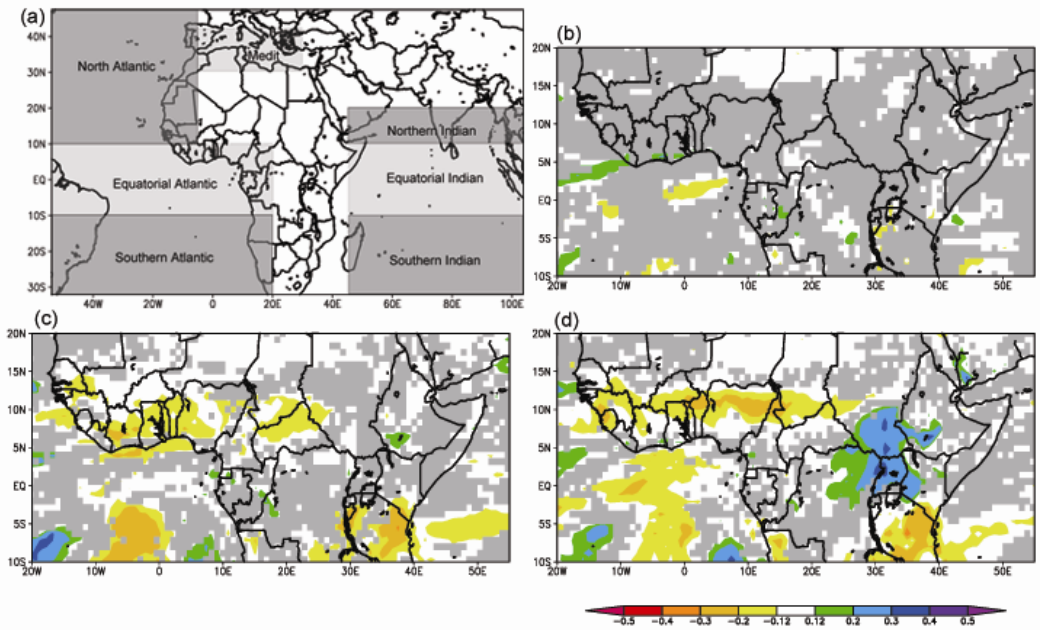

Figure 2.16: (a) Ocean regions for correlations between SSTA and precipitation anomalies. Ensemble averaged correlation coefficients for daily precipitation anomalies and SSTAs from the fully-forced future simulations over the (b) north Indian, (c) equatorial Indian, and (d) south Indian regions including May 1 – October 31. White regions are insignificant at the 5% level (two sided test), and areas where less than 77% of the ensemble members agree are shaded grey.

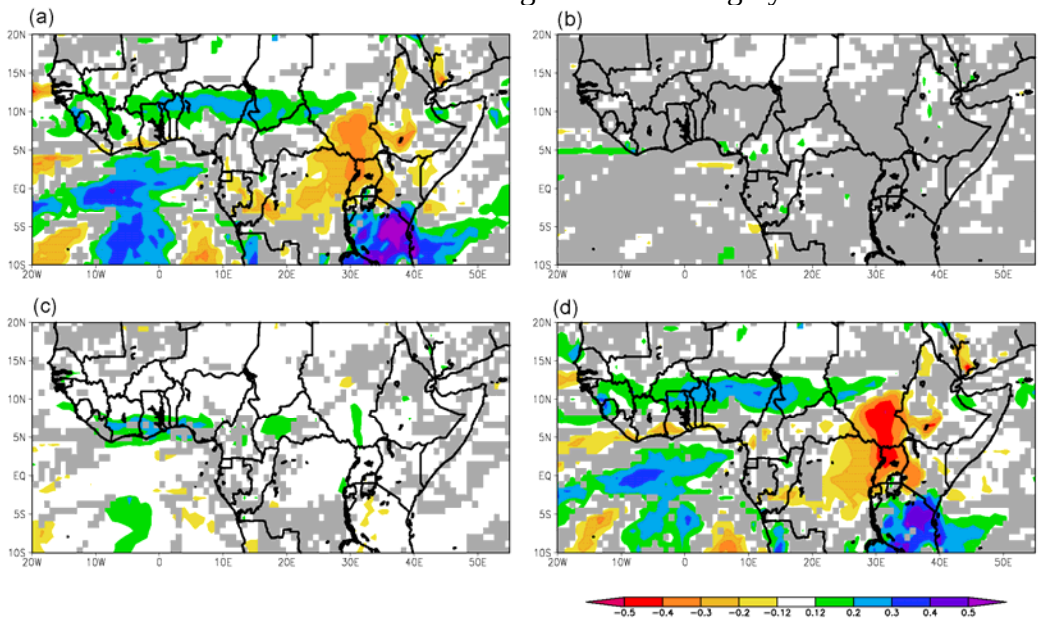

Figure 2.17: Ensemble averaged correlation coefficients for daily precipitation anomalies and SSTAs from the fully-forced future simulations over the (a) north Atlantic, (b) equatorial Atlantic, (c) south Atlantic, and (d) Mediterranean regions including May 1 – October 31. White regions are insignificant at the 5% level (two sided test), and areas where less than 77% of the ensemble members agree are shaded grey.

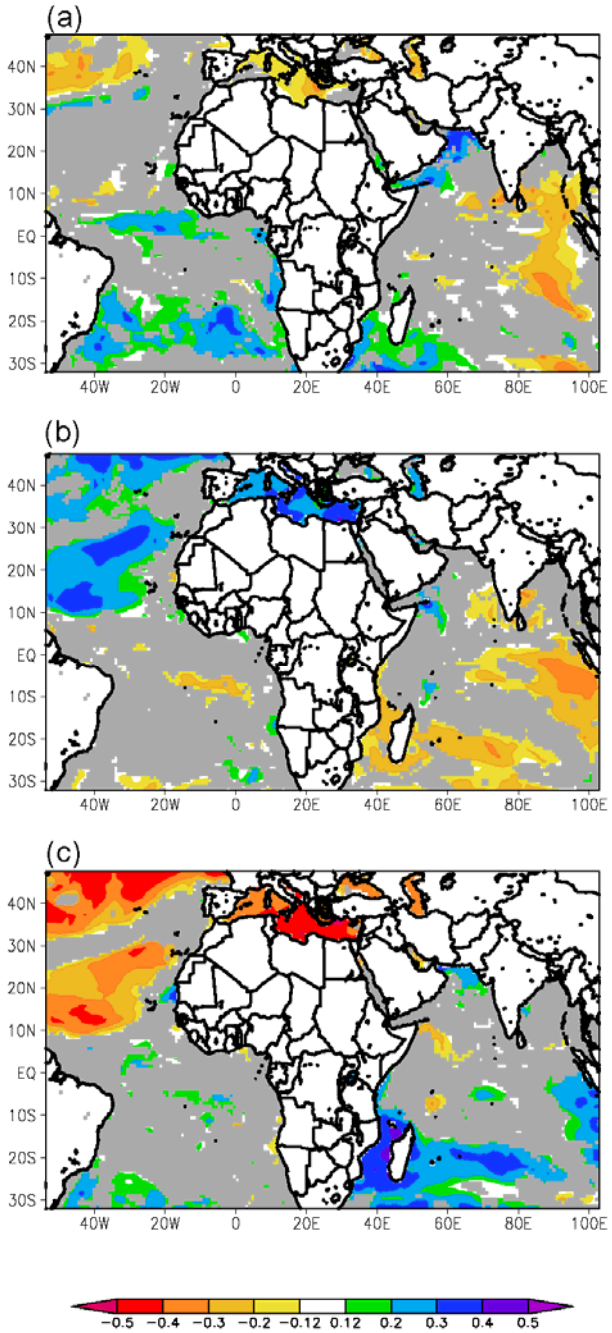

Figure 2.18: Ensemble averaged correlation coefficients for SSTAs and daily precipitation anomalies from the fully-forced future simulations over the (a) Guinean Coast, (b) Sahel, and (c) East African regions including May 1 – October 31. Only regions over land are included in the averaging. White regions are insignificant at the 5% level (two sided test), and areas where less than 77% of the ensemble members agree are shaded grey.

2.5 Conclusions

Patricola and Cook (2009) develop a method for simulating future northern African climate that combines the strengths of regional and global modeling. An ensemble set of nine simulations representative of climate at 2081 – 2100 are performed with a regional climate model forced with increased atmospheric CO_2 and anomalous SSTs and lateral boundary conditions derived from nine different AOGCMs. The high level of agreement among the ensemble members and the reasonable representation of the present day climate supports confidence in the climate predictions.

Here, we further evaluate, and enhance confidence in these climate predictions by developing a physical understanding of the response. A sensitivity test confirms that the initialization of soil moisture and temperature in the regional simulations are not influential in the response.

For the Guinean coast region, where wet conditions develop in May and mid-August through October with drying in June through mid-August, a moisture budget analysis shows that the rainfall anomalies are primarily supported by anomalies in both zonal and meridional moisture convergence. Drying in June through mid-August is related to a weaker and shallower southerly monsoon flow, while the wetter conditions in May and mid-August through October are associated with both a strengthening of the low-level westerly flow and positive atmospheric moisture anomalies, as well as a monsoon flow that is stronger near the surface with a weaker return flow.

Rainfall anomalies over the Sahel include drying in June and July, and wetter conditions in August, September, and October. Anomalies in vertically-integrated moisture convergence, as well as evaporation and vertically-integrated moisture advection, contribute significantly to the precipitation anomalies. A weaker West

African westerly jet (WAWJ) and stronger African easterly jet support the summer drying. Wetter conditions in late summer and fall are sustained by positive atmospheric moisture anomalies carried by the WAWJ, as well as a strengthening of the jet itself, and anomalous moist flow from the Mediterranean region that is likely linked with SSTAs.

Over the Uganda/Kenya/southern Sudan region in East Africa, severe drying in August and September is related to a weakening of the Somali jet and Indian monsoon and a strengthening of the Turkana jet and is partially supported by decreased evaporation. This relationship between East African and Indian rainfall is observed in present day climate variability and, given the strong relationship between these two regions, one should take note that a successful East African prediction depends on a realistic control simulation over India. The authors note that the RCM produces a reasonable simulation of over India, however a rigorous validation comparable to that completed for Africa by PC09 was not completed.

Simulations which isolate the roles of the regional CO_2 forcing and anomalous SST and lateral boundary constraints confirm that the spatial distribution of the rainfall predictions is primarily dominated by the SST and lateral boundary constraints. Over the Sahel, however, regional CO_2 forcing plays an important secondary role. The seasonal evolution of the Saharan warming due to regional CO_2 increases results in a peak intensification of the thermal low in July, with wind anomalies that carry moisture deeper into the Sahel from the south. Although the precipitation responses are similar in August, the physical mechanism due to increased regional CO_2 is different than that produced by the full future forcings.

The similarities in rainfall anomalies between simulations constrained with only SSTAs from nine AOGCMs and a simulation with a uniform SST warming of 2K suggest that the overall warming of the ocean may be in part controlling the consensus

among the ensemble members of the fully-forced future simulations over most regions. However, over West Africa in May, June, and October, changes in SST gradients play a more significant role.

The regional model simulations capture several of the observed relationships between rainfall and SST anomalies. These include a positive (negative) correlation between Sahelian rainfall and both Mediterranean and northern Atlantic (equatorial and southern Indian) SSTs, as well as a negative (positive) correlation between Guinean Coast rainfall and northern (southern) Atlantic SSTs. The presence of these relationships in the future simulations helps to better explain the predicted rainfall changes and, along with agreement among ensemble members, supports confidence in the predictions.

On seasonal timescales, the Sahelian rainfall predictions from the regional model are similar to those from the most recent AOGCM projections. This study emphasizes the need for regional climate predictions on at least monthly timescales that rely not only on ensemble agreement and model validation, but also on our physical understanding of the predicted climate changes.

REFERENCES

Bader J, Latif M (2003) The impact of decadal-scale Indian Ocean sea surface temperature anomalies on Sahelian rain- fall and the North Atlantic Oscillation. Geophys Res Lett, 30: 2169, DOI:10.1029/2003GL018426.

Chung CE, Ramanathan V (2006) Weakening of North Indian SST gradients and the monsoon rainfall in India and the Sahel. J Clim, 19(10): 2036-2045.

Cook KH (1997) Large-scale atmospheric dynamics and Sahelian precipitation. J Clim, 10(6): 1137-1152.

Cook KH (1999) Generation of the African easterly jet and its role in determining West African precipitation. J Clim, 12(5): 1165-1184.

Cook KH (2008) Climate Science: The mysteries of Sahel droughts. Nature Geoscience, 1(10): 647-648.

Cook KH, Vizy EK (2006) Coupled model simulations of the West African monsoon system: 20th Century simulations and 21st Century predictions. J Clim: 19, 3681-3703.

Druyan LM (1991) The sensitivity of sub-Saharan precipitation to Atlantic SST. Climatic Change, 18: 17-36.

European Centre for Medium-Range Weather Forecasts (2002) The ERA-40 Archive. Reading, ECMWF: 40.

Findlater J (1966) Cross-equatorial jet streams at low-levels over Kenya. Meteor Mag, 95: 353-364.

Findlater J (1977) Observational aspects of the low-level cross-equatorial jet stream of the western Indian Ocean. Pure Appl Geophys, 115: 1251-1262.

Folland CK, et al. (1986) Sahel rainfall and worldwide sea temperatures, 1901– 85. Nature, 320: 602– 607.

Folland CK, et al. (1991) Prediction of seasonal rainfall in the Sahel region using empirical and dynamic methods. J Forecasting, 10(1-2): 21-56.

Fontaine B, et al. (1995) Rainfall anomaly patterns and wind field signals over West Africa in August (1958 – 1989). J Clim, 8: 1503–1510.

Giannini A, Saravanan R, Chang P (2003) Oceanic forcing of Sahel rainfall on interannual to interdecadal time scales. Science, 302(5647): 1027-1030.

Giannini A, Biasutti M, Held IM, Sobel, AH (2008) A global perspective on African climate. Clim Change, 90: 359-383.

Grist JP, Nicholson SE (2001) A study of the dynamic factors influencing the rainfall variability in the West African Sahel. J Clim, 14: 1337-1359.

Grodsky SA, Carton JA, Nigam S (2003) Near surface westerly wind jet in the Atlantic ITCZ. Geophys Res Lett, 30(19): DOI: 10.1029/2003GL017867.

Hagos SM, Cook KH (2008) Ocean warming and late-twentieth-century Sahel drought and recovery. J Clim, 21(15): 3797-3814.

Held IM, Delworth TL, Lu J, Findell KL, Knutson TR (2005) Simulation of Sahel drought in the 20th and 21st centuries. Proc National Academy of Sci, 102(50): 17891-17896.

IPCC (2007) Climate Change 2007: Impacts, Adaptation and Vulnerability. Contribution of Working Group II to the Fourth Assessment Report of the Intergovernmental Panel on Climate Change, M.L. Parry, O.F. Canziani, J.P. Palutikof, P.J. van der Linden and C.E. Hanson, Eds., Cambridge University Press, Cambridge, UK: 976pp.

IPCC (2000) Emissions Scenarios, N. Nakicenovic and R. Swart, Eds., Cambridge Univeristy Press, Cambridge, UK: 570pp.

Janicot S (1992) Spatiotemporal variability of West African rainfall. Part II: Associated surface and airmass characteristics. J Clim, 5(5): 499-511.

Kalnay E et al (1996) The NCEP/NCAR 40-Year Reanalysis Project. Bull Am Meteorol Soc 77:437–471.

Kinuthia JH, Asnani GC (1982) A newly found jet in North Kenya (Turkana Channel). Mon Weather Rev, 110: 1722–1728.

Kinuthia JH (1992) Horizonatal and vertical structure of the Lake Turkana Jet. J Appl Meteor, 31: 1248-1274.

Koster RD, et al. (2004) Regions of strong coupling between soil moisture and precipitation. Science, 305 (5687): 1138 – 1140.

Lamb PJ (1978a) Case studies of Tropical Atlantic surface circulation patterns during recent Sub-Saharan weather anomalies: 1967 and 1968. Mon Weather Rev, 106: 482-491.

Lamb PJ (1978b) Large-scale tropical Atlantic surface circulation patterns associated with sub-Saharan weather anomalies. Tellus, 30: 240–251.

Lamb JL, Peppler RA (1992) Further case studies of tropical Atlantic surface atmospheric and oceanic patterns associated with sub-Saharan drought. J Clim, 5:476-488.

Lenters JD, Cook KH (1995) Simulation and diagnosis of the regional summertime precipitation climatology in South America. J Clim 8: 2988-3005.

Lu J, Delworth TL (2005) Oceanic forcing of the late 20th century Sahel drought. Geophys Res Lett, 32: L22706, DOI:10.1029/2005GL023316.

Lu J (2009) The dynamics of the Indian Ocean sea surface temperature forcing of Sahel drought. Clim Dyn, 33: 445-460.

Maynard K, Royer JF (2004) Effects of "realistic" land-cover change on a greenhouse-warmed African climate. Clim Dyn, 22: 343-358.

Newell RE, Kidson JW (1984) African mean wind changes between Sahelian wet and dry periods. J Climatol, 9: 27– 33.

Nicholson SE (1980) The nature of rainfall fluctuations in sub-tropical West-Africa. Mon Weather Rev, 108: 473-487.

Paeth H, Thamm HP (2007) Regional modeling of future African climate north of 15 degrees S including greenhouse warming and land degradation. Clim. Change, 83(3): 401-427.

Patricola CM, Cook KH (2009) Northern African Climate at the end of the 21st Century: Integrated Application of Regional and Global Climate Models. Clim Dyn, DOI 10.1007/s00382-009-0623-7.

Pu BP, Cook KH (2010a) Dynamics of the West African Westerly Jet, in press J Clim.

Pu BP, Cook KH (2010b) The association of the West African westerly jet and Sahel precipitation on the interannual and interdecadal scale, in preparation.

Rowell JP, et al. (1995) Variability of summer rainfall over tropical north Africa (1906-92): Observations and modeling. Q J R Meteorolo Soc, 121: 669-704.

Rowell DP (2003) The Impact of Mediterranean SSTs on the Sahelian Rainfall Season. J Clim, 16: 849-862.

Skamarock WC, Klemp JB, Dudhia J, Gill DO, Barker DM, Wang W, Powers JG (2005) A description of the Advanced Research WRF Version 2. NCAR Tech. Note, ncar/TN-468+STR: 88 pp.

Sultan B, Janicot S (2003) The West African monsoon dynamics. Part II: The “preonset” and “onset” of the summer monsoon. J Clim, 16(21): 3407-3427.

Sun L, Semazzi FHM, Giorgi F, Ogallo L (1999) Application of the NCAR regional climate model to Eastern Africa 2. Simulation of interannual variability of short rains. J Geophys Res, 104(D6): 6549-6562.

Vizy EK, Cook KH (2002) Development and application of a mesoscale climate model for the tropics: Influence of sea surface temperature anomalies on the West African monsoon. J Geophys Res, 107: DOI: 10.1029/2001JD000686.

Vizy EK, Cook KH (2003) Connections between the summer East Africa and Indian rainfall regimes. J Geophys Res, 108(D16): DOI:10.1029/2003JD003452.

Ward MN (1998) Diagnosis and short-lead time prediction of summer rainfall in Tropical North Africa at interannual and multidecadal timescales. J Clim, 11: 3167-3191.

Xue YK, Shukla J (1993) The influence of land-surface properties on Sahel climate .1. Desertification. J Clim, 6(12): 2232-2245.

Xue YK, Shukla J (1996) The influence of land surface properties on Sahel climate .2. Afforestation. J Clim, 9(12): 3260-3275.

CHAPTER 3

PROCESSES AND PREDICTION OF CLIMATE CHANGE IN THE CENTRAL UNITED STATES

3.1 Introduction

There is a critical need for regional scale climate predictions over the central United States to better understand and plan for the impacts of climate change. While the atmosphere-ocean general circulation models (AOGCMs) run for the Fourth Assessment Report of the Intergovernmental Panel on Climate change (IPCC AR4; IPCC 2007) provide useful information for future changes in large-scale circulation and temperature, precipitation projections on a scale appropriate for impacts analysis require the fine horizontal resolution afforded by regional climate models. As computing resources improve, regional climate models are more often used for predicting future climate, especially since dynamic downscaling may offer more trustworthy predictions than global models alone (e.g., Liang et al. 2008).

In this study we conduct regional climate model simulations with a nested domain focusing on the central U.S., for 1981 – 2000 and 2041 – 2060. The methodology used to prescribe SSTs and lateral boundary conditions to the regional model is a distinguishing feature of this study. Unlike the traditional dynamic downscaling approach in which lateral and surface boundary conditions are prescribed to a regional model directly from a global model, here the boundary conditions are prescribed from 6-hourly reanalysis products for the control simulation, and are created by adding linearly interpolated monthly anomalies from AOGCMs to the reanalysis products for the future simulation. A great benefit of the approach used here – constraining the future simulation with anomalies rather than direct AOGCM

output – is that driving the control simulation with reanalysis products produces a realistic representation of the present day climate and interannual variability. By prescribing the boundary conditions in this way, future changes in the mean state are accounted for through the SSTs and lateral boundaries, while future changes in the transients and interannual variability prescribed through the lateral boundary conditions are not included. The methodology sets this study apart from the currently underway North American Regional Climate Change Assessment Program (NARCCAP), which is producing a set of 50 km resolution climate change simulations for the mid-twenty-first century by the direct downscaling technique, with several combinations of regional and global climate models.

Changes in the climatological average and interannual variability in rainfall are presented. Confidence in the predictions is strengthened by taking both validation- and ensemble-based approaches and by drawing on our physical understanding of the climate variability in these regions. The validation-based approach involves an assessment of the regional model's ability to realistically represent present day climate. In particular, we perform a rigorous validation of precipitation, including its diurnal cycle, which often poses a modeling challenge. The ensemble-based approach utilizes several global models for the prescription of the unknown future boundary conditions to the regional model. We support the predictions by providing a physical understanding of the atmospheric circulation anomalies that accompany the precipitation changes, with a focus on the Great Plains low-level jet, which plays an important role in present day rainfall variability.

3.2 Background

In this section, a review of the characteristics of warm season precipitation in the central U.S. is presented, as well as a description of the circulation features that

contribute to variability in precipitation. A discussion of relationships between SSTs and precipitation and the role of land-atmosphere feedbacks is also included. This is intended to serve as a guide for the analysis of the future climate change predictions and the validation of the regional climate model.

The summer climate of the central U.S. is characterized by a strong diurnal cycle in rainfall. The assimilated precipitation of the North American Regional Reanalysis (NARR; Mesinger et al. 2006) reveals a nocturnal peak over the Great Plains. Similarly, high horizontal (2 km) and temporal (15 minute) resolution radar data shows that over the central U.S. during June – August rainfall peaks in the late night to early morning hours (Carbone and Tuttle 2008), and that most of the rainfall is related to systems propagating eastward from the Continental Divide, a nocturnal reversal of the mountain-plains solenoid (Wolyn and McKee 1994), and moisture convergence associated with the Great Plains low-level jet. Radar data suggest there may be a secondary rainfall maximum related to daytime convection in the late-afternoon over the southern Great Plains (Carbone and Tuttle 2008). Hourly rain gauge data also indicate a dual peak in summer Great Plains rainfall, with rainfall events lasting 1 hour peaking at 0400-0600 LT and 1500-1700 LT, and events longer than 3 hours in duration peaking from 0000-0600 LT and contributing more to the total rainfall (Chen et al. 2009).

While a reasonable simulation of seasonal rainfall is more commonly produced by climate models, a proper simulation of the observed diurnal rainfall cycle often poses a challenge. GCMs tend to have difficulty capturing the nocturnal summer rainfall over the Great Plains, and often simulate one maximum in the afternoon (Lee et al 2007). Sensitivity experiments with one AGCM that does reproduce the observed diurnal rainfall cycle show that the simulation is sensitive to the choice of convection starting level and the convection trigger function related to level of free

convection. (Lee et al. 2008). The simulation of the diurnal cycle of rainfall is relatively insensitive to the model resolution, as no significant change is achieved by improving the horizontal model resolution by up to 50 km. Liang et al. (2004) also find that the convection parameterization has a large impact on the simulated diurnal cycle in a regional climate model, and Liang et al. (2006) show that simulations of both the present day and future climate are strongly dependent on the convection scheme. The importance of the convection scheme is further supported by Han and Roads (2004), who suggest that differences between the summer precipitation in the central U.S. simulated by a global model and a dynamically downscaled regional are largely related to the different convection parameterizations.

The Great Plains low-level jet (GPLLJ; Bonner 1968) is an important feature that supports the summer diurnal rainfall over the central U.S. It is a meridional jet aligned along the eastern side of the Rocky Mountain topography with a core at about 100°W and 900-850 hPa that transports moisture from the Gulf of Mexico to the interior of the central U.S. The GPLLJ is strongest in the summer months, peaking in June and July and, like the rainfall, has a strong diurnal cycle peaking around 0300 LT. While the jet is apparent in the monthly climatologies, it forms as individual events, which do not necessarily occur daily (e.g. Wu and Raman 1998). Experiments with an AGCM and linear and nonlinear stationary wave models suggest that the climatological GPLLJ is primarily maintained by transient vorticity forcing due to the modification of transient eddies by topography, specifically the interactions of the easterly wind along the southern edge of the North Atlantic subtropical high with the Sierra Oriental (Ting and Wang 2006). The nocturnal maximum in the GPLLJ is produced by the diurnal oscillation of the pressure gradient force and vertical diffusion, as suggested by AGCM simulations (Jiang et al 2007). The mechanism of the diurnal oscillation of vertical diffusion was proposed by Blakadar (1957) and is

supported by the abrupt reduction of friction at sunset. Holton (1967) theorized the importance of the diurnal oscillation of the pressure gradient force, which is caused by differential heating and cooling over the topography. Maximum afternoon heating over the topography induces easterly winds on the eastern side of the mountain and, due to the inertial oscillation, the flow curves to the north with a maximum southerly wind speed at midnight.

Since the GPLLJ transports large amounts of moisture from the Gulf of Mexico into the central U.S., it plays an important role in warm season rainfall variability. For example, the rainfall anomalies during the Great Plains flood of 1993 and drought of 1988 related strongly to changes in the strength of the GPLLJ and the associated moisture transport and convergence (Weaver et al. 2009a). Enhanced moisture transport by the GPLLJ is also found to support composites of observed wet events (Mo et al. 1997).

Results from several AOGCMs from the Intergovernmental Panel on Climate Change Fourth Assessment Report (IPCC-AR4) predict an increase in the strength of the GPLLJ during April – June, which is related to a strengthening and westward expansion of the North Atlantic subtropical high that is associated with greater warming over the continental U.S. compared to the subtropical Atlantic Ocean (Cook et al. 2008). The importance of zonal land/sea temperature gradients in modifying the strength of the GPLLJ is supported by idealized GCM experiments that produce a stronger GPLLJ and enhanced Great Plains rainfall as a result of cold Atlantic SSTAs (Weaver et al. 2009b).

The North Atlantic Oscillation (NAO), which is measured by the shift in atmospheric mass between the North Atlantic subtropical high and the Icelandic low, also contributes to present day variability in the warm season central U.S. precipitation. Conditions during the warm season in the upper (lower) Midwest tend

to be drier (wetter) during the positive phase of the NAO, which is characterized by a strong North Atlantic subtropical high and Icelandic low (Weaver and Nigam 2008). This may be related to North Atlantic SSTs, as Paeth et al. (2003) find that the positive (negative) phase of the NAO tends to occur with cooler (warmer) subtropical Atlantic SSTs and warmer (cooler) Atlantic SSTs between 30°N – 45°N.

Several studies document the role of North Atlantic and tropical Pacific SSTs in contributing to North American drought. Observations indicate that Great Plains droughts lasting less than 3 months are most closely related to simultaneous cold tropical Pacific and subtropical North Atlantic SSTAs, while droughts lasting 6 months or more are related to simultaneous and preceding (by 6 months) Indian and tropical Pacific SSTs and simultaneous SSTs in the subtropical North Atlantic (Wu and Kinter 2009). Trenberth et al. (1988) and Trenberth and Branstator (1992) have linked the onset of the central U.S. drought of 1988 to SSTAs in the tropical Pacific, which forced a shift in the intertropical convergence zone, producing atmospheric heating anomalies that supported the anomalous North American circulation that initiated the drought. The drought conditions of the 1930s dust bowl are attributed to both cold tropical Pacific and warm tropical Atlantic SSTAs on the decadal time scale through AGCM simulations, although there is a southward bias to the location of the simulated drought center (Schubert et al. 2004; Seager et al. 2008). Cook et al. (2008) find that with the SST forcing alone, model simulations are unable to reproduce the intensity and spatial pattern of the 1930s drought, but that accounting for the increased dust aerosol loading enhances the severity of the drought and improves the location. Findell and Delworth (2010) have also found that cold Pacific SSTs are associated with U.S. drought.

Atmospheric variability may also play a significant role in U.S. drought. Hoerling et al (2009) find that drought over the southern Great Plains is related to

SSTs, especially strong La Nina, while drought over northern Great Plains is less sensitive to SSTs and may be more related to random atmospheric variability. Combined global and regional modeling suggests that different physical processes contributed to the onset, maintenance, and termination of the Oklahoma-Texas drought of 1998 (Hong and Kalnay 2000). SSTAs most strongly contributed to the early rainfall deficit, with secondary contributions from the atmospheric conditions associated with the decaying warm El Nino event, while a strong land-atmosphere feedback prolonged the drought through decreased soil moisture and evaporation. The drought ended when the strength of the local feedbacks were dominated by other factors.

Many other studies find that drought conditions are sustained and intensified by land-atmosphere interactions. Wu and Kinter (2009) attribute positive land-atmosphere feedbacks through soil moisture and precipitation to extending the persistence of drought, and Schubert et al. (2004) similarly find that land-surface interactions enhanced the severity of the drought 1930s. AGCMs suggest strong land-atmosphere coupling over the central Great Plains region (Koster et al 2004), while regional climate model simulations find that land-atmosphere coupling (through soil moisture and convective rainfall) dominates summer precipitation variability over the northern, but not southern Great Plains (Zhang et al. 2008).

There is evidence that the role of soil moisture and evaporation in supporting precipitation anomalies depends on the wetness of the soil. AGCM simulations suggest that long-term wet conditions in the Great Plains are more predictable than droughts due to a dependence of the strength of land-atmosphere coupling on the soil conditions, such that dry soil conditions increases the strength of the coupling (Schubert et al. 2007). This dependence on soil moisture is also suggested by observations, which find that evaporation supplied 41% of rainfall over the

Mississippi River basin during the drought of April – July of 1988, but only 33% during the flood of April – July of 1993 (Dirmeyer and Brubaker 1999). In addition, at the maximum of the flood in July of 1993, water recycling was reduced and moisture transport from the Gulf of Mexico increased, while at the peak of the 1988 drought in June, water recycling was at a maximum.

3.3 Methodology

Regional climate model (RCM) simulations are conducted with the Weather Research and Forecasting Model (WRF; Skamarock et al. 2008) version 3.1. This model has been developed and maintained by the National Center for Atmospheric Research (NCAR). It is a non-hydrostatic model with 30 vertical levels, and the top of the atmosphere is set to 30 hPa. The following user-specified options are utilized: monthly varying albedo, fractional sea ice, and gravity wave drag.

Physical parameterizations for the simulations include the Lin et al. microphysics scheme (Lin et al. 1983; Rutledge and Hobbs 1984), CAM longwave and shortwave radiation schemes (Collins et al. 2004), Monin-Obukhov surface scheme (Monin and Obukhov 1954), Yonsei University (YSU) planetary boundary layer scheme (Hong et al. 2006), and new Kain-Fritsch cumulus scheme (Kain and Fritsch 1990; 1993).

The land-surface is represented by the NOAH land-surface model (Chen and Dudhia 2001) which solves heat and moisture transfer equations at four levels in the soil column and energy and moisture budget equations for the ground surface. The NOAH land-surface model also calculates snow cover and runoff, and includes canopy effects. Land surface categories are prescribed according to the 10-minute resolution 24-category United States Geological Survey (USGS) data set.

A nested domain is utilized for this study. The parent domain, which uses 90

km horizontal resolution and a 6-minute time step, is shown in Figure 3.1a with topography as resolved in the simulations. It includes most of North America and the tropical and subtropical Atlantic Ocean and extends from 125.1°W – 14.9°W and 10.8°N – 65.4°N. The inner domain, shown in Figure 3.1b, uses 30 km horizontal resolution and a 2-minute time step, and covers the central U.S. from 103.0°W – 84.3°W and 20.2°N – 50.4°N. The fine resolution of the inner domain lends the advantage of resolving the GPLLJ and topography well and providing information suitable for regional scale analysis. The boundaries of the parent domain ensure that the North Atlantic subtropical high fits within the domain.

The control simulation includes the years 1981 through 2000 and consists of twenty annual integrations. For the initial model spin up, the control run is started on January 1, 1980 and run through December 1, 1980. The simulation of the year 1981 is then initialized on December 1, 1980 and run through December 31 of 1981, with the first month disregarded for spin-up. Each of the twenty annual integrations for the control simulation is formed this way, with one month of model spin-up. At each annual model restart, the atmospheric variables are reinitialized from reanalysis products, while the surface temperature, snow cover, and soil moisture and temperature are initialized from the previous model integration. The atmosphere is reinitialized annually because after several years of continuous simulations, the model became unstable on the boundary of the inner domain where there is a large topography gradient. The surface variables are carried over from the model so that the memory retained by the soil and snow fields is included. Model output is saved every three hours.

Soil moisture and temperature are initialized from the North American Regional Reanalysis (NARR; Mesinger et al. 2006) at 32 km resolution from the January average of 1980 – 2000. Since the NARR does not contain the entire parent

domain, lateral boundary conditions for the control simulation are prescribed from the 6-hourly National Center for Environmental Prediction/Department of Energy Atmospheric Model Intercomparison Project II (NCEP/DOE AMIP-II) Reanalysis (Kanamitsu et al. 2002) at 2.5° resolution. The European Centre for Medium-Range Weather Forecasts (ECMWF 2002) reanalysis is used to prescribe SSTs, which are linearly interpolated from monthly averages to the 6-hourly timescale, and the initialization of snow cover. Fractional sea ice is prescribed according to the monthly NCEP/NCAR reanalysis (Kalnay et al. 1996).

For the future climate simulation, which represents the years 2041 – 2060 and consists of twenty annual integrations designed similarly to the control simulation, the atmospheric CO_2, N_2O, CH_4, CFC-11, and CFC-12 concentrations are prescribed based on the SRESA2 emissions scenario (IPCC 2000). The CO_2 concentration updates annually, from 339.6 to 370.5 ppm in the control simulation, and 533.0 to 578.0 ppm in the future simulation. The N_2O, CH_4, CFC-11, and CFC-12 concentrations are prescribed based on the 20-year average and are modified from 0.311 ppm, 1.714 ppm, 0.280 ppb, and 0.503 ppb in the control simulation to 0.373 ppm, 2.562 ppm, 0.123 ppb, and 0.362 ppb in the future. The SRESA2 emissions scenario projects a relatively high emissions rate and is chosen since it is likely to produce a clearer signal than a lower emissions scenario.

The method used in this study to produce future climate projections is similar to that developed in Patricola and Cook (2009), in which integrations for the future are performed by the regional model, and AOGCMs provide information for surface and lateral boundary conditions as anomalies. This method differs from the traditional regional downscaling approach in which lateral and surface boundary conditions are prescribed to a regional model directly from a global model. Here, we have prescribed boundary conditions for the control simulation from 6-hourly reanalysis products and

created LBCs, SSTs, and sea ice for the future by adding linearly interpolated monthly climatological anomalies from coupled atmosphere-ocean GCMs (AOGCMs) to the reanalysis products. (For example, the lateral boundary conditions for the control simulation at 00z on 15 June 1981 are taken from the reanalysis at 00z on 15 June 1981, while the lateral boundary conditions for the future simulation at 00z on 15 June 2041 are calculated by adding the reanalysis at 00z on 15 June 1981 to the AOGCM climatological monthly average of June 2041 – 2060, minus the AOGCM climatological monthly average of June 1981 – 2000.) Therefore, the future lateral boundary conditions account for changes in the mean state of remote forcings, but do not include changes in transients or interannual variability. That is, the transients and interannual variability prescribed in the lateral boundary conditions is the same between the control and future simulations. (This does not imply that transients generated within the domain are the same between the control and future simulations.) The benefit of this method is that by prescribing the boundary conditions this way, the quality of the control simulation is preserved and the impact of model error on the regional climate projections is reduced.

The approach taken in Patricola and Cook (2009) relies on ensembles to measure the confidence of the projections. Whereas GCM ensembles are generated by integrating multiple simulations with the same physical parameterizations and forcings, but slightly different initial conditions, Patricola and Cook (2009) create nine future RCM ensemble members by using anomalies in surface and lateral boundary conditions from nine AOGCM simulations. This is done because the predictions from the AOGCMs themselves were uncertain for the region of interest. For the central U.S., there is less uncertainty in the predictions from the AOGCMs, and so the ensembles are designed with a focus on understanding the physical processes of the climate change on the regional scale. For this application, we account for

uncertainties associated with the details of the AOGCMs' projections of SSTs and lateral boundary conditions by averaging the boundary conditions from six AOGCMs to create one future simulation. Boundary conditions are derived from the following AOGCMs which are included in the World Climate Research Programme's (WCRP's) Coupled Model Intercomparison Project phase 3 (CMIP3) multi-model dataset (Meehl et al. 2007) and are archived by the Program for Climate Model Diagnosis and Intercomparison: CCCMA_CGCM3.1, CNRM-CM3, ECHAM/MPI-OM, GFDL-CM2.0, NCAR_PCM, and UKMO-HadCM3.

Future lateral boundary conditions are taken from the monthly climatological ensemble average of the six AOGCM simulations, which are interpolated to 6-hourly intervals on the grid of the reanalysis, are applied as anomalies to the 6-hourly values of the NCEP/DOE AMIP-II reanalysis used in the control simulation. The LBCA anomalies are the 2041-2060 average forced by the SRESA2 emissions scenario minus the 1981-2000 average from the twentieth century (named 20C3M) simulation. For the AOGCMs that have missing information below the local ground surface, the anomaly from the lowest level provided by the AOGCM is applied to the reanalysis value.

SSTs and sea ice for the future are also derived from the monthly climatological ensemble average of the six AOGCM simulations, interpolated to the grid of the reanalysis, and applied as anomalies to the monthly values from the ECMWF and NCEP reanalysis, respectively. These monthly values are then linearly interpolated to the 6-hourly timescale.

A moisture budget analysis, similar to that derived in Lenters and Cook (1995), is particularly useful to develop an understanding of the connections between the future precipitation and circulation anomalies, and is presented in Section 3.5c. The moisture budget is expressed as

$$P = E + C + A + TC + TA + R, \tag{3.1}$$

and calculates the contributions to precipitation (P) from evaporation (E), vertically-integrated time-mean moisture convergence (C) and advection (A), moisture convergence due to transient eddies (TC), moisture advection due to transient eddies (TA), and the residual (R), which includes topographical effects and numerical error. The terms C, A, TC, and TA are defined below. The contribution from the vertically-integrated time-mean moisture convergence, hereafter referred to as "time-mean moisture convergence" is defined as

$$C = -\frac{1}{g\rho_w}\sum_{p=\bar{p}_s}^{100hPa}(\bar{q}\nabla_h \cdot \bar{V})\Delta p, \tag{3.2}$$

where g is the acceleration due to gravity, ρ_w is the density of water, p is pressure, $\bar{p}_s$ is the monthly averaged surface pressure, $\bar{q}$ is the monthly averaged water vapor mixing ratio, $\bar{V}$ is the monthly averaged horizontal wind vector, and ∇_h is the horizontal divergence operator. Note that, as pointed out by Lenters and Cook (1995), the terminology used here is loose, and the "moisture convergence" term is the vertically integrated product of the mixing ratio and the wind convergence.

The vertically-integrated time-mean moisture advection, hereafter referred to as "time-mean moisture advection" is defined as

$$A = -\frac{1}{g\rho_w}\sum_{p=\bar{p}_s}^{100hPa}(\bar{V}\cdot\nabla_h \bar{q})\Delta p \tag{3.3}$$

Vertically-integrated moisture convergence due to transient eddies is defined as

$$TC = -\frac{1}{g\rho_w}\sum_{p=p_s}^{100hPa}(q'\nabla_h \cdot V')\Delta p, \tag{3.4}$$

where V' is the perturbation horizontal wind vector defined as $V' = V - \bar{V}$ and q' is the perturbation water vapor mixing ratio defined as $q' = q - \bar{q}$. The

vertically-integrated moisture advection due to transient eddies is defined as

$$TA = -\frac{1}{g\rho_w}\sum_{p=p_s}^{100hPa}(V'\cdot\nabla_h q')\Delta p \qquad (3.5)$$

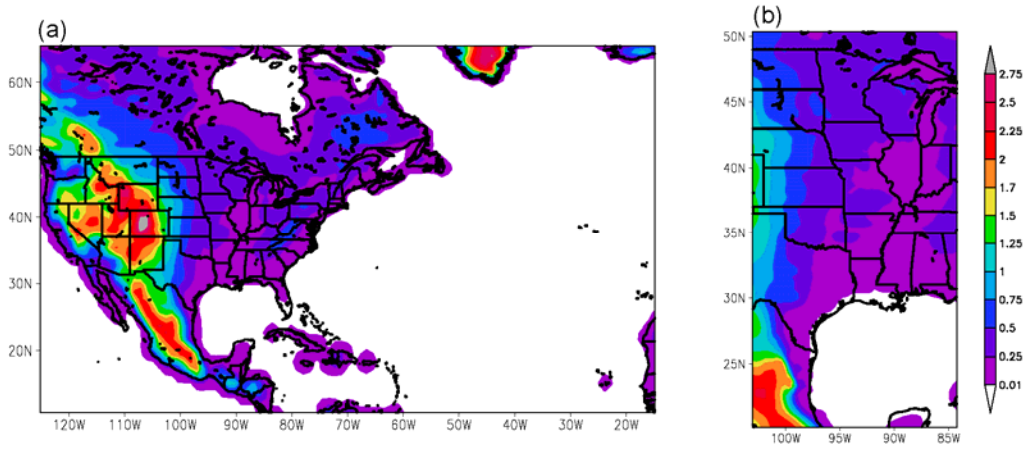

Figure 3.1. Topography (km) at (a) 90 km resolution on the parent domain and (b) 30 km resolution on the nested domain.

3.4 Model Validation

The ability of the regional model to represent the observed central U.S. climate and interannual variability is assessed to support confidence in the results. Particular attention is devoted to the validation of precipitation, since this is such an important variable for impacts and is also one of the more difficult variables to simulate. The ability of the regional model to simulate circulation features important to variability in central U.S. precipitation is also assessed.

Figures 3.2a-d show assimilated precipitation rates from the NARR averaged for March – April, May – June, July – August, and September – October of 1981 – 2000 on a 32 km grid, for comparison with precipitation rates from the control simulation on the 90 km grid (Figures 3.2 e-h). Note that precipitation from the NARR is based on rain gauge observations over the continental U.S. and is considered a high-quality product. Therefore, "assimilated precipitation" and "observations" are

used interchangeably when referring to the precipitation from the NARR. In March and April (Fig. 3.2a), there is a rainfall maximum located over Louisiana and Mississippi that shifts to the central and southern Mississippi River region in May and June (Fig. 3.2b), with a strong zonal gradient in rainfall to the west. The RCM captures the shift of the rainfall maximum from March and April (Fig. 3.2e) to May and June (Fig. 3.2f) well, although the location of the rainfall maximum is simulated to the east in May and June. Despite this issue, the RCM simulates the location of the maximum well compared to many AOGCMs. The observed rainfall maximum shifts to the northern Great Plains in July and August, and there are also high rainfall rates over Florida (Fig. 3.2c). The RCM reproduces the location of these maxima well, and although precipitation rates over the northern Great Plains (Florida) are weaker (stronger) than observed (Fig. 3.2g), the magnitudes of the simulated rainfall are reasonable within the accuracy of the observations. In September and October (Fig. 3.2d) the maximum in the central U.S. retreats southward and rainfall rates are much weaker over the southeastern states, and the RCM also represents this general pattern (Fig. 3.2h).

Since land-atmosphere interactions are known to be important over the Great Plains, a validation of precipitation minus evaporation (PME) is presented. A map of the averaging regions selected for analysis is shown in Figure 3.3. The choice of averaging regions is motivated by both the characteristics of the present day precipitation climatologies as well as the future climate change signals. These regions include the northern and southern Great Plains, the Midwest, and the western and eastern South. Figure 3.4 shows the observed and modeled seasonal cycle of precipitation and PME for the northern and southern Great Plains regions. Observed rainfall over the southern Great Plains peaks in May and June at about 3.5 mm/day, just before the slightly weaker maximum of 3 mm/day in June over the northern Great

Plains (Fig. 3.4a). There is a secondary peak in September over the southern Great Plains, and over both regions precipitation is at a minimum during the winter months. The RCM captures the seasonal precipitation cycle well, producing the winter minimum and simulating a peak in the southern Great Plains that precedes that of the northern Great Plains, which occurs slightly earlier than observed. The secondary peak in the southern Great Plains is also simulated by the RCM. The only discrepancy is in the relative magnitudes of the summer rainfall maxima, with the RCM producing more rainfall in the northern than southern Great Plains. There is also a pronounced seasonal cycle in the PME over the Great Plains, with negative PME over the southern Great Plains from April through August in both the observations and RCM simulation (Fig. 3.4b). Over the northern Great Plains the observed and simulated onset of negative PME values begins one month later in May, and remains negative throughout August as well.

In addition to an excellent representation of climatological precipitation, the RCM is successful at reproducing observed drought and flood events. Figure 3.5 shows the precipitation anomalies for April – June of 1988 and for May – August of 1993 relative to the 1981-2000 base period from the NARR and the control simulation. The RCM simulates the spatial extent and the magnitude of the drought of 1988 very well with anomalously dry conditions of -3mm/day over much of the central U.S. (Figs. 3.5a and b). The RCM produces drying that is weaker than observed over Louisiana, which may be related to weak rainfall rates over that region in the climatology. The observed flood of 1993 was centered over the northern Great Plains with the largest anomalies of up to 5 mm/day over Iowa, while the southeastern U.S. experienced weak drying of 1-2 mm/day (Fig. 3.5c). The RCM simulates the rainfall anomalies of the summer of 1993 reasonably well, with wetter conditions over the entire central U.S. (Fig. 3.5d). Unobserved wetter conditions are simulated over

Louisiana and the drying in the southeastern U.S. is not reproduced. Despite these issues in the simulation of 1993, the regional model is able to capture the occurrence of strong drought and flood events quite well.

Figure 3.6 shows the diurnal cycle of rainfall averaged over June – August from the NARR, the 30 km domain of the regional model control simulation, and a control simulation from an AOGCM, the GFDL CM2.0 of the Geophysical Fluid Dynamics Laboratory. The summer rainfall in the NARR peaks at 0000 – 0300 LT and is at a minimum at 1200 LT. The regional model simulates two maxima; the stronger maximum is associated with daytime convection and occurs at 1800 LT, while the weaker maximum at 0300 – 0600 LT is associated with nocturnal rainfall processes, such as convergence associated with the GPLLJ and eastward propagating systems. While the nocturnal (daytime) rainfall is under (over) represented by the regional model, the dual maximum suggests that the convection scheme is representing the correct physical processes. (Note that radar data suggests a secondary afternoon rainfall maximum.) For comparison, the AOCGM incorrectly simulates one rainfall maximum at 1500 LT, and produces a minimum in rainfall overnight. The proper simulation of the diurnal cycle is also an issue in the National Aeronautics and Space Administration Global Modeling and Assimilation Office (NASA GMAO) AGCM, while the National Center for Environmental Prediction Global Forecasting System model (NCEP GFS) produces a realistic diurnal cycle (Lee et al. 2007). While there is clearly room for improvement in the regional model simulation of the diurnal rainfall cycle, it more closely represents the observations compared to some, but not all, AOCGM simulations.

A validation of the North Atlantic subtropical high and Great Plains low-level jet (GPLLJ) is included since these circulation features are important in understanding precipitation variability over the central U.S. We use the NARR to validate the

GPLLJ since its horizontal resolution is much finer than that of the NCEP-II reanalysis (32 km versus 2.5°). Since the NARR does not cover the entire parent domain of the RCM simulation, the NCEP/NCAR reanalysis (Kalnay et al. 1996) is used to validate the North Atlantic subtropical high.

The regional model reproduces the characteristics of the GPLLJ and its seasonal cycle extremely well. Figure 3.7 shows a vertical cross section of the 1981 – 2000 climatological monthly meridional wind averaged from 28°N – 32°N from the NARR (Figs. 3.7a-d) and the 30 km nest of the control simulation (Figs. 3.7e-h) from May through August. The core of the GPLLJ is located between 103°W-95°W and 950hPa – 850hPa and reaches a maximum of 6.5 m/s in June and July. The RCM captures the position and seasonal cycle of the GPLLJ well, with a slightly stronger, but reasonable, jet peaking in June and July at 7.5 m/s. In addition, the RCM simulates the alignment of the GPLLJ along the topography, which is often not captured in GCM simulations with coarse horizontal resolution.

In addition to realistically representing the seasonal cycle of the GPLLJ, the RCM captures the diurnal cycle of the jet very well. Figure 3.8 plots the meridional wind (shaded) and horizontal wind (vectors) at 925 hPa at 3-hourly intervals averaged for June from the NARR. The meridional wind is positive throughout the day, but is markedly stronger from 0000 – 0600 LT (Figs. 3.8c-e). Figure 3.9 is similar to Figure 3.8, but for the control simulation, and shows a similar diurnal cycle in the GPLLJ compared with the reanalysis. The magnitude of the meridional wind is comparable between the RCM and the NARR, with the RCM producing a slightly stronger nighttime maximum. The model also reproduces the location of the core over eastern Texas.

Geopotential heights and winds at 925 hPa are shown in Figure 3.10 averaged March – April, May – June, July – August, and September – October of 1981 – 2000

from the NCEP/NCAR reanalysis (Kalnay et al. 1996) and the control simulation on the 90 km grid. The RCM reproduces the strength, position, and seasonal cycle of the North Atlantic subtropical high (NASH) very well, and captures the peak of about 875 m in July – August. The RCM also simulates the southern extent of the Icelandic Low well, with a deeper, more organized center in March – April and September – October than during the summer months. In addition, the simulated features of the NASH and Icelandic Low compare well with the reanalysis during individual years (not shown).

The RCM produces an excellent simulation of the important circulation features as well as a reasonable seasonal cycle, diurnal cycle and interannual variability in precipitation over the central U.S. that is suitable for applications to study the future climate on regional space scales.

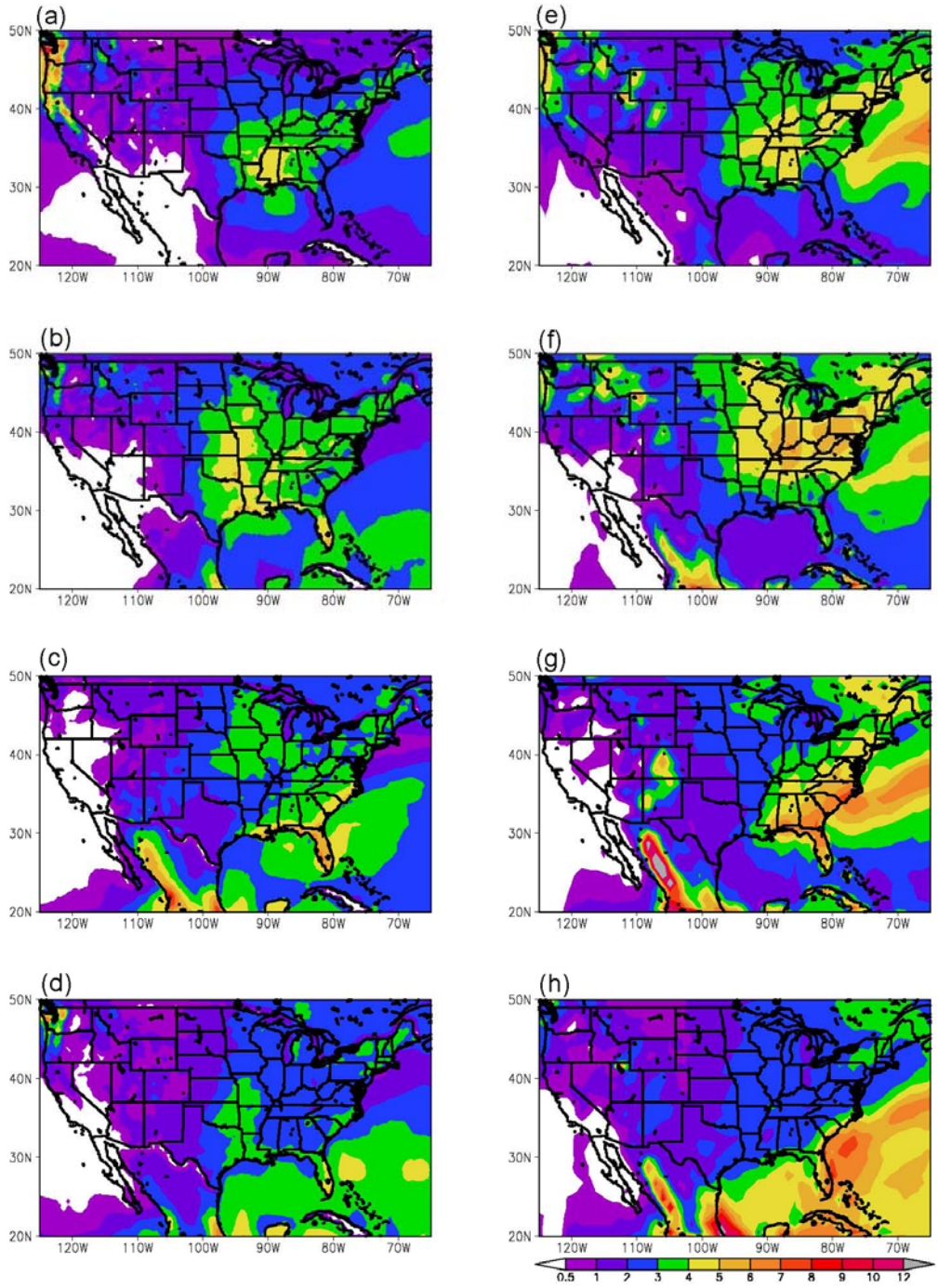

Figure 3.2: Precipitation rate (mm/day) averaged (a) March – April, (b) May – June, (c) July – August, and (d) September – October of 1981 – 2000 from the NARR. Precipitation rate (mm/day) averaged (e) March – April, (f) May – June, (g) July – August, and (h) September – October of 1981 – 2000 from the 90 km domain of the control simulation.

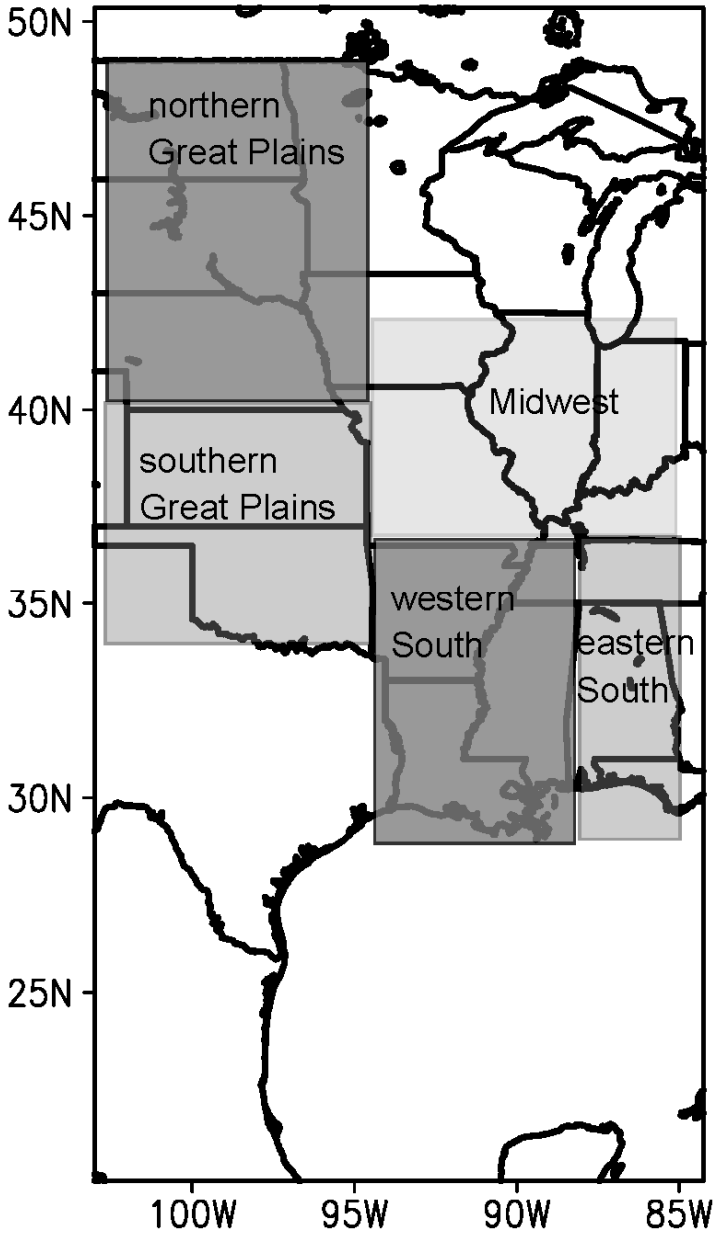

Figure 3.3: Averaging regions including the northern (40.1°N-48.9°N, 103.0°W-94.3°W) and southern (33.8°N-39.8°N, 103.0°W-94.3°W) Great Plains, the Midwest (36.8°N-42.3°N, 94.0°W-85.0°W), and the western (29.0°N-36.6°N, 94.0°W-88.3°W) and eastern (29.0°N-36.6°N, 88.0°W-85°W) South.

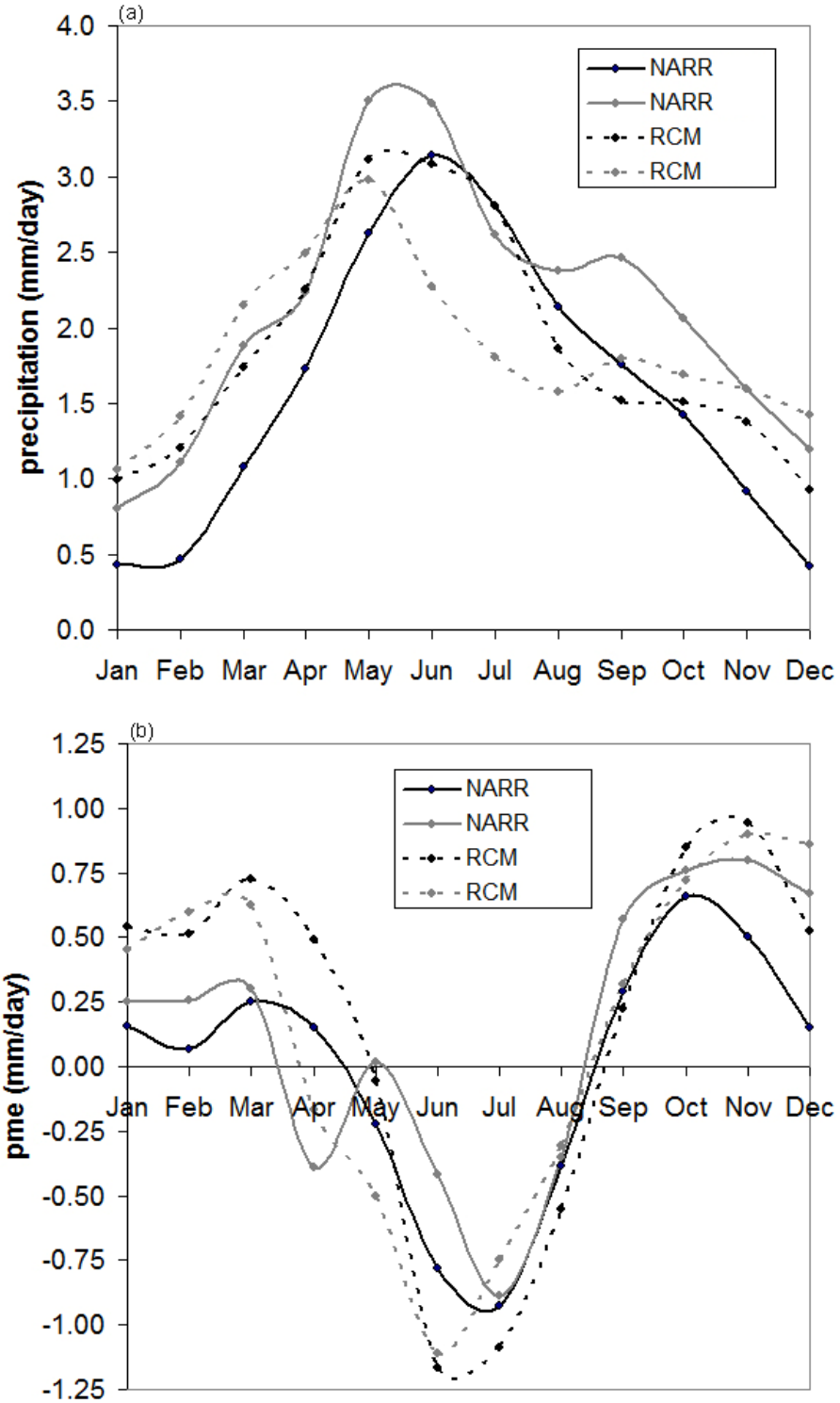

Figure 3.4: (a) Precipitation rate (mm/day) from the NARR over the northern Great Plains (solid black) and southern Great Plains (solid grey) and from the control simulation over the northern Great Plains (dotted black) and southern Great Plains (dotted grey) averaged over 1981 – 2000, and (b) the same as (a), except for precipitation minus evaporation.

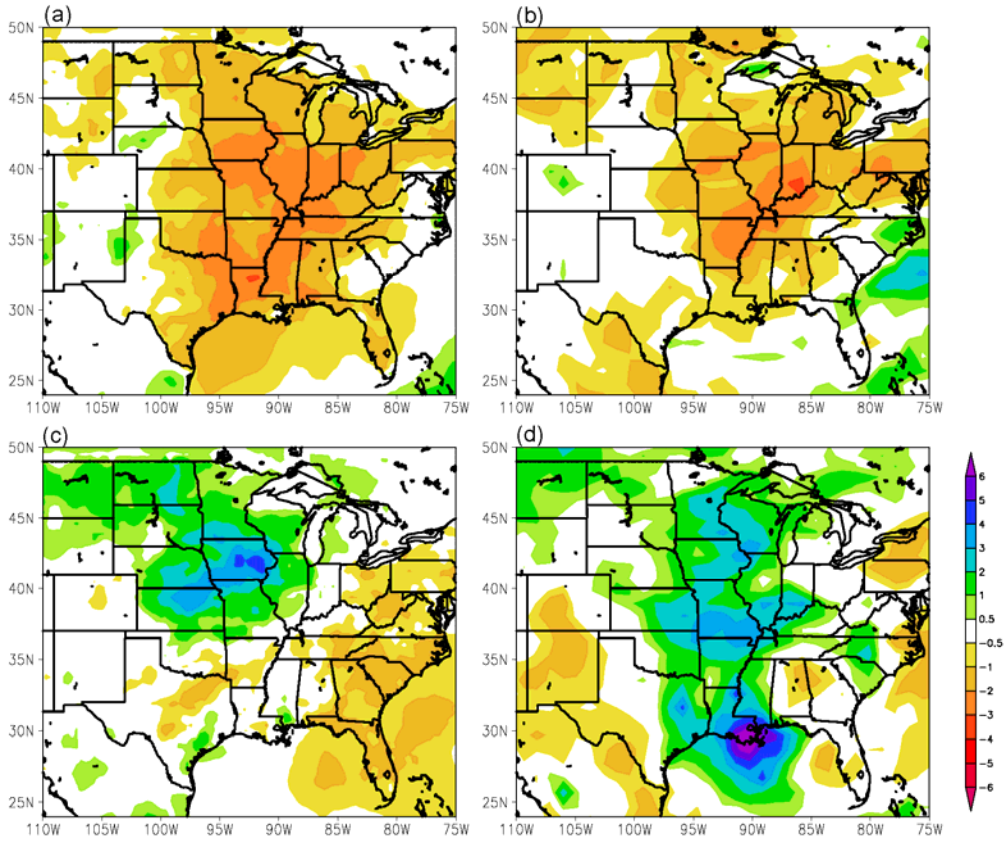

Figure 3.5: Precipitation anomalies (mm/day) relative to the 1981 – 2000 base period from April through June of 1988 from the (a) NARR and (b) 90 km domain of the control simulation, and from May through August of 1993 from the (c) NARR and (d) 90 km domain of the control simulation.

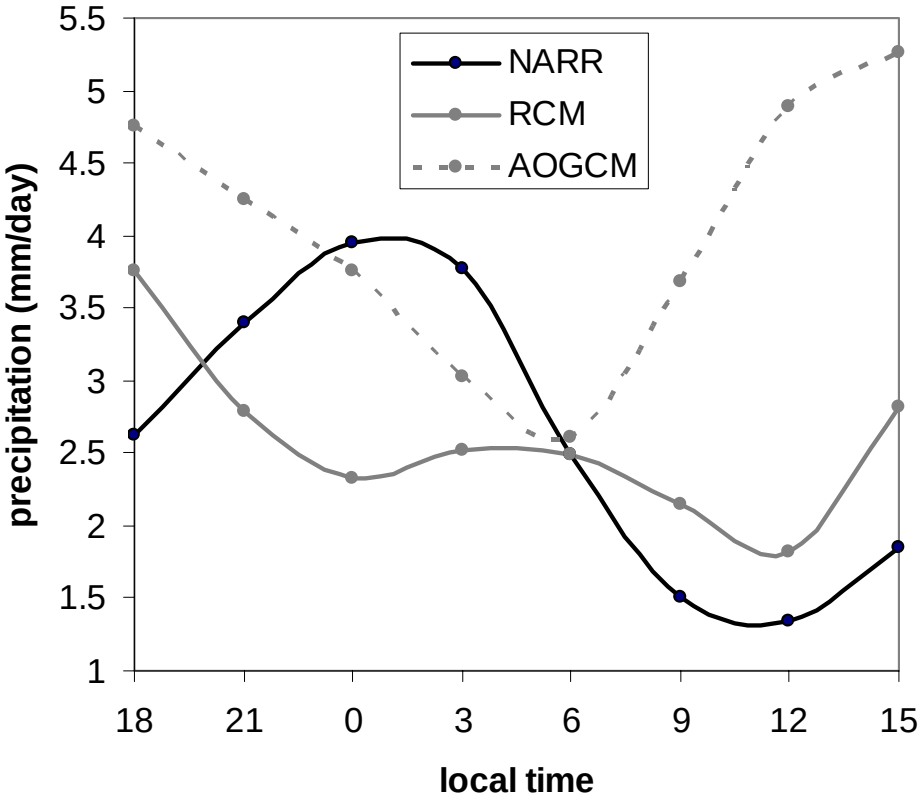

Figure 3.6: Climatological 3-hourly precipitation (mm/day) averaged over June – August from the NARR (solid black), the 30 km domain of the regional model control simulation (solid grey), and the GFDL 2.0 AOGCM (dash grey) for the northern Great Plains.

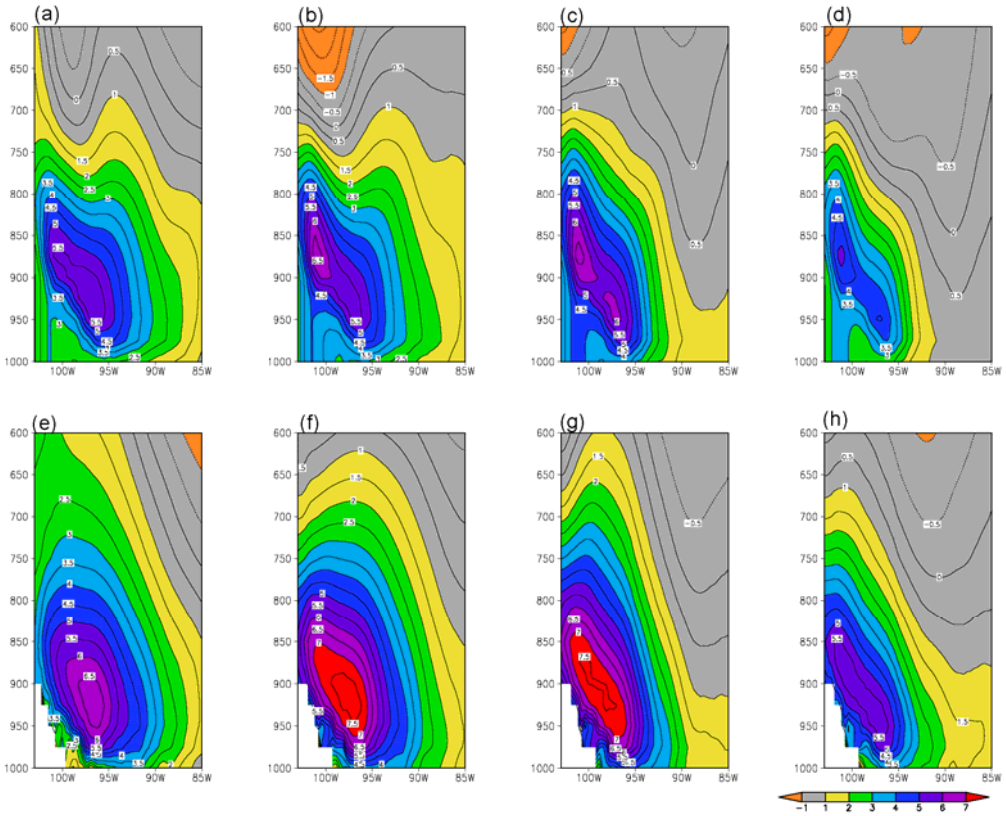

Figure 3.7: Vertical cross sections of the meridional wind (m/s) averaged from 28°N – 34°N for (a) May, (b) June, (c) July, and (d) August of 1981 – 2000 from the NARR and for (e) May, (f) June, (g) July, (h) and August of 1981 – 2000 from the 30 km domain of the control simulation. Contour interval is 0.5 m/s. Topography is shaded white in the RCM simulation, while the data is interpolated through the topography in the NARR.

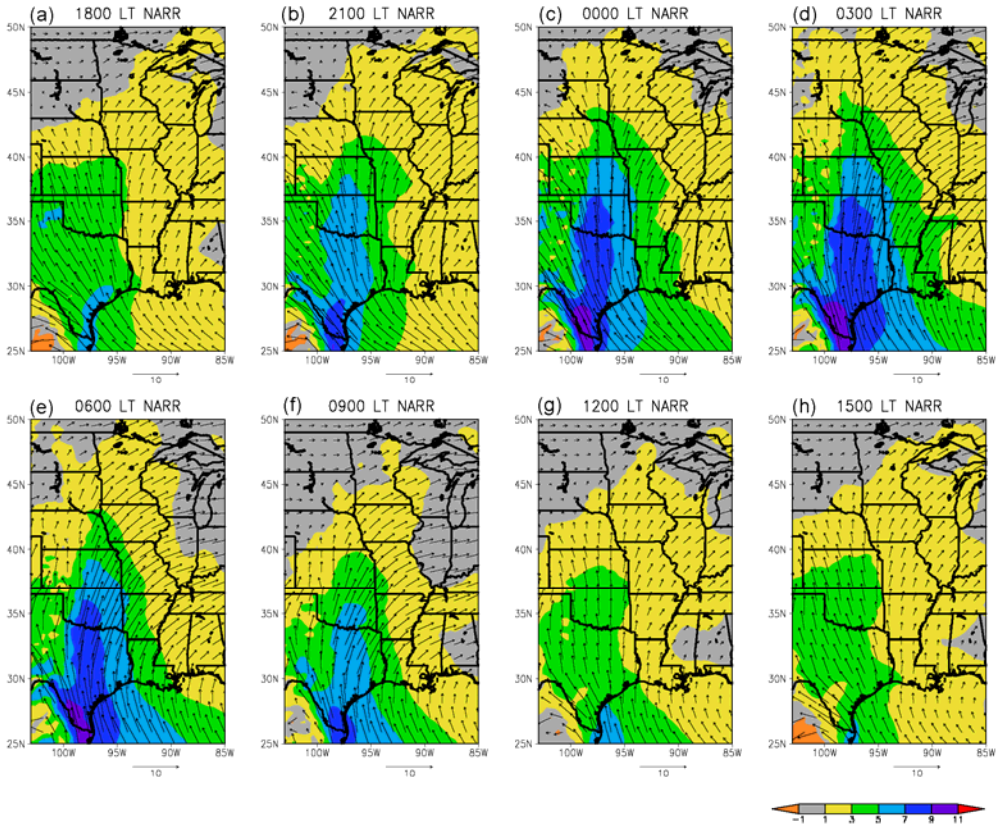

Figure 3.8: The meridional (shaded; m/s) and horizontal (vectors; m/s) wind at 925 hPa averaged during June of 1979 – 2007 at (a) 1800, (b) 2100, (c) 0000, (d) 0300, (e) 0600, (f) 0900, (g) 1200, (h) and 1500 LT from the NARR.

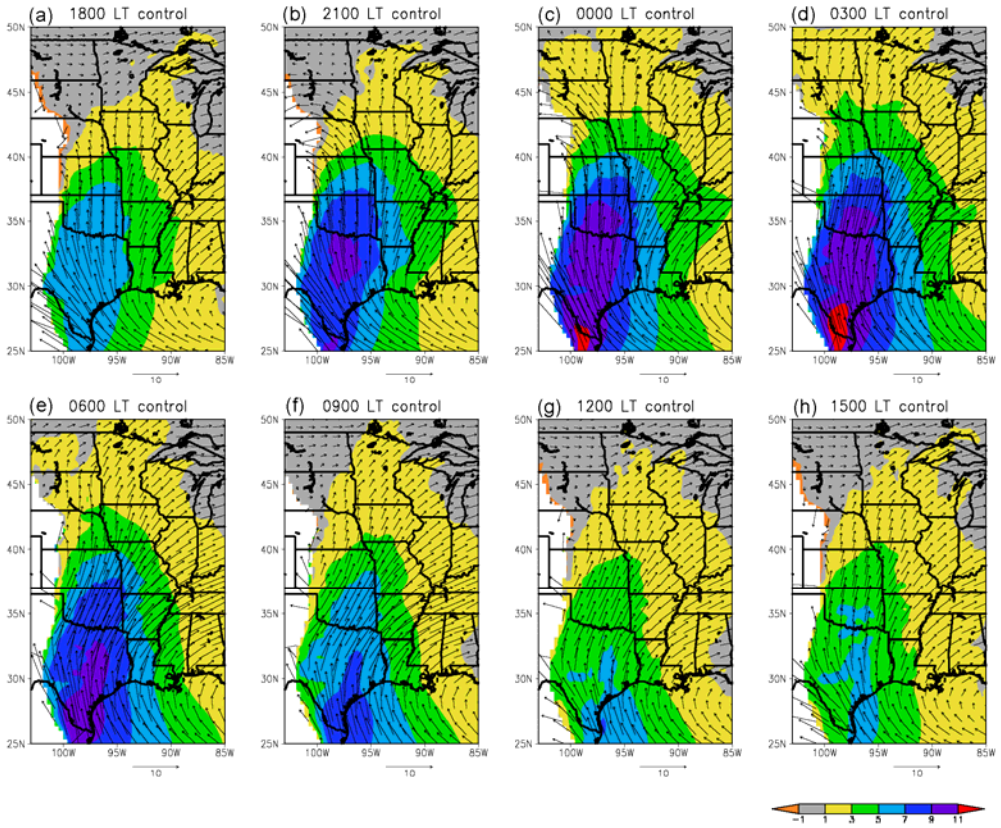

Figure 3.9: The meridional (shaded; m/s) and horizontal (vectors; m/s) wind at 925 hPa averaged during June of 1981 – 2000 at (a) 1800, (b) 2100, (c) 0000, (d) 0300, (e) 0600, (f) 0900, (g) 1200, (h) and 1500 LT from the 30 km domain of the control simulation. Topography is shaded white.

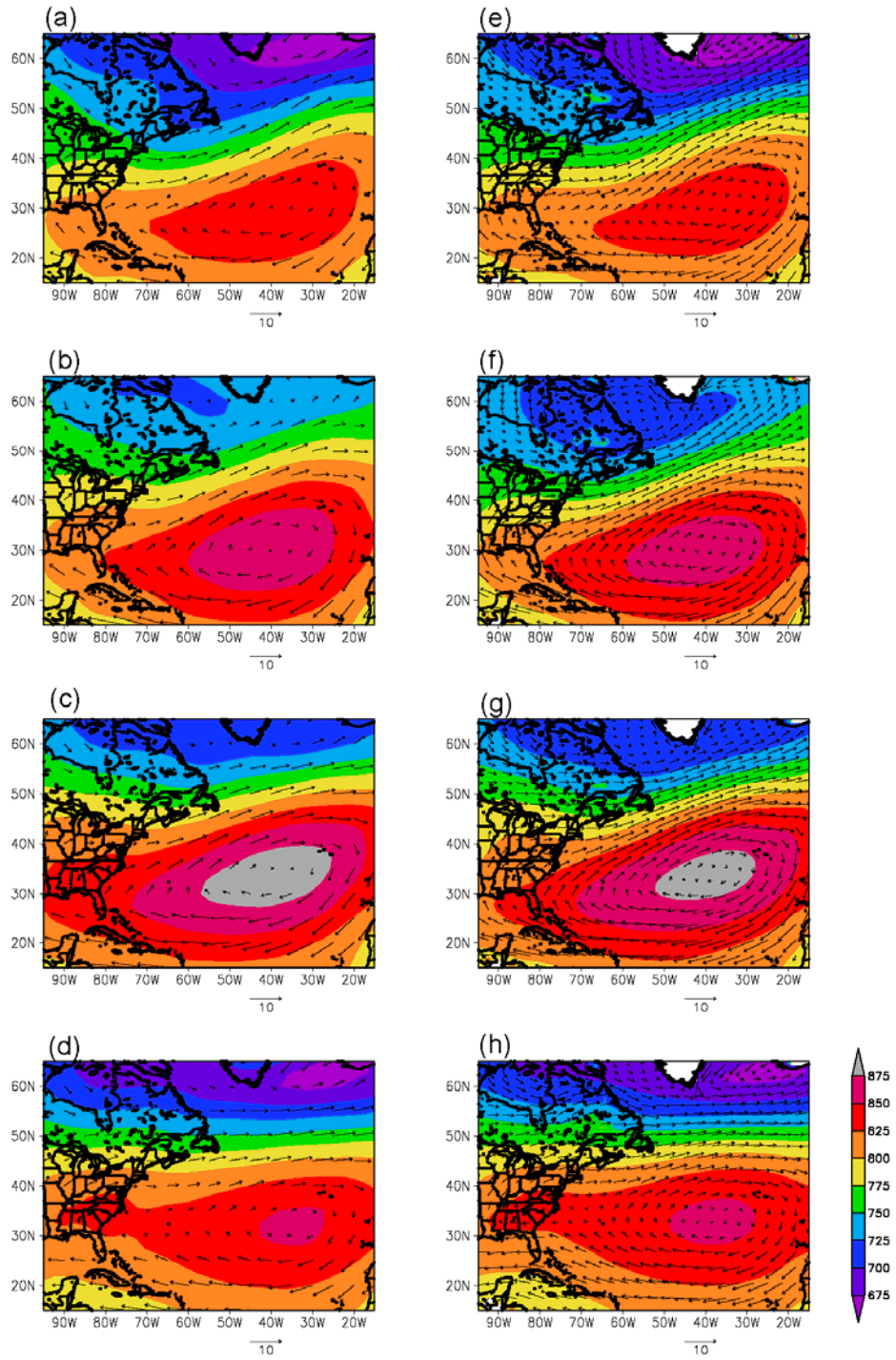

Figure 3.10: Geopotential heights (m) and wind vectors (m/s) at 925 hPa averaged over (a) March – April, (b) May – June, (c) July – August, and (d) September - October of 1981-2000 from the NCEP/NCAR reanalysis and averaged over (e) March – April, (f) May – June, (g) July – August, and (h) September – October of 1981-2000 from the parent domain of the control simulation. White regions are underground in the model simulations, while variables are interpolated through topography in the reanalysis.

3.5 Results

Regional climate change predictions for the central U.S., including changes in climatological and extreme rainfall and temperature, are presented in Section 3.5a. A dynamical analysis that focuses on the changes in the GPLLJ and North Atlantic subtropical high that support the precipitation anomalies is presented in Section 3.5c to enhance the confidence in the climate predictions.

3.5a Regional climate predictions - precipitation

Future anomalies in the seasonal cycle of precipitation are shown in Figure 3.11 for the five averaging regions (Fig. 3.3). The anomalies are generally coherent among the northern and southern Great Plains, Midwest, and eastern and western South regions, with wetter conditions in the spring, drying in the summer, and for some regions, wetter anomalies again in the fall. Over the southern Great Plains and Midwest, the future changes are very similar, with wetter conditions occurring in March – May, drying in June – August, and positive anomalies returning in September – October. While the absolute anomalies tend to be weaker for the southern Great Plains, ranging from -0.25 – 0.33 mm/day compared to -0.33 – 0.5 mm/day in the Midwest, the relative changes are about equal, with the spring, summer, and fall anomalies peaking near +8%, -15%, and +15% over both regions. The precipitation anomalies over the northern Great Plains region are similar in absolute (relative) magnitude to those over the southern Great Plains (southern Great Plains and Midwest), but the wetter spring and drier summer conditions are delayed by one month over the northern compared to the southern Great Plains, and the summertime drying continues throughout the fall months. Over both the northern and southern Great Plains, conditions are wetter during the winter months, by as much as 15-20% in January.

Precipitation anomalies over the western and eastern South regions, although generally similar, are less consistent with the northern regions and each other in timing and magnitude. The western South region experiences prolonged positive anomalies of up to 13% from March through June, and a shorter dry (up to -10%) period occurring July – August, while the eastern South is projected to be wetter in March – April and drier May through August. The magnitude of the drying over the eastern South region in July and August peaks at -17% – -22%, with two individual years very strongly influencing the 20-year averages. The average drying when these years are not included is -11% and -17%. Projections are similar over both southern regions in September, with wetter conditions of 20-30%.

The two-sided t-test for differences of the mean is used to assess the significance of the monthly precipitation predictions. The tests are evaluated at the 15% rejection level since the interannual variability of precipitation is relatively large compared to other variables (e.g., temperature), the sample size is moderate (20 years for each the control and the future), and the climate forcings are relatively weak (mid-twenty-first century as opposed to end of the twenty-first century). Also, since the future precipitation anomalies are contained within the averaging regions shown in Figure 3.3, but generally do not cover the entire averaging region, the t-tests are calculated for averaging regions that are focused on the future precipitation response to eliminate regions where there is little change. The months selected for averaging focus on times when the future precipitation signals are strong. Table 3.1 shows months and averaging regions chosen to isolate the future precipitation predictions, the broader averaging region from Figure 3.3 which contains the focus region, as well as whether the monthly means are statistically different at the 15% level.

The precipitation predictions over the northern Great Plains are statistically insignificant at the 15% level in April when the interannual variability in precipitation

is relatively large compared to the other months, while the future wetter conditions in June and drier conditions in July and August over the northern Great Plains are statistically significant at the 15% level. The weaker drying in September in the northern Great Plains is not statistically significant, while over the Midwest, the projected drying in June and July is statistically significant at the 15% level. In the South, wetter conditions in April are insignificant, while the future drying in August and wetter conditions in September are statistically significant.

Table 3.1: Significance of monthly precipitation predictions. (NGP denotes the northern Great Plains.)

Averaging region	Primarily contained within	Month	Difference in precipitation	Significant at 15% level
40.0 – 43.5°N, 97.0 – 91.5°W	NGP	April	+12%	No
44.0 – 47.0°N, 102.0 – 96.0°W	NGP	June	+18%	Yes
44.0 – 47.0°N, 102.0 – 92.0°W	NGP	July	-19%	Yes
42.5 – 45.5°N, 98.0 – 92.0°W	NGP	August	-19%	Yes
42.0 – 45.0°N, 98.0 – 92.0°W	NGP	September	-13%	No
37.5 – 41.0°N, 96.0 – 88.0°W	Midwest	June	-17%	Yes
36.0 – 42.0°N, 90.0 – 85.0°W	Midwest	July	-20%	Yes
31.0 – 36.5°N, 95.0 – 85.0°W	South	April	+16%	No
30.5 – 36.5°N, 90.0 – 85.0°W	South	August	-21%	Yes
30.5 – 36.5°N, 94.0 – 85.0°W	South	September	+27%	Yes

While there are considerable precipitation anomalies apparent on the monthly timescale, the annual anomalies are weak, totaling only +1.9% over the southern Great Plains, -0.2% over the northern Great Plains, +0.8% over the Midwest, +3.2% over the western South and -1.5% over the eastern South regions.

In addition to the projected monthly climatological rainfall anomalies, there are changes in interannual variability. We present changes in interannual variability so that they may be used in comparison with other studies, and we draw on the presence or lack of regional coherence to provide some measure of the confidence in the predictions here, realizing that the sample size is moderate. Figure 3.12 shows

histograms of the seasonally averaged precipitation rates for the spring months from the 20 years of the control and future simulations for the northern and southern Great Plains and the Midwest. The seasonal average is displayed so that changes in the frequency of drought and flood events can be assessed. The three spring months selected for the averaging are chosen based when the monthly precipitation projections are positive. When conditions are projected to be wetter over the northern Great Plains during April – June, the distribution of seasonal rainfall rates (Fig. 3.12a) is, as expected, shifted towards higher values. In addition, the highest spring rainfall total in the control is equaled or surpassed during three years in the future, indicating an increased potential for flooding. Despite the overall wetter conditions, the driest spring projected for the future is more extreme than that of the control simulation, and the 15^{th} percentile, which represents the upper limit on the driest 15% of the springtime rainfall rates, is the same for the future and control. While wetter conditions are projected to be more extreme and occur more frequency in the future, the frequency of droughts remains the same, and the intensity of the strongest drought is amplified.

Over the southern Great Plains, when projections are wetter in March – May, the distribution of springtime rainfall totals (Fig. 3.12b) is shifted to the right, with a median of 2.5 mm/day in the control and 2.9 mm/day in the future. Although the 85^{th} percentile is the same for the future and control, the wettest spring of the 20 years in the future exceeds that of the control. Like the northern Great Plains, the occurrence of drought is similar between the control and future, but over the southern Great Plains, the severity of the most extreme drought does not change.

Future changes in interannual variability of springtime rainfall are different over the Midwest (March – May, Fig. 3.12c) compared to the Great Plains regions. Over the Midwest, there is no change in the median rainfall from the control to the

future. Instead, the wetter conditions are supported by a decreased severity of drought events. For example, the most extreme drought of the control is of 2.9 mm/day in 1988, while the driest spring in the future is 3.4 mm/day. The wetter conditions are also supported by an increase in the frequency and intensity of flood events, with the 85^{th} percentile increasing from 4.9 mm/day in the control to 5.6 mm/day in the future, and the wettest spring increasing from 5.3 mm/day in the control to 6.0 mm/day in the future. The increased intensity of future floods in the spring emerges as a robust signal among the Great Plains and Midwest.

Figure 3.13 displays histograms of the rainfall rates for each summer of the 20 years of the control and future simulations for the averaging regions. Here, the three months selected for the averaging are chosen based on the time period when the monthly precipitation projections are negative. Over the northern Great Plains (Fig. 3.13a) future drying during July – August is received through more frequent and extreme dry years and less extreme wet years. A rainfall rate of 2.9 mm/day, which represents the flood of 1993, is the wettest summer over the northern Great Plains during the control. Although the most extreme summer wet event is less intense in the future, rainfall rates of 2.6 m/day are received during two years, suggesting that floods of slightly weakened intensity may occur more frequently in the future despite the average climatological drying.

The changes in the summer rainfall distributions are much different over the southern Great Plains (Fig. 3.13b). During June – August, the future drying is supported by less extreme, but more frequent dry summers and less extreme and less frequent wet summers. Specifically, while the minimum summer rainfall rate increases from 1.0 mm/day in the control to 1.2 mm/day in the future, rainfall rates of the driest two summers of the control are projected for five summers in the future. The wettest summer of the future receives an average of 1.0 mm/day less than the

wettest summer in the control.

Over the Midwest, drying in June – August occurs as more frequent and more extreme dry summers and less frequent and less extreme wet summers (Fig. 3.13c). The intensity of the strongest flood event is reduced considerably, from 5.8 mm/day to 4.7 mm/day. More severe and/or frequent droughts during the summer months in the future are a common signal over the Great Plains and Midwest.

3.5b Regional climate predictions – near-surface air temperature

Figure 3.14 illustrates the climatological anomalies in monthly near-surface air temperature for the averaging regions. Projections are very similar for the northern and southern Great Plains and Midwest, with a minimum in warming of 0.65 – 0.75 K (1.2 – 1.4°F) in March and a maximum warming of 2.45 – 2.85 K (4.4 – 5.1°F) in August. The greater warming over the Midwest compared to the Great Plains regions may be related to the greater absolute summer rainfall deficit there. The one-sided t-test for differences of the mean is used to assess the significance of the monthly near-surface air temperature predictions. The projected warming in near-surface air temperature is significant at the 10% level in March over the northern and southern Great Plains and in August over the northern and southern Great Plains and the Midwest. The projected annual warming for all three regions is 1.7 – 1.8K (3.0 – 3.2°F).

The projected anomalies for the seasonal near-surface air temperature cycle over the western and eastern South regions are different from the northern regions, but similar to each other. There is a minimum in warming of about 0.9K (1.6°F) in February and a maximum warming of 2.25 – 2.3K (4.0 – 4.1°F) in September over both southern regions. The warming in February and September is significant at the 10% level for the western and eastern South. The projected annual warming in the

South is 1.5K (2.8°F).

Histograms of the frequency of daily maximum near-surface air temperatures occurring during June – September of 1981 – 2000 for the control and 2041 – 2060 for the future are shown in Figures 3.15a – d for the northern Great Plains, southern Great Plains, Midwest, and the western and eastern South regions together. Over the northern Great Plains (Fig. 3.15a), the median daily maximum near-surface air temperature warms about 2K from the control to the future, and the warmest temperatures experienced in the control are projected to occur more frequently in the future. In addition, the 20-year record high daily maximum near-surface air temperature of the control is equaled or exceeded on 28 days in the future. Although the temperature distribution is shifted towards warmer values in the future, the 20-year record low of the control is also projected for the future, indicating that along with the climatological warming in temperatures, there is greater variability projected in the future. The projected changes in near-surface air temperature distributions over the southern Great Plains (Fig. 3.15b) and Midwest (Fig. 3.15c) regions are very similar to those of the northern Great Plains, suggesting that this is a robust signal that is not an artifact of sample size.

The projected near-surface air temperatures over the western and eastern South regions (Fig. 3.15d), which are considered together since they share a similar signal, exhibit a different behavior than the northern regions. While the temperature distribution is shifted towards warmer values, as is the case with the other regions, the variability in temperatures is not projected to increase.

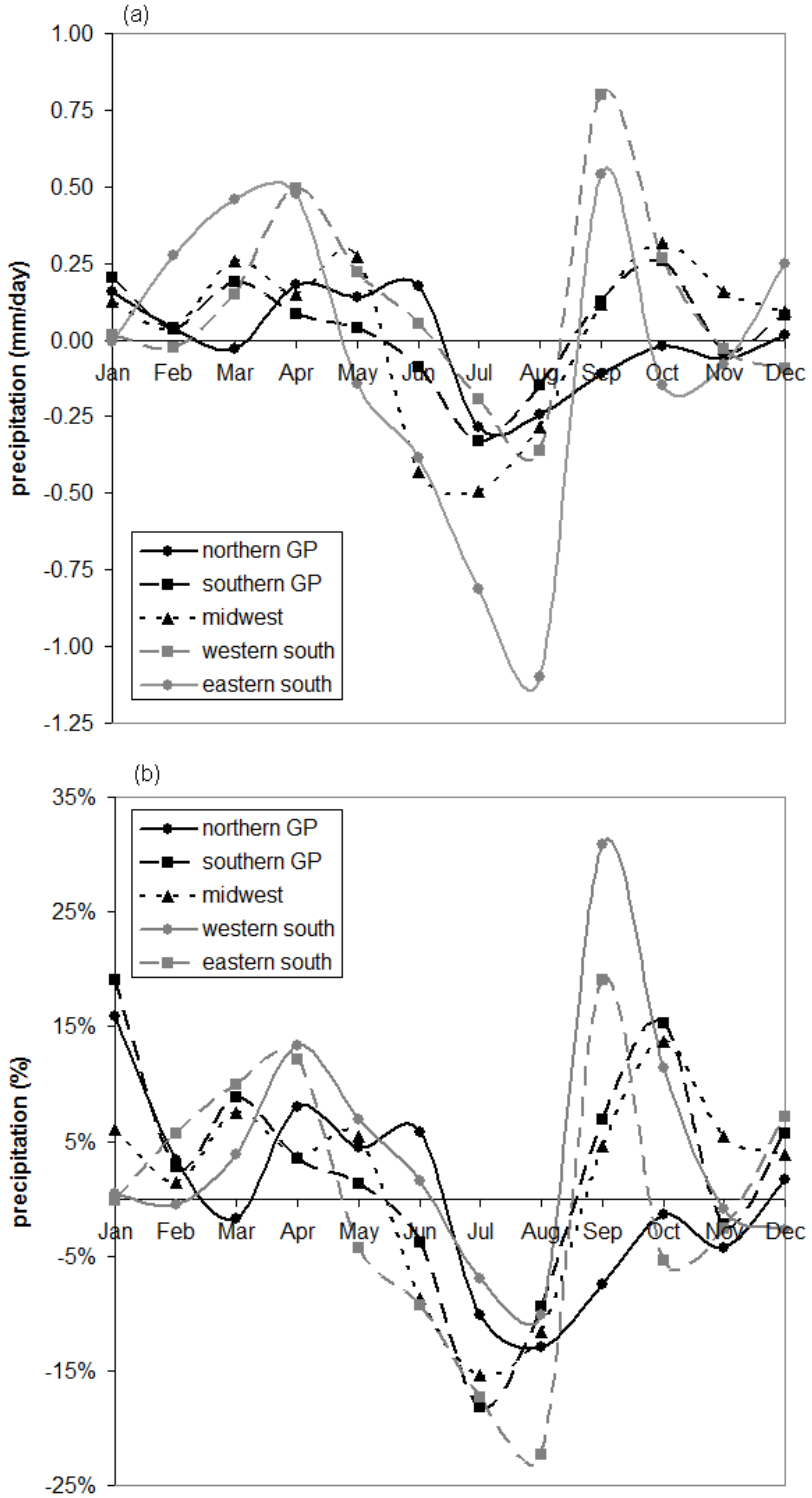

Figure 3.11: Precipitation anomalies (2041 – 2060 minus 1981 – 2000) from the 30 km domain of the RCM expressed as (a) mm/day and (b) percent for the northern Great Plains (black solid), southern Great Plains (black dash), Midwest (black dot), western South (grey solid) and eastern South (grey dash) regions.

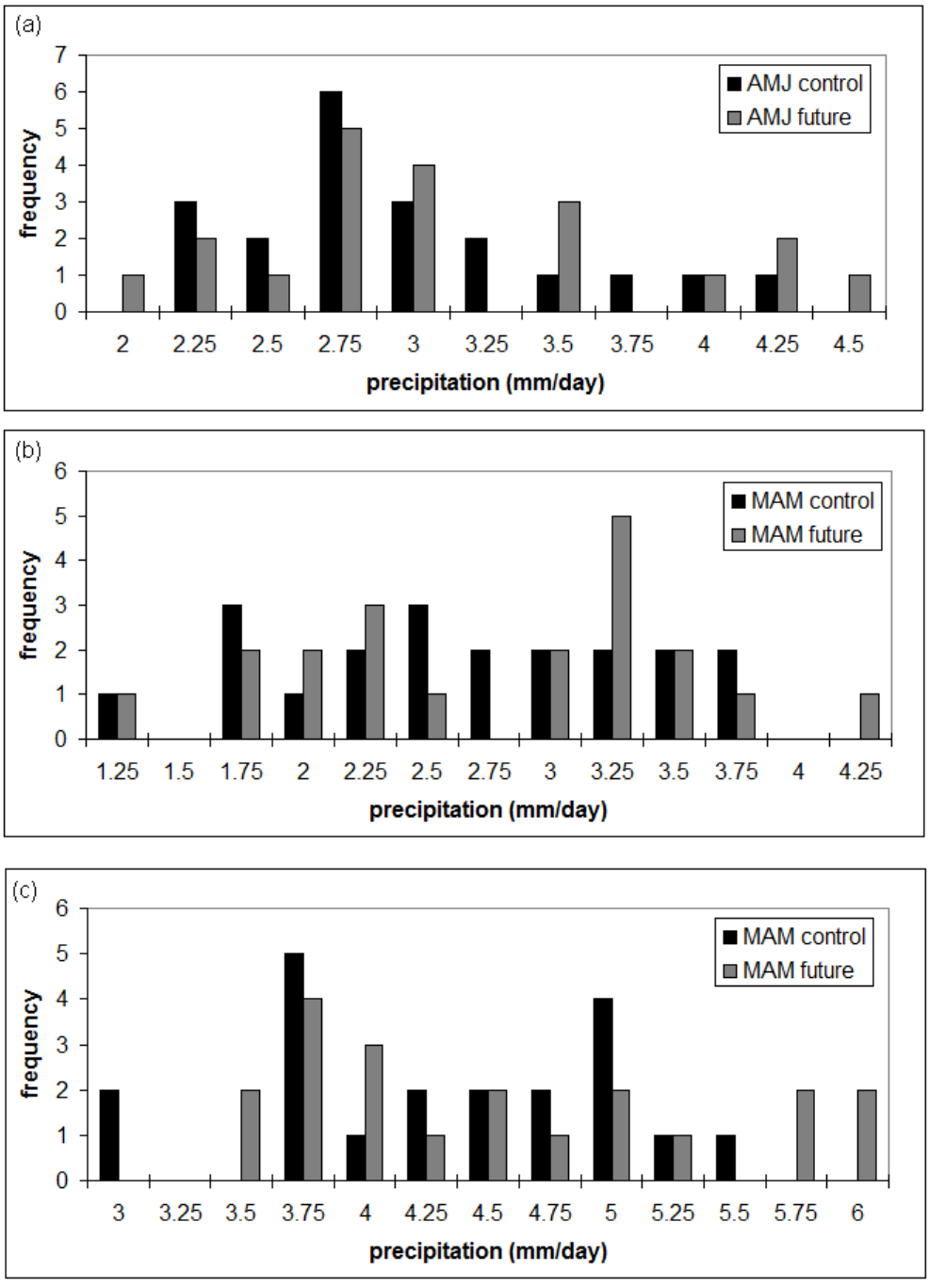

Figure 3.12: Frequency of precipitation rates for the control (black) and future (grey) simulations over the 30 km domain averaged (a) April – June over the northern Great Plains, (b) March – May over the southern Great Plains, and (c) March – May over the Midwest.

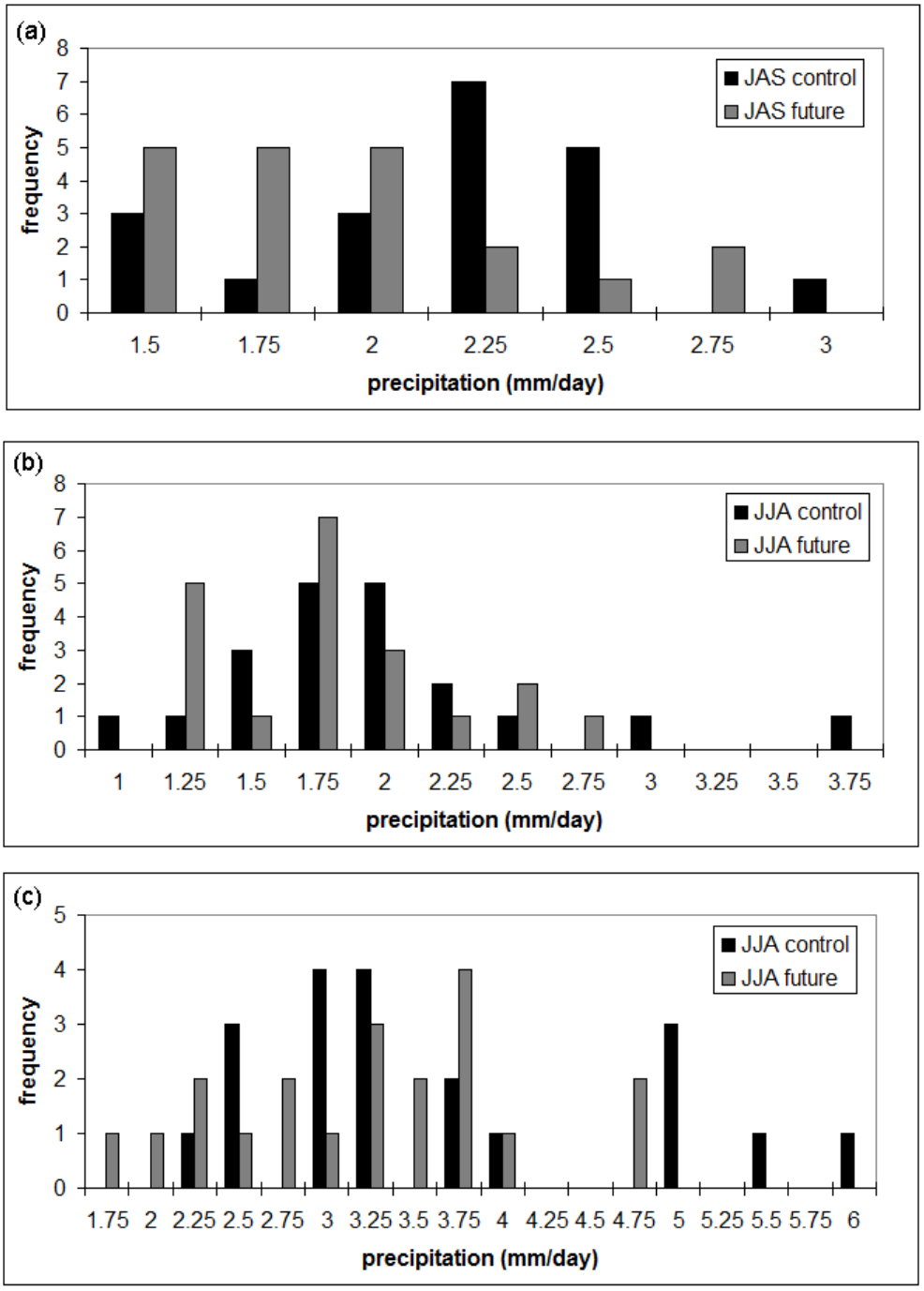

Figure 3.13: Frequency of precipitation rates for the control (black) and future (grey) simulations over the 30 km domain averaged (a) July – September over the northern Great Plains, (b) June – August over the southern Great Plains, and (c) June – August over the Midwest.

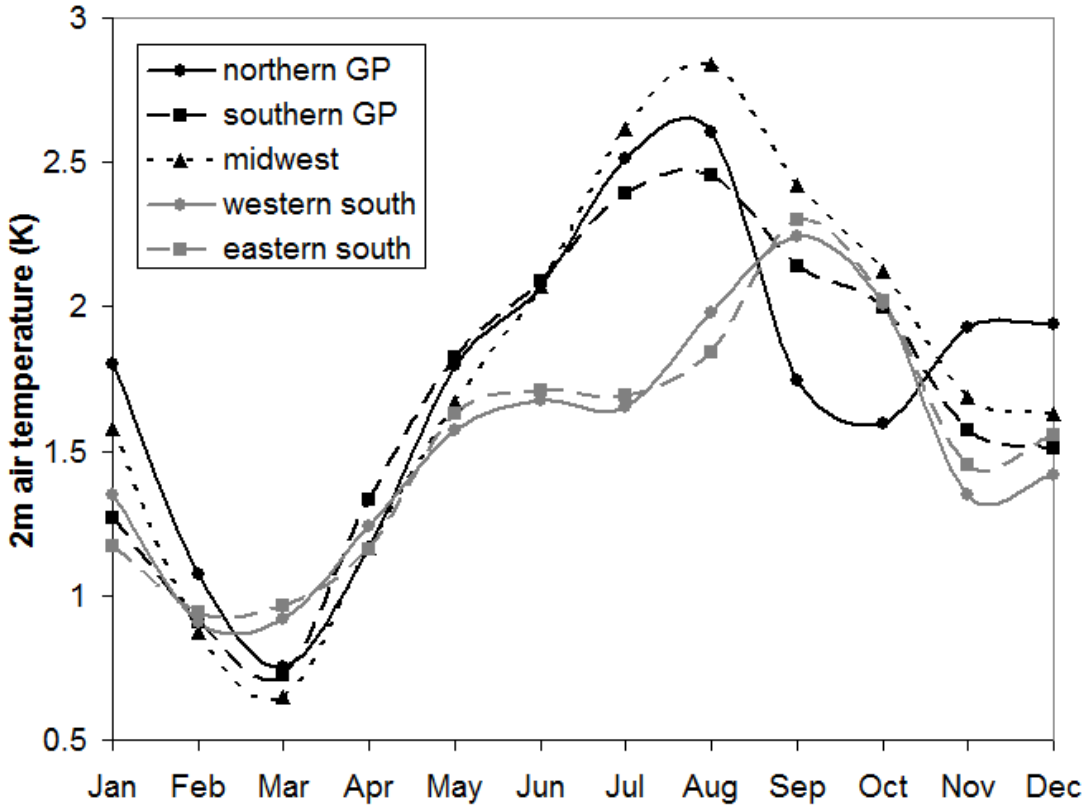

Figure 3.14: Near-surface air temperature (K) anomalies (2041 – 2060 minus 1981 – 2000) from the 30 km domain of the RCM for the northern Great Plains (black solid), southern Great Plains (black dash), Midwest (black dot), western South (grey solid) and eastern South (grey dash) regions.

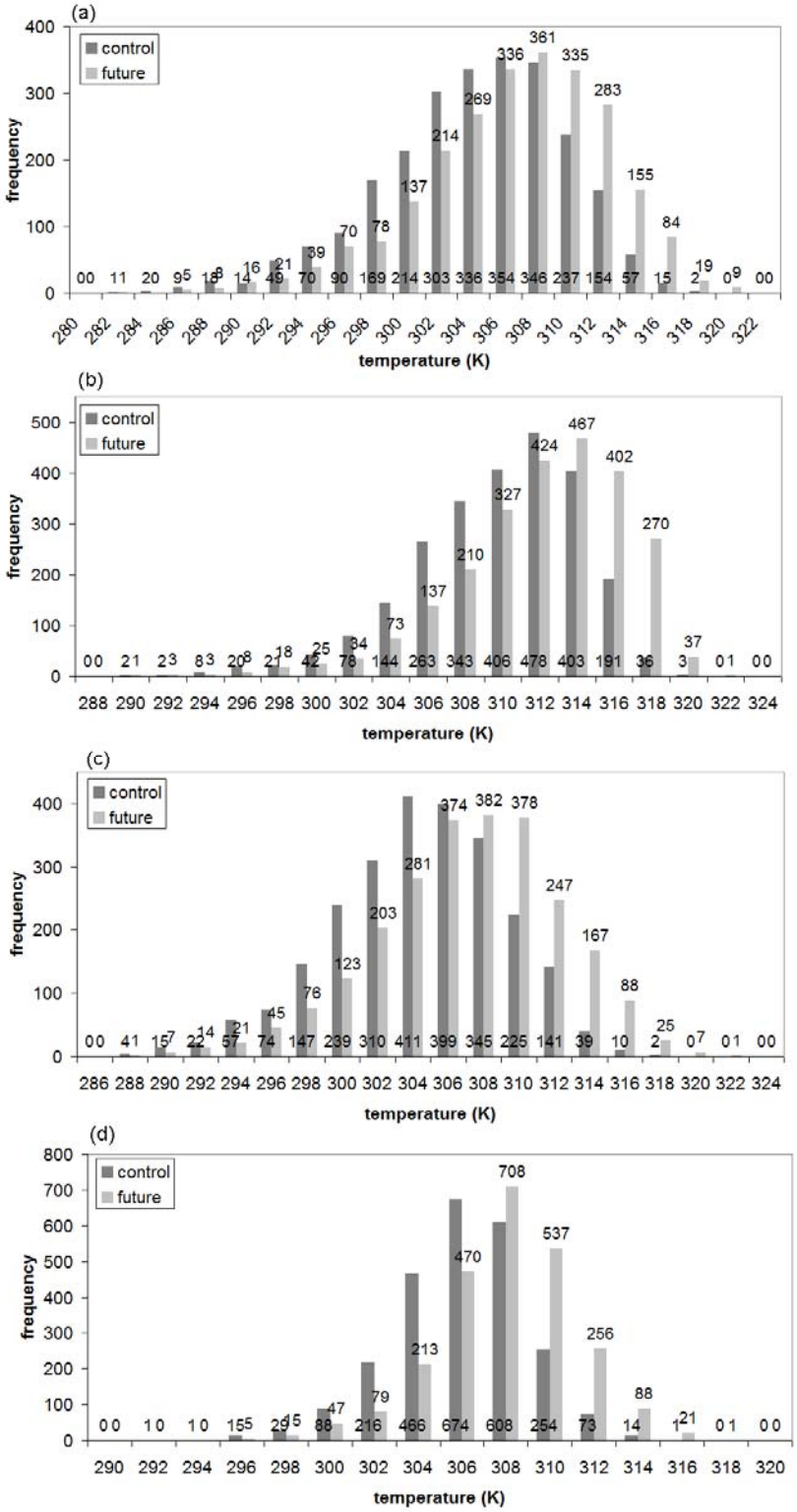

Figure 3.15: Histograms of the frequency of daily maximum near-surface air temperatures occurring between 01 June and 30 September for the control (dark grey) and future (light grey) simulations over the 30 km domain over the (a) northern Great Plains, (b) southern Great Plains, (c) Midwest, and (d) western and eastern South.

3.5c Climate change processes

In order to better understand the relationships between the precipitation projections and circulation anomalies, we utilize the moisture budget. In addition, considering the diurnal cycle of the rainfall projections allows us to further understand the physical processes responsible for the precipitation changes. Figures 3.16a-g show the future anomalies in precipitation, total (the sum of time-mean and transient) moisture convergence, time-mean moisture convergence, moisture convergence due to transient eddies, evaporation, time-mean moisture advection, and moisture advection due to transient eddies, respectively, averaged for April. The residual is not shown since it is relatively small except over the border of Texas and Mexico. In the South during April, the precipitation anomalies (Fig. 3.16a) are primarily supported by anomalies in the total moisture convergence (Fig. 3.16b) with similar contributions from the time-mean (Fig. 3.16b) and transient (Fig. 3.16c) moisture convergence anomalies. Over the northern Great Plains positive rainfall projections are related to anomalous transient moisture convergence, and occur most strongly at 1800 LT and are near-zero at 0300 LT, indicating that they are supported by enhanced local daytime convection as opposed to the nocturnal rainfall processes described in Section 3.2. Evaporation anomalies (Fig. 3.16e) provide a negligible contribution over the entire central U.S. in April. Time-mean moisture advection (Fig. 3.16f) is strongly increased over most of the central U.S. in the future, but is approximately opposed by anomalies in advection due to transient eddies (Fig. 3.16g).

The positive time-mean moisture advection anomalies in April (Fig. 3.16f) are explained by the low-level wind anomalies and the gradient in atmospheric moisture anomalies. Figure 3.16h shows anomalies in the vertically-integrated water vapor mixing ratio and the horizontal winds at 925 hPa averaged over April. The meridional gradient in atmospheric moisture anomalies, with more positive anomalies over the

Gulf of Mexico, and the anomalous anticyclonic circulation support positive time-mean moisture advection anomalies in April.

The anomalous anticyclonic circulation over the eastern U.S. that supports the positive moisture advection anomalies is related to large-scale changes in the North Atlantic subtropical high. Figure 3.17 shows monthly anomalies in geopotential height and wind at 925 hPa from the 90 km domain for April through September. In April the NASH is stronger and extended towards the west and east (Fig. 3.17a). The westward expansion of the NASH over the eastern U.S. places southerly low-level wind anomalies over the central U.S., which supply moisture to the Great Plains and Midwest regions from the Gulf of Mexico.

The precipitation anomalies in May (not shown) are supported in a similar way as in April. Wetter conditions over the northern Great Plains are supported by anomalous time-mean and transient moisture convergence, with evaporation playing a negligible role and anomalies in time-mean and transient moisture advection approximately balancing. As in April, the positive rainfall anomalies peak in the late evening over the northern Great Plains suggesting the importance of similar physical processes.

While the climate response is comparable between April and May, the rainfall projections in June are supported by different physical processes. Figure 3.18 is the same as Figure 3.16, but for June. Similar to April and May, during June future anomalies in evaporation (Fig. 3.18e) play a small role in supporting the rainfall projections (Fig. 3.18a), and the anomalies in time-mean moisture advection (Fig. 3.18f) are approximately balanced by the anomalies in moisture advection due to transient eddies (Fig. 3.18g). The positive precipitation anomalies over the northern Great Plains in June are supported primarily by anomalous time-mean moisture convergence (Fig. 3.18c), which is dominated by meridional convergence anomalies

and opposed by zonal divergence anomalies (not shown), and is very weakly opposed by moisture convergence due to transients (Fig. 3.18d). Over the Midwest, the negative precipitation projections are supported by both anomalous time-mean moisture divergence (Fig. 3.18c), which is dominated by the zonal component and opposed by the meridional component (not shown), as well as anomalous transient moisture divergence (Fig. 3.18d), which is primarily meridional (not shown).

A better understanding of the connection between the precipitation and circulation anomalies is enabled by considering the diurnal timescale. The 3-hourly precipitation anomalies during June over the northern Great Plains and the Midwest are shown in Figure 3.19. The anomalies in the diurnal cycle are strong over the northern Great Plains, with maximum increases occurring from 0000 – 0600 LT, and a minimum of no change at 1200 LT, suggesting that changes in the GPLLJ, and not daytime convection, are supporting the rainfall anomalies. Over the Midwest, negative anomalies peak at 0000 LT and 1500 LT, suggesting both a connection with the GPLLJ as well as a contribution from suppressed daytime convection.

By investigating the connection between the anomalous moisture convergence and low-level wind convergence, the role of the GPLLJ in supporting the rainfall anomalies in June becomes clear. The pattern of vertically-integrated low-level (surface – 775 hPa) atmospheric convergence anomalies averaged over June (not shown) resembles that of the anomalous vertically-integrated time-mean moisture convergence field (Fig 16c), indicating that the spatial pattern of those moisture convergence anomalies is dominated by changes in the wind field, and not by changes in atmospheric moisture. In addition, the 3-hourly low-level atmospheric convergence anomalies show a significant diurnal cycle that is consistent with the anomalies in the diurnal precipitation, with the strongest convergence occurring between 0000 – 0600 LT over the northern Great Plains, further supporting a connection between the rainfall

anomalies and the GPLLJ.

Figure 3.20a plots the anomalies in the meridional wind (shaded) and horizontal wind (vectors) at 925 hPa for June averaged 0000 – 0600 LT. In the future the meridional wind at 0000 – 0600 LT is more southerly over nearly the entire central U.S., and the nocturnal GPLLJ is strengthened especially north of the core in the jet exit region. Since the convergence of the geostrophic wind is zero, we remove the geostrophic wind component to more clearly identify the anomalies in the full wind field that contribute to the anomalous convergence. Figures 3.20b and c show the ageostrophic meridional and horizontal wind at 925 hPa for June averaged 0000 – 0600 LT from the control simulation and the future anomalies, respectively. Like the full wind (Figs. 3.8 and 3.9), the ageostrophic wind demonstrates a significant diurnal cycle (not shown). In June of the control simulation, the ageostrophic component of the GPLLJ peaks between 0000 – 0600 LT, and the southerly flow reaches the border of Canada and the U.S. (Fig. 3.20b). The ageostrophic component of the meridional wind is positive, but weaker, and does not penetrate as far north in the hours before and after the peak of the GPLLJ, and at 1200 – 1500 LT the meridional ageostrophic wind is northerly (not shown).

The ageostrophic wind anomalies at 0000 – 0600 LT in June (Fig. 3.20c) are similar in pattern and weaker in magnitude than the full wind anomalies (Fig. 3.20a), with stronger southerly ageostrophic wind anomalies reaching as far north as Iowa. North of about 44°N, the ageostrophic wind anomalies are weak or negative, and so the northern extent of the ageostrophic component of the GPLLJ does not penetrate as far north in the future. These anomalies in the meridional ageostrophic wind at 0000 – 0600 LT support the anomalous low-level convergence that contributes to the time-mean moisture convergence anomalies (Fig. 3.18c) that sustain enhanced precipitation in the northern Great Plains in the future (Fig. 3.18a). The full and ageostrophic wind

anomalies at 0000 – 0600 LT in June are more zonally oriented over the Midwest region (Figs. 3.20a and c) and contribute to the time-mean moisture divergence anomalies (Fig. 3.18c) that support precipitation decreases over that region in the future.

While the precipitation projections in June are primarily supported by time-mean and transient moisture convergence anomalies, the contributions of advection and evaporation are also important over some regions in July. Figure 3.21, which is the same as Figures 3.16 and 3.18, but for July, shows the future anomalies in various terms of the moisture budget as well as the water vapor mixing ratio and low-level wind anomalies. Although precipitation projections are negative over the northern and southern Great Plains and Midwest regions (Fig. 3.21a), the physical processes supporting the anomalies are not uniform among the regions. Over North Dakota, South Dakota, and Minnesota in the northern Great Plains and eastern Iowa, Illinois, and Indiana in the Midwest regions the precipitation anomalies are primarily supported by anomalous moisture divergence due to transient eddies (Fig. 3.21d), with secondary support from time-mean moisture divergence anomalies (Fig 3.21c). The rainfall deficit is strongest at 1500 LT over the northern Great Plains, suggesting the importance of reduced local convection, with a secondary minimum at 0300 – 0600 LT. Over the Midwest negative rainfall anomalies occur most strongly at 0000 LT.

Over northern Kansas and Missouri, eastern Nebraska, and northern Iowa precipitation projections (Fig. 3.21a) are weakly negative despite large time-mean moisture convergence anomalies (Fig 3.21c). The negative contribution of time-mean moisture advection (Fig. 3.21f) is important over these regions and is related to the change in the orientation of the atmospheric moisture anomalies (Fig. 3.21h), from meridional in April to zonal in July, and to the position of the anomalies in the North Atlantic subtropical high. In July, the NASH is strengthened in the west, with the

greatest height anomalies located over the east coast of the U.S. and tilted from the southwest to northeast (Fig 3.17d), which leads to southwesterly winds over Oklahoma and Kansas (Fig. 3.21h) that advect relatively drier air into that region.

In the southern Great Plains over Oklahoma and Arkansas, the large negative contribution of the time-mean moisture divergence anomalies (Fig. 3.21c) is lessened by positive time-mean (Fig. 3.21f) and transient (Fig. 3.21g) moisture advection anomalies. Similar to the northern Great Plains, the negative rainfall anomalies are most intense at 1800 LT with a secondary minimum at 0900 LT.

Figure 3.22 shows the anomalies in precipitation, evaporation, the sum of the time-mean and transient moisture convergence and advection and the residual, and the time-mean moisture convergence for August. Over the eastern South region, where PME is positive in the control during August, anomalous time-mean moisture convergence (Fig. 3.22d) is the primary contributor to the strongly negative precipitation anomalies (Fig. 3.22a). The future response over the northern Great Plains regions is very different compared to the eastern South region. Over the northern Great Plains, the negative precipitation anomalies are primarily supported by decreased evaporation (Fig. 3.22b) with little contribution from the other terms of the moisture budget (Fig. 3.22c). This suggests that, similar to the present day mechanism for prolonging and intensifying droughts (e.g., Hong and Kalnay 2000; Schubert et al. 2004; Wu and Kinter 2009), the soil moisture has provided a memory of the negative precipitation anomalies from the previous month over that region. Since PME is negative in July and August, the rainfall deficit in July future desiccates the ground resulting in an further decreased supply of soil moisture in August. This mechanism prolongs the negative precipitation anomalies through September, and in October anomalous time-mean and transient moisture convergence dominates the moisture budget over the Great Plains (not shown).

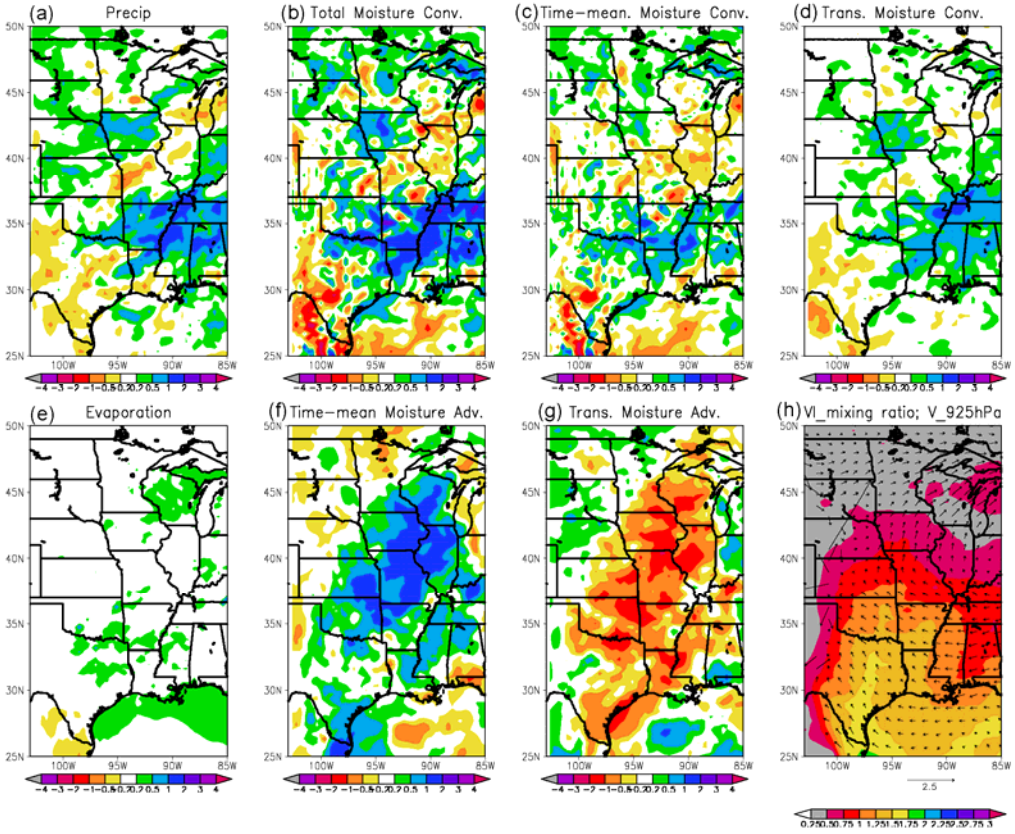

Figure 3.16: Anomalies (2041 – 2060 minus 1981 – 2000) in (a) precipitation, (b) total vertically-integrated moisture convergence [the sum of (c) and (d)], (c) vertically-integrated time-mean moisture convergence, (d) vertically-integrated moisture convergence due to transient eddies, (e) evaporation, (f) vertically-integrated time-mean moisture advection, and (g) vertically-integrated moisture advection due to transient eddies for April from the 30 km domain. Units are mm/day. (h) Anomalies in vertically-integrated water vapor mixing ratio (shaded; kg water vapor/kg air) and wind at 925 hPa (vector; m/s) for April from the 30 km domain.

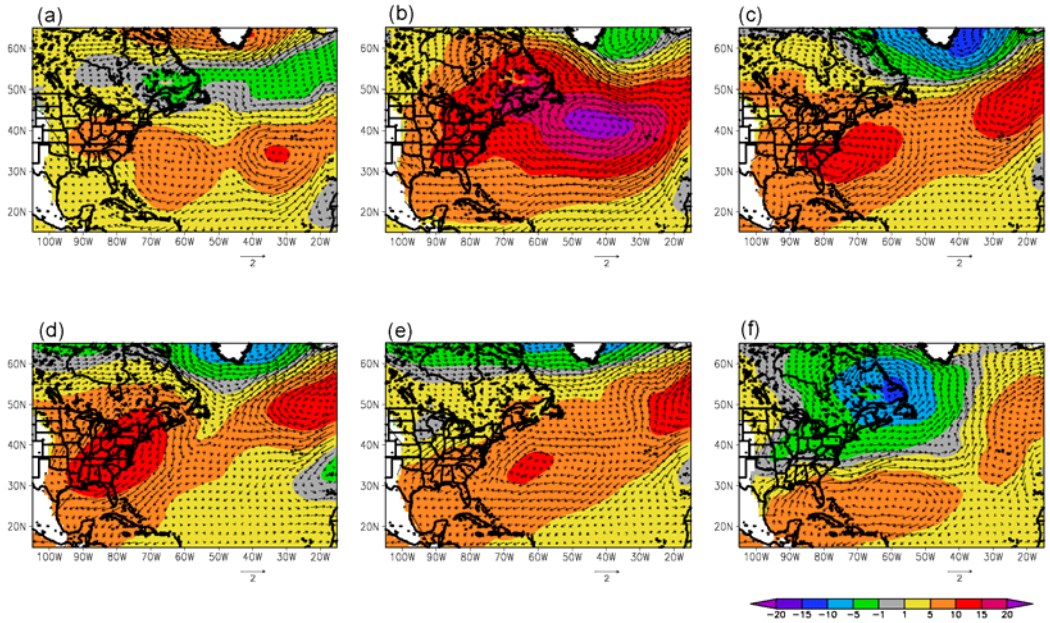

Figure 3.17: Anomalies in geopotential heights (shaded; m) and horizontal wind (vector; m/s) at 925 hPa for (a) April, (b) May, (c) June, (d) July, (e) August, and (f) September from the 90 km domain.

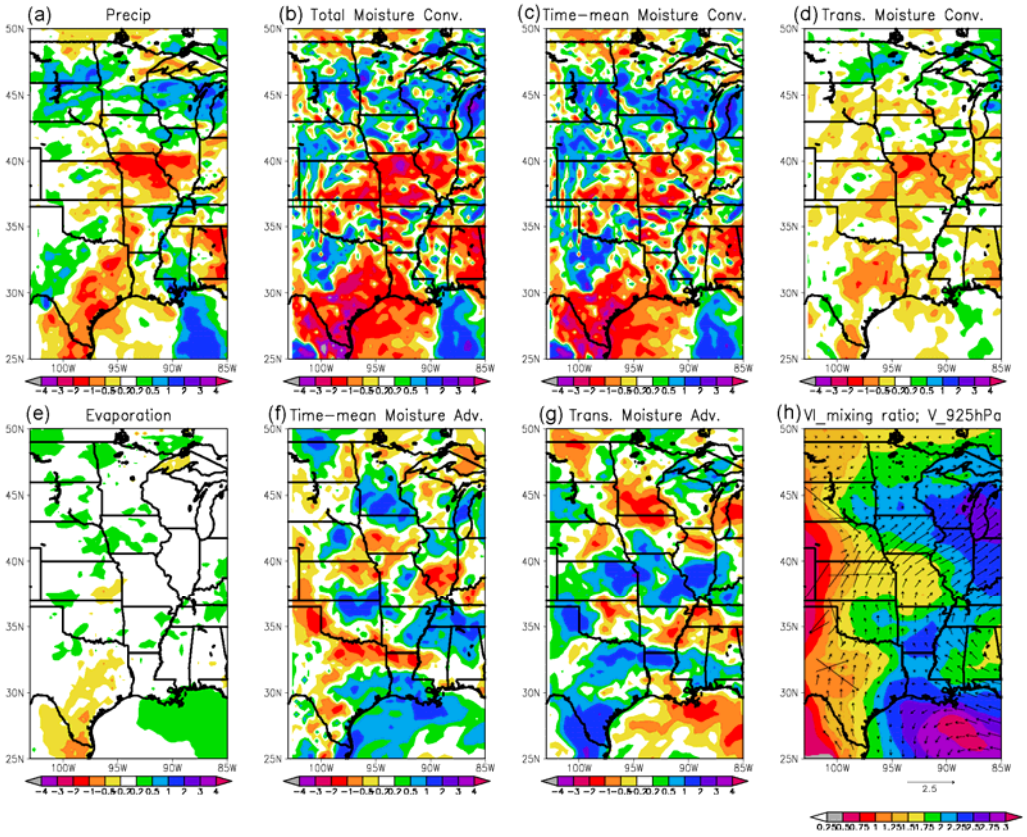

Figure 3.18: The same as Figure 3.16, but for June.

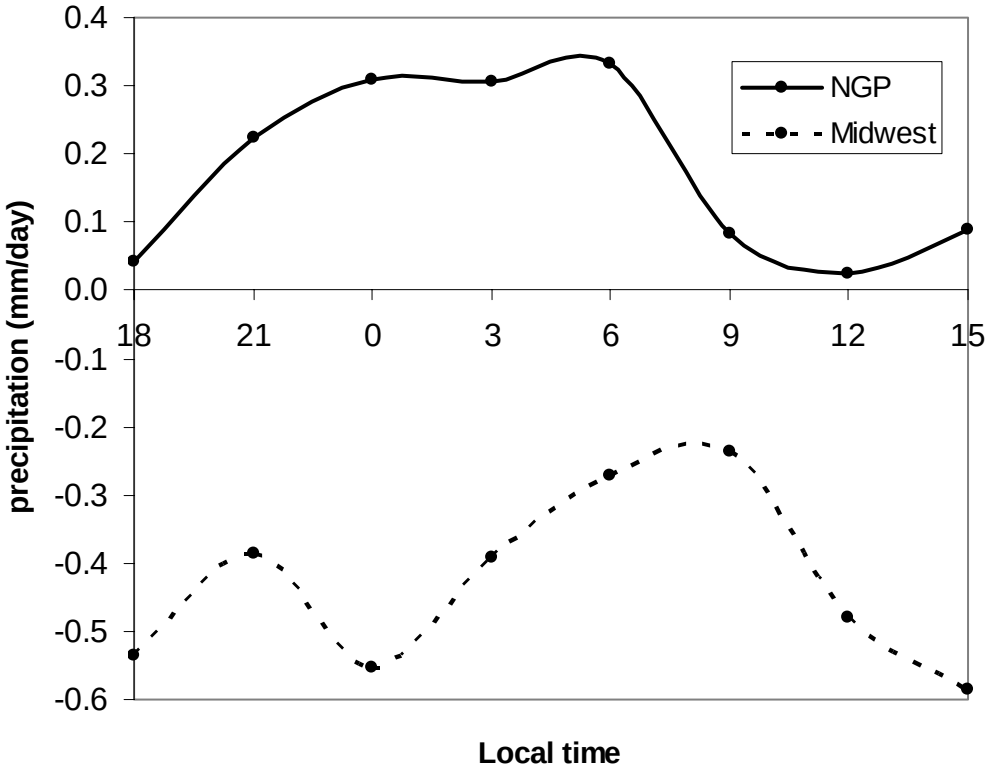

Figure 3.19: Future anomalies (2041 – 2060 minus 1981 – 2000) in precipitation (mm/day) averaged over June on the 3-hourly timescale for the northern Great Plains (solid) and Midwest (dashed).

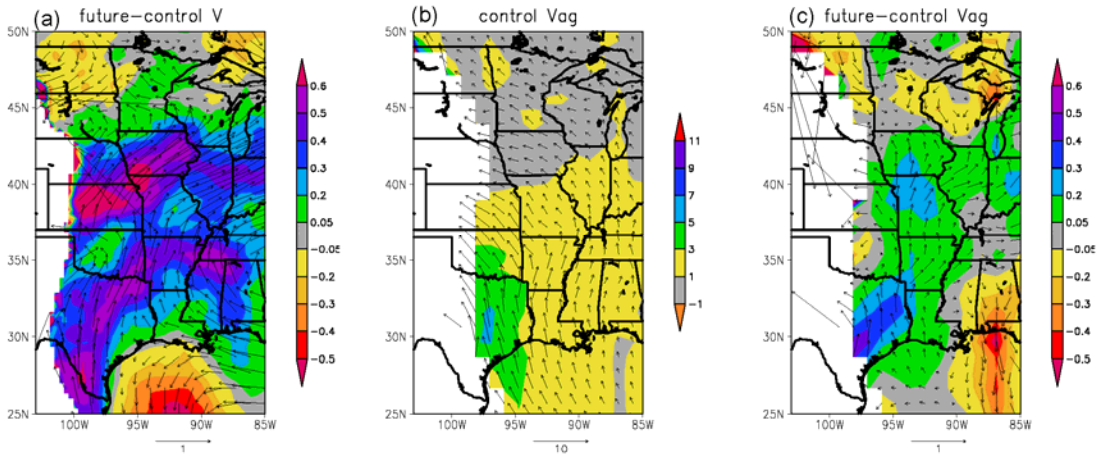

Figure 3.20: The (a) future anomalies in the meridional wind (shaded) and horizontal wind (vector), (b) meridional ageostrophic wind (shaded) and horizontal ageostrophic wind (vector) from the control simulation, and (c) future anomalies in the meridional ageostrophic wind (shaded) and horizontal ageostrophic wind (vector) at 925 hPa averaged 0000 – 0600 LT during June. Units are m/s and topography is shaded white. The scales are the same for Figure 3.20b and Figure 3.9 and for Figure 3.20a and c.

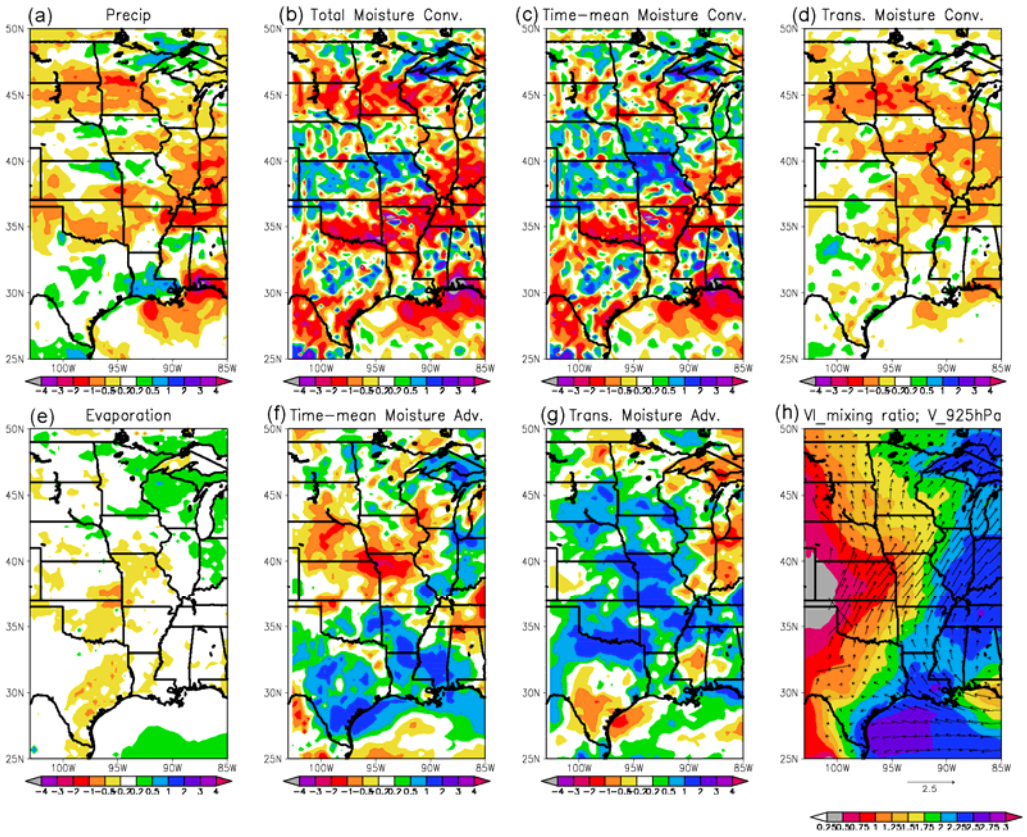

Figure 3.21: The same as Figure 3.16, but for July.

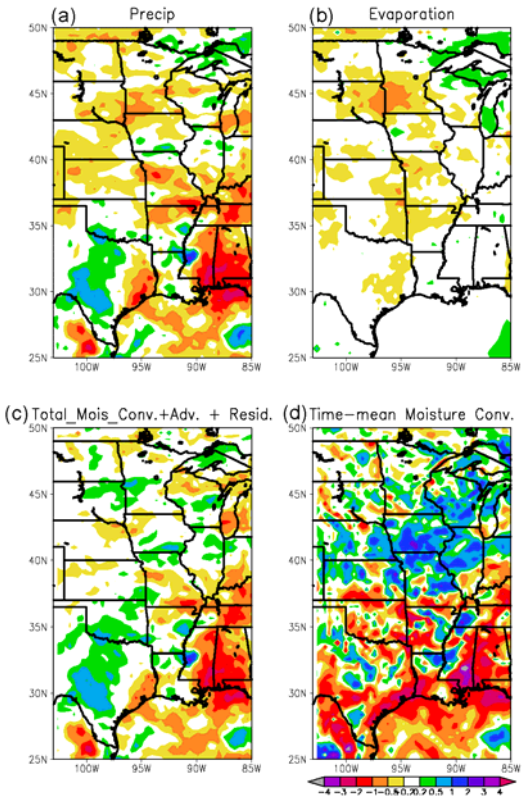

Figure 3.22. Anomalies (2041 – 2060 minus 1981 – 2000) in (a) precipitation, (b) evaporation, (c) the sum of the vertically-integrated time-mean and transient moisture convergence and advection and the residual, and (d) vertically-integrated time-mean moisture convergence for August from the 30 km domain. Units are mm/day.

3.6 Conclusions

A regional climate model is used to generate climate projections for the mid-twenty-first century over the central U.S. and understand the processes of climate change in that region. The regional simulation design differs from the typically employed dynamic downscaling method, which uses lateral and surface boundary conditions prescribed directly from AOGCMs for both the control and future integrations. Here, lateral and surface boundary conditions for the control are obtained from reanalysis products, and boundary conditions for the future are created by adding anomalies from AOGCMs to the reanalysis. This method accounts for changes in the mean state of the boundary conditions, but the transients prescribed on the lateral boundaries remain the same between the control and future simulations.

Precipitation projections are very similar among the northern and southern Great Plains and the Midwest, with wetter conditions in the spring (MAM in the southern Great Plains and Midwest and AMJ in the northern Great Plains) and drying in the summer (JJA in the southern Great Plains and Midwest and JAS in the northern Great Plains). While precipitation changes are sizeable on the monthly timescale, reaching up to +/- 15%, annual precipitation changes are very weak.

Along with climatological changes in the future spring and summer rainfall, changes in interannual variability are projected as well. The range of interannual variability is increased over the northern Great Plains in the spring when conditions are projected to be wetter, with more severe drought and flood events projected in the future. However, considering the moderate sample size, this result should be compared with other studies. Over the Great Plains and Midwest, more severe flooding is predicted in the spring, with more severe and/or frequent drought in the summer.

Precipitation anomalies over the western and eastern South regions are

somewhat similar, although less coherent compared with the northern regions. The western (eastern) South is projected to experience drying from March through June (March and April) and wetter conditions during July and August (May through August). The magnitude of the rainfall anomalies is greater in the southern regions compared with the rest of the central U.S. and is strongly influenced by a few individual years.

Annually averaged near-surface air temperatures are projected to warm from 2.8-3.2°F over the central U.S. There is a pronounced seasonal cycle with maximum warming over the northern and southern Great Plains and the Midwest of 4.4-5.1°F in August and a minimum in warming of 1.2-1.4°F in March. The seasonal cycle is different over the South where there is a maximum projected warming of 4.0-4.1°F in September and minimum warming of 1.6°F in February.

The distributions of the JJAS daily maximum near-surface air temperature are shifted towards warmer values with the 20-year record high of the present day often being exceeded in the future over all of the central U.S. Unlike the South, variability over the northern and southern Great Plains and the Midwest is expected to increase in the future, with a 20-year record low daily maximum air temperature that is similar for the present day and future.

An analysis of future anomalies in moisture budget, circulation, and diurnal precipitation cycle reveals that the projected precipitation anomalies are related to different physical processes throughout the spring and summer. In April and May positive rainfall projections occur most strongly in the afternoon and evening hours and are supported primarily by anomalous moisture convergence due to transient eddies, suggesting the importance of enhanced local daytime convection. During June, increased rainfall over the northern Great Plains is strongest from 0000 - 0600 LT and is supported by anomalous time-mean meridional moisture convergence

related to a strengthening of the GPLLJ, especially in the jet exit region. Over the Midwest, decreased rainfall is strongest at 1500 LT and 0000 LT and is supported by anomalous moisture divergence due to transient eddies and anomalous time-mean zonal divergence, indicating the importance of both suppressed local daytime convection as well as changes in the zonal flow in the GPLLJ exit region. Negative precipitation anomalies over the northern Great Plains begin in July and are related to weakened local daytime convection, as suggested by the significant contribution from anomalous moisture divergence due to transient eddies and the occurrence of the maximum anomaly in the afternoon. Drying over the northern Great Plains persists throughout August and September when the deficit in soil moisture and strong land-atmosphere feedbacks dominate.

This study provides high-resolution climate predictions for the central U.S. during the mid-twenty-first century to better understand the impacts of climate change on the regional scale. A useful addition to this study would be an assessment of the impacts of the predicted changes in seasonal precipitation and temperature on agriculture. A comparison of the predictions from this study with those from the North American Regional Climate Change Assessment Program (NARCCAP), which is currently completing a suite of direct downscaling simulations with several regional climate models, is planned for future work.

REFERENCES

Bonner WD (1968) Climatology of the low level jet. Mon Wea Rev 96: 833-850.

Carbone RE, Tuttle JD (2008) Rainfall occurrence in the U.S. warm season: The diurnal cycle. J Clim 21: 4132-4146.

Chang F-C, Smith EA (2001) Hydrological and dynamical characteristics of summertime droughts over the U.S. Great Plains. J Clim 14: 2296-2316.

Chen H, Zhou T, Yu R, Li J (2009) Short Communication: Summer rain fall duration and its diurnal cycle over the US Great Plains. IntJ Climatol 29: 1515-1519.

Cook BI, Miller RL, Seager R (2008) Dust and sea surface temperature forcing of the 1930s "Dust Bowl" drought. Geophys Res Lett 35: L08710, doi:10.1029/2008GL033486.

Cook KH, Vizy EK, Launer ZS, Patricola CM (2008) Springtime intensification of the Great Plains low-level jet and Midwest precipitation in GCM simulations of the twenty-first century. J Clim 21: 6321-6340.

Dirmeyer PA, Brubaker KL (1999) Contrasting evaporative moisture sources during the drought of 1988 and the flood of 1993. J Geophys Res 104: 19383-19397.

European Centre for Medium-Range Weather Forecasts (2002) The ERA-40 Archive. Reading, ECMWF: 40.

Han J, Roads JO (2004) U.S. climate sensitivity simulated with the NCEP Regional Spectral Model. Clim Change 62: 115-154.

Hoerling M, Quan X-W, Eischeid J (2009) Distinct causes for two principal U.S droughts of the 20th century. Geophys Res Lett 36: L19708, doi:10.1029/2009GL039860.

Hong S-Y, Kalnay E (2000) Role of sea surface temperature and soil-moisture feedback in the 1998 Oklahoma-Texas drought. Nature 408: 842-844.

IPCC (2007) Climate change 2007: Impacts, adaptation and vulnerability. In: Parry ML, Canziani OF, Palutikof JP, van der Linden PJ, Hanson CE (eds) Contribution of Working Group II to the Fourth Assessment Report of the Intergovernmental Panel on Climate Change. Cambridge University Press, Cambridge, p 976

IPCC (2000) Emissions Scenarios, Nakicenovic N, Swart R Eds., Cambridge University Press, Cambridge, UK: 570pp.

Kalnay E et al (1996) The NCEP/NCAR 40-Year Reanalysis Project. Bull Am Meteorol Soc 77:437–471.

Jiang X, Lau N-C, Held IM, Ploshay JJ (2007) Mechanisms of the Great Plains low-level jet as simulated in an AGCM. J Atm Sci 64: 532-547.

Kanamitsu M., Ebisuzaki W, Woollen J, Yang S-K, Hnilo JJ, Fiorino M, Potter GL (2002) NCEP-DOE AMIP-II Reanalysis (R-2). Bul of the Am Met Soc 83: 1631-1643.

Koster RD et al (2004) Regions of strong coupling between soil moisture and precipitation. Science 305(5687): 1138 – 1140.

Lee M-I, Schubert SD, Suarez MJ, Held IM, Lau N-C, Ploshay JJ, Kumar A, Kim H-K, Schemm J-K E (2007) An analysis of the warm-season diurnal cycle over the continental United States and northern Mexico in general circulation models. J Hydrometeor 8: 344-366.

Lee Schubert SD, Suarez MJ, Schemm J-K E, Pan H-L, Han J, Yoo S-H (2008) Role of convection triggers in the simulation of the diurnal cycle of precipitation over the United States Great Plains in a general circulation model. J Geophys Res 113: D02111, doi:10.1029/2007JD008984.

Lenters JD, Cook KH (1995) Simulation and diagnosis of the regional summertime precipitation climatology in South America. J Clim 8: 2988-3005.

Liang X-Z, Li L, Dai A, Kunkel KE (2004) Regional climate model simulation of summer precipitation diurnal cycle over the United States. Geophys Res Lett 31: L24208, doi:10.1029/2004GL021054.

Liang X-Z, Pan J, Zhu J, Kunkel KE, Wang J XL, Dai A (2006) Regional climate model downscaling of the U.S. summer climate and future change. J Geophys Res 111: D10108, doi:10.1029/2005JD006685.

Liang X-Z, Kunkel KE, Meehl GA, Jones RG, Wang J XL (2008) Regional climate models downscaling analysis of general circulation models present climate biases propagation into future projections. Geophys Res Lett 35: L08709, doi:10.1029/2007GL032849.

Mo KC, Paegle JN, Higgins RW (1997) Atmospheric processes associated with summer floods and droughts in the Central United States. J Clim 10: 3028-3046.

Paeth H, Latif M, Hense A (2003) Global SST influence on twentieth century NAO variability. Clim Dyn 21: 63-75.

Patricola CM, Cook KH (2009) Northern African Climate at the end of the 21st Century: Integrated Application of Regional and Global Climate Models. Clim Dyn DOI 10.1007/s00382-009-0623-7.

Schubert SD, Suarez MJ, Pegion PJ, Koster RD, Bacmeister JT (2004) On the cause of the 1930s Dust Bowl. Science 303: 1855-1859.

Schubert SD, Suarex MJ, Pegion PJ, Koster RD, Bacmeister JT (2007) Predictability of long-term drought and pluvial conditions in the U.S. Great Plains. J Clim 21:802-816.

Seager R, Kushnir Y, Ting M, Cane M, Naik N, Miller J (2008) Would advance knowledge of the 1930s SSTs have allowed prediction of the dust bowl drought? J Clim 21: 3261-3280.

Skamarock WC et al (2008) A description of the Advanced Research WRF Version 3. NCAR Tech. Note, NCAR/TN-475+STR, 113 pp.

Ting M, Wang H (2006) The role of the North American topography on the maintenance of the Great Plains summer low-level jet. J Atm Sci 63: 1056-1068.

Trenberth KE, GW Branstator, PA Arkin (1988) Origins of the 1988 North American drought. Science 242: 1640-1645.

Trenberth KE, GW Branstator (1992) Issues in establishing causes of the 1988 drought over North America. J Clim 5: 159-172.

Van den Dool HM, Peng P, Johansson A, Chelliah M, Shabbar A, Saha S (2006) Seasonal-to-decadal predictability and prediction of North American climate – The Atlantic influence. J Clim 19: 6005-3024.

Weaver SJ, Nigam S (2008) Variability of the Great Plains low-level jet: Large-scale circulation context and hydroclimate impacts. J Clim 21: 1532 -1551.

Weaver SJ, Ruiz-Barradas A, Nigam S (2009a) Pentad evolution of the 1988 drought and 1993 flood over the Great Plains: An NARR perspective on the atmospheric and terrestrial water balance. J Clim 22: 5366-5384.

Weaver SJ, Schubert S, Wang H, (2009b) Warm season variations in the low-level circulation and precipitation over the central United States in observations, AMIP simulations, and idealized SST experiments. J Clim 22: 5401:5420.

Wu R, Kinter JL (2009) Analysis of the relationship of U.S. droughts with SST and soil moisture: Distinguishing the time scale of droughts. J Clim 22:4520-4538.

Wu Y, Raman S (1998) The Summertime Great Plains Low Level Jet And The Effect of Its Origin On Moisture Transport. Boundary Layer Met 88: 445-466.

Zhang J, Wang W-C, Leung LR (2008) Contribution of land-atmosphere coupling to summer climate variability over the contiguous United States. J Geophys Res 113: D22109, doi:10.1029/2008JD010136.